UNIVERSITÀ DEGLI STUDI DI PADOVA

DIPARTIMENTO DI SCIENZE CHIMICHE

CORSO DI LAUREA MAGISTRALE IN SCIENZA DEI MATERIALI

TESI DI LAUREA MAGISTRALE

Rational understanding of exsolution process in Ru-doped $LaFeO_3$ perovskite-like for OER

Relatore: Prof.ssa Silvia Gross
Correlatore: Dr. Jaime Gallego

LAUREANDO: Filippo Bragioto

ANNO ACCADEMICO 2022/2023

List of acronyms

BET	Brunauer–Emmett–Teller
CB	Carbon black
CE	Counter electrode
CRMs	Critical raw materials
CV	Cyclic voltammetry
DFT	Density functional theory
ECSA	Electrochemical active surface area
EIS	Electrochemical impedance spectroscopy
HER	Hydrogen evolution reaction
HR	High resolution
L0.9FR	$La_{0.9}Fe_{0.9}Ru_{0.1}O_3$
LFR	$LaFe_{0.9}Ru_{0.1}O_3$
LSV	Linear sweep voltammetry
NPs	Nanoparticles
OER	Oxygen evolution reaction
PCC	Products of complete combustion
PGMs	Platinum group metals
PIC	Products of incomplete combustion
RE	Reference electrode
SEM	Scanning electron microscopy
TEM	Transmission electron microscopy
TGA/MS	Thermogravimetric analysis/mass spectrometry
WE	Working electrode
XPS	X-ray photoelectron spectroscopy
XRD	X-ray diffraction

Table of contents

Chapter 1

Motivation and aim of the thesis

The energy crisis is a significant challenge for the world today. The primary global energy source nowadays is fossil fuels (including oil, coal, and natural gas) which represent 82% of the energy consumption.[1] This value in recent years slightly decreased in favor of all renewable energy resources. Still, at the present rate of decline, nearly 200 years would be needed to reach zero consumption of fossil fuels; furthermore, the energy global demand increases with an annual growth rate of 1.4% in the last decade.[1] The combustion of fossil fuels is the primary source of air pollution and greenhouse gases emissions driving climate change. The combustion products are fine respirable particles, carbon monoxide, sulfur dioxide, nitrogen oxides, polycyclic aromatic hydrocarbons, and volatile compounds into the atmosphere that negatively impact on human health.[2] Carbon dioxide is one of these compounds, whose emissions have drastically increased in the last 70 years, rising to 35 billion metric tons in 2020 from barely 5 billion metric tons in 1950.[2] As a result of this emission, the average surface temperature of the earth has increased by approximately 1.1 °C since preindustrial times. Projections estimate a further increase, reaching 1.5 °C in less than 20 years and 2.5 °C - 2.9 °C at the end of the century with the policies adopted until November 2022. According to the Intergovernmental Panel on Climate Change, keeping the global warming to 1.5 °C above preindustrial levels would minimize catastrophic effects.[3,4] Moreover, energy resources can be used as powerful geopolitical and economic weapons by the countries that control them. In history, there are two main cases. The first one, in 1973, by the Organization of Arab Petroleum Exporting Countries (OAPEC), under the leadership of King Faisal of Saudi Arabia, announced an oil embargo against countries that had supported Israel during the Yom Kippur War, and the increase of the oil price leads to a global economy and politics crisis. The second case began in 2022 and continues by Russia; after it invaded Ukraine, it began withholding gas supplies to Europe.[5] Urgent actions are required to be independent of fossil fuels and carry out an energy transition towards renewable energies; for this purpose, *Paris agreements* and the *European Green Deal* were made.[6,7]

A promising alternative energy vector is hydrogen, which can convert, store, and release energy. Depending on the different primary source and the production process used to produce it, hydrogen can be classified by color: grey and blue are produced by steam reforming of natural gas or coal gasification without and with carbon capture, utilization, and storage (CCUS), respectively. Turquoise is produced by pyrolysis of fossil fuels with solid carbon as byproduct; green, purple and yellow are produced from water by electrolysis using electricity from renewable energy sources, nuclear energy and grid electricity, respectively. The color with the lowest impact on the environment, contributing to the decarbonization of the energy system, is the green. Still, the price varies from 2.2 $ to - 8.2 $ per kg of H_2, making it not competitive compared to the grey, 0.8 -2.1 $/kg.[8] To lower the price of green hydrogen, it is crucial the role of electrocatalyst, which speeds up the process and makes it more energy efficient. However, active materials for electrocatalysis are made of critical raw materials.

The European Commission defines critical raw materials (CRMs) as "raw materials of high importance to the economy of the EU and whose supply is associated with high risk".[9,10] They represent the essential prerequisites for the development of strategic sectors such as renewable energy, electric mobility, defense, aerospace, ICT (information and communication technology) and digital technologies.[11] In the fields of

catalysts, the most important CRMs are platinum group metals (PGMs), cobalt, and vanadium. PGMs are especially used in electrolyzers, fuel cells, digital technologies, and robotics. Still, they are mainly supplied from South Africa (the global producer of 94% iridium, platinum, rhodium and ruthenium) and Russia (the global producer of 40% palladium).[12] Ruthenium is particularly important for the electrochemical water splitting, being the state-of-art for the limiting reaction of the chemical process. It is however a CRM, therefore strategies should develop to reduce its use.

Exsolution is a method to increment the efficiency use of ruthenium, which could optimize its atomic use and enhance the activity and the durability of the catalyst. The present Master Thesis aims to investigate the effects of exsolution and subsequent heat treatments at different temperatures on Ru-doped $LaFeO_3$-based perovskite-like materials for the electrocatalytic oxygen evolution reaction (OER), the most challenging step for water splitting. The perovskite-like materials are synthetized through a sol-gel auto-combustion, the calcination temperature is studied by thermogravimetric analysis/mass spectrometry (TGA-MS), crystal structure is characterized by X-ray diffraction (XRD), morphology by scanning electron microscopy (HR-SEM), specific surface area and porosity by N_2 physisorption, and surface chemical composition and environment by X-ray photoelectron spectroscopy (XPS). Electrocatalytic proprieties are investigated through linear sweep voltammetry (LSV) to estimate the overpotential at 5 mA cm^{-2} and Tafel slope, cyclic voltammetry (CV) to calculate the electrochemical active surface area, and electrochemical impedance spectroscopy (EIS) to evaluate the impedance of the catalytic system. The goal is not the research of the best catalyst for OER but rather to understand the effect of the surface reconstruction during the exsolution process of Ru-doped $LaFeO_3$-based perovskite-like catalyst and applied for electrocatalytic water splitting.

This Master Thesis is structured in 6 chapters. *Chapter 1* is an introduction to the role of energy sources and critical raw materials. *Chapter 2* provides an overview of electrocatalysis focused on oxygen evolution reaction, perovskite-type materials, and exsolution. *Chapter 3* is dedicated to the synthesis of Ru-doped $LaFeO_3$-based perovskite-like and thermal treatments. *Chapter 4* presents the experimental results and their discussion. *Chapter 5* illustrates the experimental methods and characterization techniques. Finally, *Chapter 6* draws the conclusion and outlines possible perspectives.

Chapter 2

Electrocatalyst for OER

Notes on Electrochemistry

Electrochemistry originates from the existence of interfaces and their resulting electrical properties. An electrode is an interface between an electronic and an ionic conductor.[13] The fundamental characteristics are the interphase electrification and the possibility to transfer the charge that is inevitably accompanied by an oxidative-reductive chemical process.[14, 15] The interphase electrification is described by Gouy-Chapman-Stern model, when a charged surface is immersed in an electrolyte solution is covered by a double-layer of charges, the internal one is the Stern layer made up by counterions adsorbed on the surface, the external one is the diffusive layer in which there are ions (both counter and co-ions) that interact less with the surface with an average charge opposite to the surface. Overall, the electrical double-layer corresponds to an enrichment of the concentration of counterions (opposite in charge to the surface) and to a depletion of co-ions, compared to the average values of the electrolyte bulk solution. An electrochemical process (**Figure 2.1**) is made up of various steps, at least one of which involves charge transfer (electron transfer). Any step can be the rate-determining step of the process, commonly are the electron or the mass transfer.

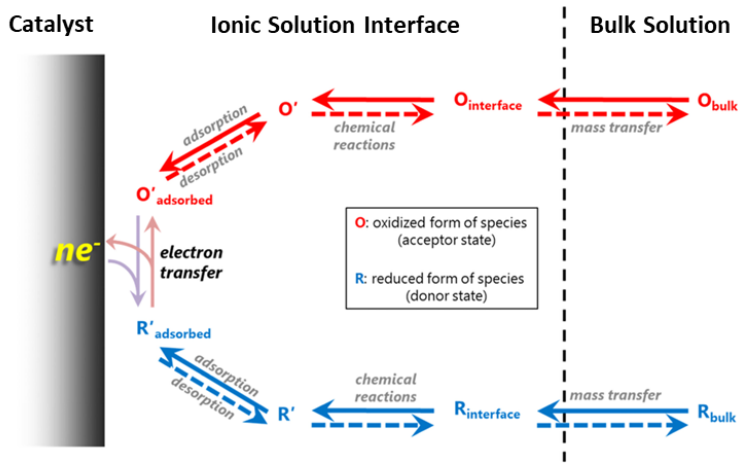

***Figure 2.1**. Schematic representation of an electrochemical process with the steps of mass transport, formation of intermediate, adsorption/desorption and electron transfer.*[16]

A general redox reaction, $O^{z+} + ne^- \leftrightarrows R^{(z-n)+}$, at the equilibrium is described by Nerst equation, **Eqn. 2.1** and the **Eqns. 2.2** and **2.3** present the relations with thermodynamic functions.[17, 18]

$$E_i = E_i^\circ + \frac{RT}{nF} ln \frac{a_O}{a_R} \qquad \textbf{(2.1)}$$

$$E_i = -\frac{\Delta_r G}{nF} \qquad \textbf{(2.2)} \qquad\qquad nFE_i^\circ = -\Delta_r G^\circ = RTlnK \qquad \textbf{(2.3)}$$

E_i: equilibrium redox potential (defined by considering the standard hydrogen electrode that conventionally has zero potential at all temperatures, it consists in a platinum gaze immersed in a a_{H^+}= 1 M solution and a p_{H_2}= 1 bar)
$\Delta_r G$: Gibbs free energy of the reaction
$X°$: X-physical quantity in standard condition (273.15 K, 1 bar)
K: equilibrium constant
R: universal gas constant (8.3145 J K^{-1} mol^{-1})
T: temperature (in Kelvin)
n: number of exchanged electrons
F: Faraday constant (96485 C mol^{-1})
a_x: activity of x-species

There is no net flow of current through the electrode interface at equilibrium potential (E_{eq}), while in non-equilibrium conditions (E) a net current flows. Therefore, it is possible to measure the overvoltage for the electrode under examination at a certain current value, which is defined: $\eta = E - E_{eq}$. The equilibrium potential for a reaction is the thermodynamic minimal potential from which it is possible favoring the reduction or the oxidation but an extra voltage, due e.g. to sluggish kinetics and ohmic loss, is required to have an appreciable current. The η is a descriptor for the activity of the electrocatalysts; indeed, one of their roles is to maintain the overpotential as close to zero as possible to have an appreciable current. The Butler-Volmer model (**Eqn. 2.4**) describes the electrode kinetics, therefore the current density vs overvoltage curve (**Figure 2.2**).[19]

$$j = j_0 \left[\frac{C_R(0,t)}{C_R^*} \exp\left(\frac{(1-\alpha)nF\eta}{RT}\right) - \frac{C_O(0,t)}{C_O^*} \exp\left(-\frac{\alpha nF\eta}{RT}\right) \right] \qquad \textbf{(2.4)}$$

j: net current density
j_0: exchange current density, [20] current that enters and leaves the electrode at E=E_{eq} (anodic and cathodic current are equal and the net current is zero) it reflects the intrinsic rate of the electron transfer
$C_x(0,t)$: concentration t of the x-species on the catalyst surface at the time t
C_x^*: concentration of the x-species in the bulk of solution at the time t
α: electron transfer coefficient,[21] equal to $\Delta_c G^{\neq}/\Delta_r G$ (assumed constant in Butler-Volmer model), where $\Delta_r G = \Delta_c G^{\neq} - \Delta_a G^{\neq}$ and $\Delta_x G^{\neq}$ is the activation energy of cathodic (c) or anodic (a) process, it is an objective descriptor of how the potential variation ΔE and therefore the affects the activation energies of the cathodic and anodic processes

The terms in green are introduced to have a limiting current density (j_l) due to the fact that the mass transfer is the rate-determining step, otherwise the current density would go to infinity.

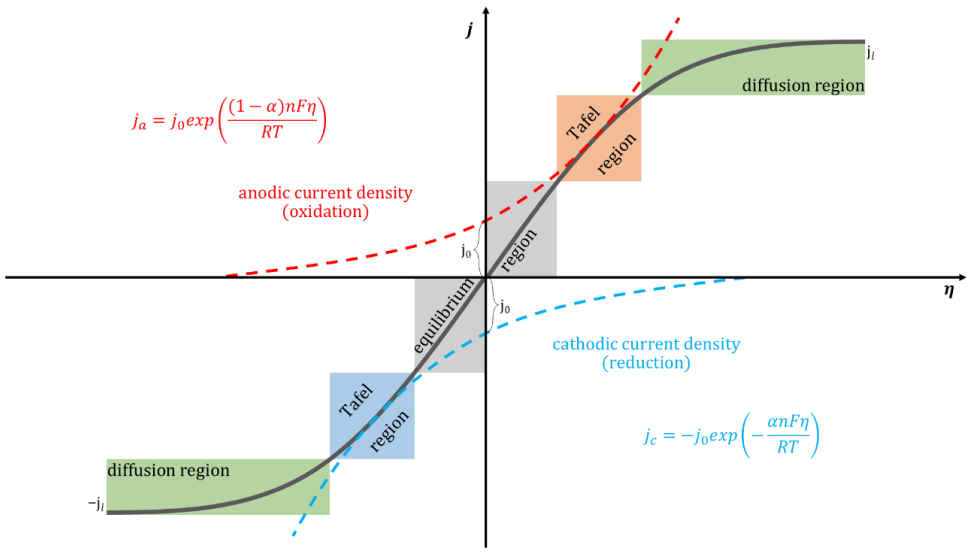

Figure 2.2. *Butler-Volmer plot, j vs η, in solid gray line (α = 0.5). Anodic and cathodic current density in dashed lines, red and sky blue respectively. Equilibrium region in gray where neither the anodic nor the cathodic contribution are negligible, Tafel regions in orange and blue in which the cathodic and anodic current density are negligible respectively, diffusion controlled regions in green where the mass transport is the rate-determining step instep of the electron transfer. Exchange current density given by the intersection of the two current density contributions with the ordinate axis, limiting current density due to mass transfer.*

In the case in which the rate-determining step is the electron transfer, it is possible to rearrange the Butler-Volmer equation and obtain a linear relationship called Tafel law (**Eqn. 2.5**), from the slope of the straight line it is possible to obtain kinetic information of the redox reaction thanks to the presence of electron transfer coefficient α.[13]

$$\eta = a + b ln|j| \qquad \textbf{(2.5)}$$

for reduction: $a = \frac{RT}{\alpha nF} \ln(j_0)$ and $b = -\frac{RT}{\alpha nF}$; for oxidation: $a = -\frac{RT}{(1-\alpha)nF} \ln(j_0)$ and $b = \frac{RT}{(1-\alpha)nF}$

Commonly, Tafel law can be reported with decimal logarithm, making the $log|j|$ explicit (**Figure 2.3**).

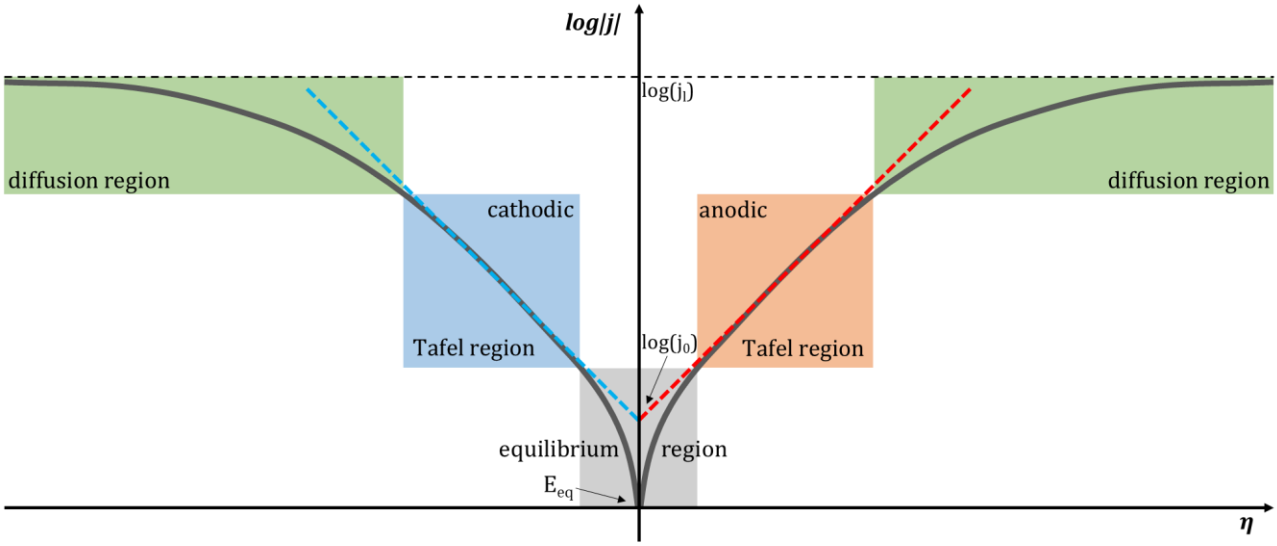

Figure 2.3. *Tafel plot, log|j| vs η, in solid gray line (α = 0.5). Anodic and cathodic Tafel law in dashed lines, red and sky blue respectively. Equilibrium region in gray, kinetically controlled Tafel regions in orange and blue, diffusion controlled regions in green where the mass transport is the rate-determining step instep of the electron transfer. Logarithm of exchange current density is given by the intersection of the two current contributions with the ordinate axis, logarithm of limiting current density due to mass transfer.*

The instrument for measuring and investigating the electrode kinetics is a potentiostat/galvanostat connected to an electrochemical cell (**Figure 2.4**). The electrochemical cell is typically a system of three electrodes immersed in an electrolyte (ionic conductor), and the potentiostat/galvanostat controls the potential/current applied to the electrodes and records the current/potential.

The three electrodes are:[13]

- Working electrode (WE), catalytic material in which the reaction to be studied occurs.
- Counter electrode (CE) closes the galvanometric circuit; a process occurs with a net current equal to and in the opposite direction of that of the WE.
- Reference electrode (RE) closes the potentiometric circuit; there is no current passage through this electrode, thus maintaining the potential fixed and known making it possible to measure the potential difference between RE and WE.

Thanks to this system it is possible to investigate only the process at the working electrode and its proprieties. Typical studied parameters are η at a specific current density, Tafel slope, ECSA and EIS.

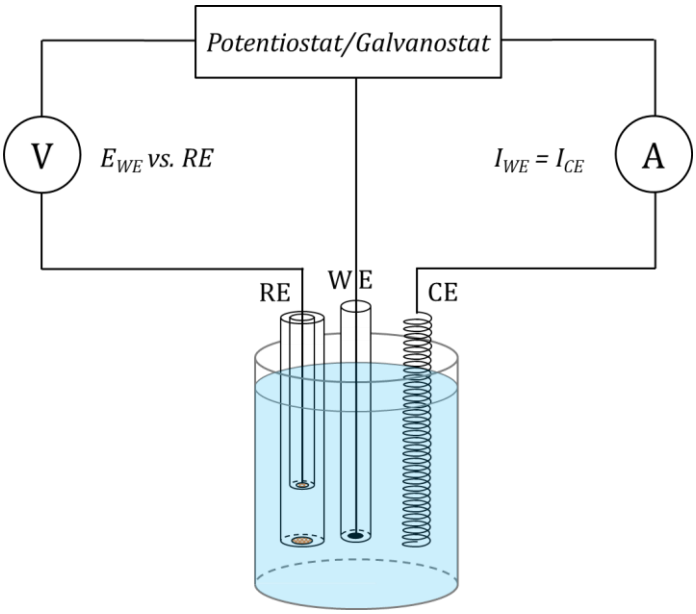

Figure 2.4. *Representation of electrochemical instrument set up, composed by the potentiostat/galvanostat connected to a three electrodes electrochemical cell.*

The linear sweep voltammetry (LSV) in **Figure 2.5** is an electrochemical method to study a reaction kinetics. In LSV the WE potential varies linearly over the time (with respect to RE); therefore, the scan rate is constant. The scan begins from an initial potential where no electrochemical processes occur and finishes at a final potential while the current density is recorded.[22]

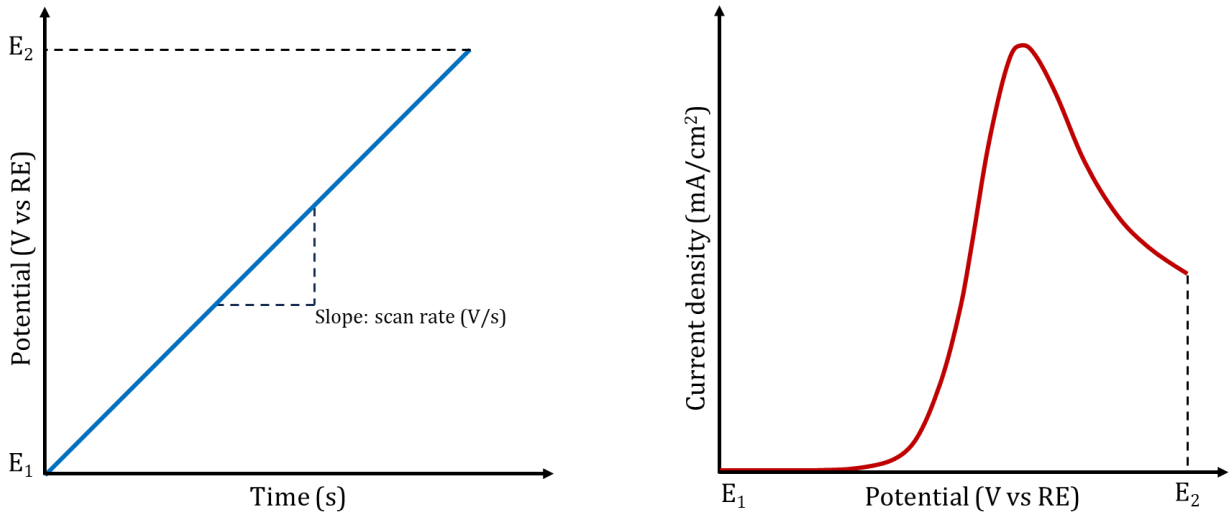

Figure 2.5. *Linear potential scan from E_1 to E_2 (left) and the linear sweep voltammetry (right).*

In LSV curve, the current density is initially zero until the potential reaches a value at which the electron transfer occurs with an appreciable speed, which is the rate-determining step. The current increases as the overpotential becomes more positive, making the electron transfer faster. At a certain potential the curve reaches its current density peak; around this peak, the system is a mixed-controlled regime; after, the electron transfer becomes too fast and the process enters in the mass-controlled regime, so the current decreases because the concentration of the reagent on the electrode surface is zero. In the electron transfer region, it is possible to perform analysis via Tafel analysis and obtain kinetic information.

The potential is conventionally reported with reference to the reversible hydrogen electrode (RHE), a subtype of standard hydrogen electrode whose potential does not change with the pH. To convert the potential the Nerst equation is used, **Eqn. 2.6** reported the case of an Ag/AgCl electrode as RE.[23]

$$E_{RHE} = E_{AgCl} + 0.059pH + E^{\circ}_{AgCl} \qquad \textbf{(2.6)}$$

$$(E^{\circ}_{AgCl} = 0.198\,V\ vs\ RHE, \qquad T = 25\,^{\circ}C)$$

Another type of voltammetry is the cyclic voltammetry (CV), similar to LSV. However, after reaching the final potential, the scan returns at the initial potential with the same rate, giving the typical triangular profile of the curve potential vs time. In this study, CVs are used to evaluate the electrochemical active surface area (ECSA), determined from the double-layer capacitance (C_{DL} in µF) and the specific capacitance of any investigated electrode material (C_S in µF cm^{-2}) according to **Eqn. 2.7**.[24]

$$ECSA = \frac{C_{DL}}{C_S} \qquad \textbf{(2.7)}$$

When an electrode surface is subjected to a voltage ramp (scan rate: v), a steady-state capacitive current is observed in a short time (i_C) if the only process taking place within the voltage range is the charging of the double-layer, that is, movement of ions on either side of an electrode/electrolyte interface, for ideal capacitors, i_C described in **Eqn. 2.8**. A common method for obtaining the double-layer capacitance consists in recording cyclic voltammograms at various scan rates within a potential region where no faradic processes take place, extracting i_C from the anodic and cathodic scans of the recorded voltammograms, and subsequently extracting C_{DL} from the slope of the resulting i_C vs v plot (**Figure 2.6**).[25]

$$i_C = v \cdot C_{DL} \qquad \textbf{(2.8)}$$

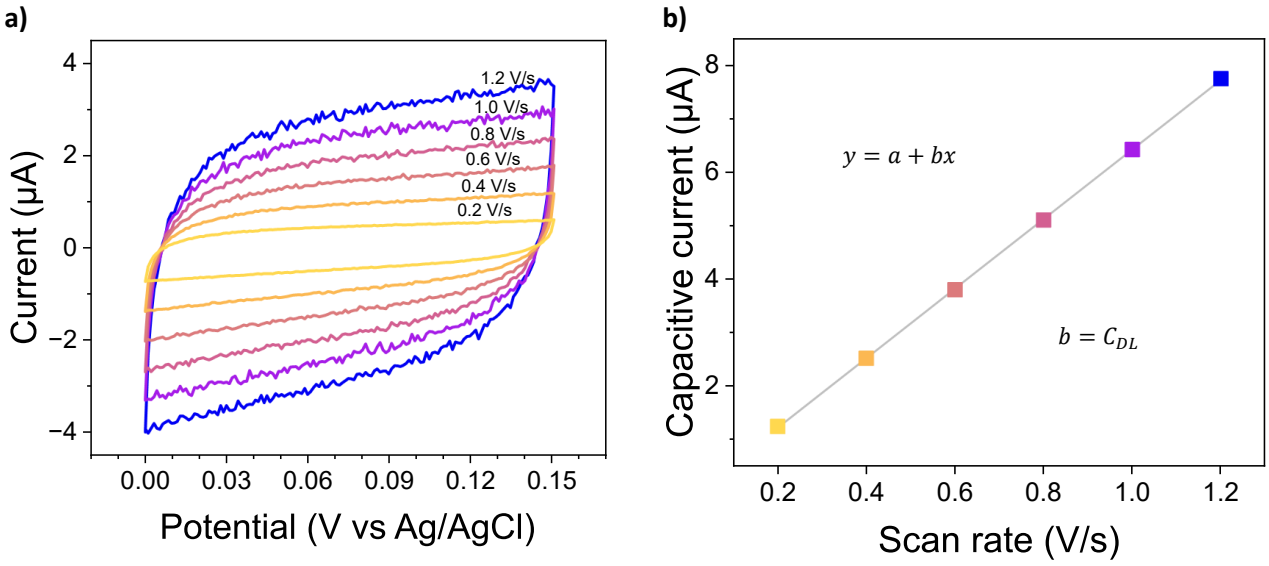

Figure 2.6. a) *CVs at different scan rate (0.2, 0.4, 0.6, 0.8, 1.0 and 1.2 V/s) in a non-faradic region for the catalyst L0.9FR_750c_600e_400m.* ***b)*** *i_C vs v plot, linear regression in grey whose angular coefficient is C_{DL}.*

The specific capacitance of the sample corresponds to the capacitance of an atomically smooth planar surface of the material per unit area under identical electrolyte conditions as the studied material. While ideally one would synthesize smooth, planar surfaces of each catalyst to measure C_s and estimate ECSA, this is not practical for most electrodeposited systems. However, specific capacitances have been measured for a variety of metal electrodes in acidic and alkaline solutions and typical reported values range between C_s = 15−110 μF cm^{-2} in H_2SO_4 and C_s = 22−130 μF cm^{-2} in NaOH and KOH solutions, and a typical value in alkaline environment is 40 μF cm^{-2} (value used in the present work).[26]
Moreover, when CV is performed including a faradic region in the scan potential, it is possible to investigate the kinetics of a redox reaction like with LSV, and obtain other useful information on the reaction, such as if the process is adsorptive or diffusive, and for the latter to distinguish if it is reversible or irreversible.[27, 28]

Electrochemical impedance spectroscopy (EIS) is a powerful tool to investigate properties of materials and electrode reactions.[29, 30] It is performed by applying a time-dependent sinusoidal voltage $V(t)$ (with a certain amplitude V_0 and angular frequency ω) to the WE and recording the output current signal $I(t)$. In the case of sufficiently low V_0, a linear approximation can be retained, and the sinusoidal output current will have the same frequency of the applied voltage and a possible phase shift θ. The impedance $Z(\omega)$ represents the total opposition to the current flow in an electrical circuit and can be considered as a generalization of the resistance from the Ohm's law ($R = V/I$), as it takes into account the dependency on the frequency, therefore can be expressed by the transfer equation that relates the input and output signals, **Eqn. 2.9**.

$$Z(\omega) = \frac{V(t)}{I(t)} = \frac{V_0 \sin(\omega t)}{I_0 \sin(\omega t + \theta)} = Z_0 \frac{\sin(\omega t)}{\sin(\omega t + \theta)} \qquad \textbf{(2.9)}$$

Using Euler relationship, the impedance $Z(\omega)$ can be separated in real and imaginary part, **Eqn. 2.10**, using which the magnitude and phase angle can be calculated, **Eqns. 2.11** and **2.12**.

$$Z(\omega) = Z_0 \frac{e^{j\omega t}}{e^{j(\omega t + \theta)}} = Z_0 e^{-j\theta} = Z_0(cos\theta - jsin\theta) = Z_{Re} - jZ_{Im} \qquad \textbf{(2.10)}$$

$$|Z| = \sqrt{(Z_{Re})^2 + (-Z_{Im})^2} = \left(\frac{1}{Z_{Re}} - \frac{1}{Z_{Im}}\right)^{-1} \qquad \textbf{(2.11)}$$

$$\theta = \tan^{-1}\frac{Z_{Im}}{Z_{Re}} \qquad \textbf{(2.12)}$$

A common way to report the impedance is the Nyquist plot ($Z_{Im}\ vs\ Z_{Re}$) shown in **Figure 2.7a** with the typical semicircle profile. This type of data representation allows for a facile analysis of the impedance response, even if the information on the frequency is lost. EIS data are analyzed by fitting the Nyquist plot with an equivalent electrical circuit. The electrical elements in the model (commonly resistors, capacitors, and inductors) should have a basis in the physical electrochemistry of the system. In a DC circuit, the current flow is hindered only by resistors, while in AC circuit, it is also hindered by capacitors and inductors. One of the equivalent circuits used to describe a simple electrocatalytic system in a 3-electrode electrochemical cell is the simplified Randles cell (diagram in **Figure 2.7b**). [31]

When a sinusoidal voltage input is applied to a resistor, the resulting current follows the AC voltage without delay, and $V(t)$ and $I(t)$ are in-phase ($\theta = 0$), **Eqn. 2.13**. The impedance of a resistor is independent on the frequency and contains only the real part equal to the resistance of the resistor, $Z_R = R$. The Nyquist plot of

a pure resistive response of a system will only be a point on the x axis in correspondence of the value of the respective resistance.

$$I(t) = \frac{V(t)}{R} = \frac{V_0 \sin(\omega t)}{R} = I_0 \sin(\omega t) \qquad \textbf{(2.13)}$$

On the other hand, when $V(t)$ is applied to a capacitor the $I(t)$ has a phase shift is $\pi/2$, **Eqn. 2.14**. Only the imaginary part of the impedance of a capacitor is affected, resulting in $Z_C = \frac{1}{j\omega C}$. The Nyquist plot of a pure capacitive response will be a line along the y-axis.

$$I(t) = C\frac{dV(t)}{dt} = \omega C V_0 \cos(\omega t) = \omega C V_0 \sin\left(\omega t + \frac{\pi}{2}\right) \qquad \textbf{(2.14)}$$

The simplified Randles equivalent circuit is made by a resistor R_s connected in series to a sub-circuit of a resistor R_{ct} and capacitor CPE connected in parallel; the impedance of this model is expressed by **Eqn. 2.15**.

$$Z(\omega) = R_s + \frac{R_{ct}}{1 + j\omega CPE} \qquad \textbf{(2.15)}$$

R_s represents the ohmic series resistance, mainly caused by the uncompensated electrolyte resistance and the connection of the electrodes to the instrument. CPE is the constant phase element and represents the electrical double-layer capacitance of the catalyst. In contrast, electrode's charge transfer (or polarization) resistance is represented by R_{ct}. In the Nyquist plot, the imaginary parts of the start and the end of the semicircle are zero and represent two values of the impedance of resistor, R_s and (R_s + R_{ct}) respectively. Indeed, at very high frequency, the impedance of the capacitor tends to zero and all the current flows through R_s and CPE, while, at very low frequency, CPE tends to infinity and all the current flows through R_s and R_{ct}. At intermediate frequency the current flows in all the electronic components, and the maximum semicircle function is at $\omega = 1/R_{CT}CPE$.

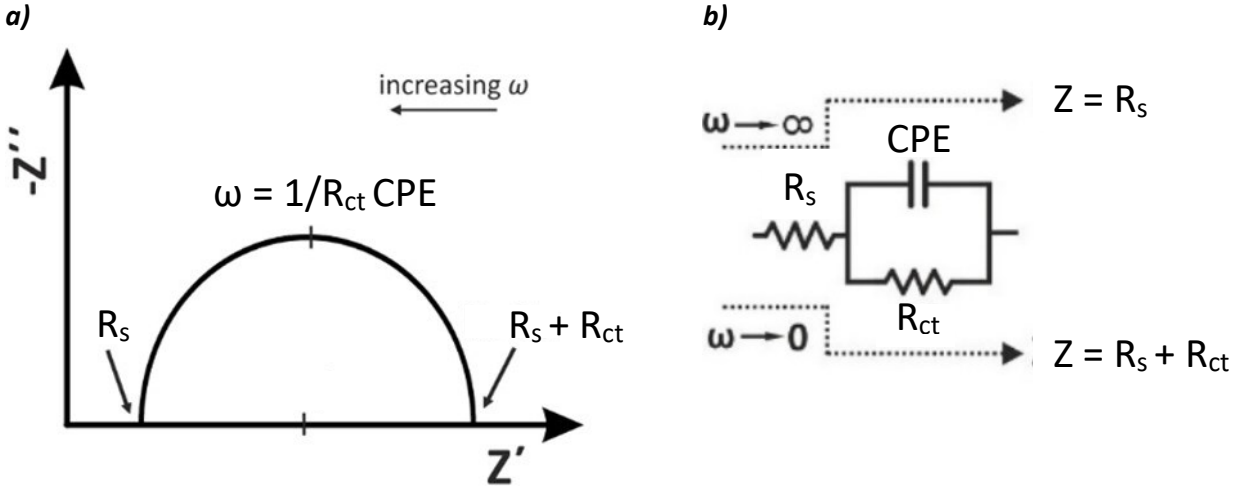

Figure 2.7. a) *Nyquist plot (Z_{Im} vs Z_{Re}) of the near model.* ***b)*** *Diagram circuit of simplified Randles model.*[31]

Oxygen Evolution Reaction

Water splitting, **Eqn. 2.18**, is a highly promising, environmentally friendly approach for hydrogen production. As a redox reaction, water splitting consists of two half-cell reaction: the HER (hydrogen evolution reaction), in **Eqn. 2.16**, and the OER (oxygen evolution reaction) in **Eqn. 2.17**, which produce hydrogen and oxygen at the cathode and anode, in an electrolyzer respectively (**Figure 2.8**), electrochemical device that converts electric energy in chemical energy. The equilibrium potential (thermodynamic potential) for HER is 0 V vs RHE, while for OER is +1.23 V vs RHE; therefore water is thermodynamically stable in this voltage window 1.23 V wide (**Figure2.9**).[32, 33]

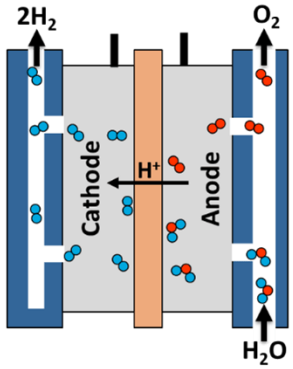

Figure 2.8. *Illustration of an electrolyzer for water splitting: the reagent is water, and the products are hydrogen and oxygen.*[34]

HER: $2H^+(aq) + 2e^- \rightarrow H_2(g)$ x2 **(2.16)**

OER: $2H_2O(l) \rightarrow O_2(g) + 4H^+(aq) + 4e^-$ **(2.17)**

$$2H_2O(l) \rightarrow 2H_2(g) + O_2(g) \quad \textbf{(2.18)}$$

$\Delta E° = E°_{anode} - E°_{cathode} = 1.23$ V

$\Delta G° = 237.2$ kJ mol^{-1}

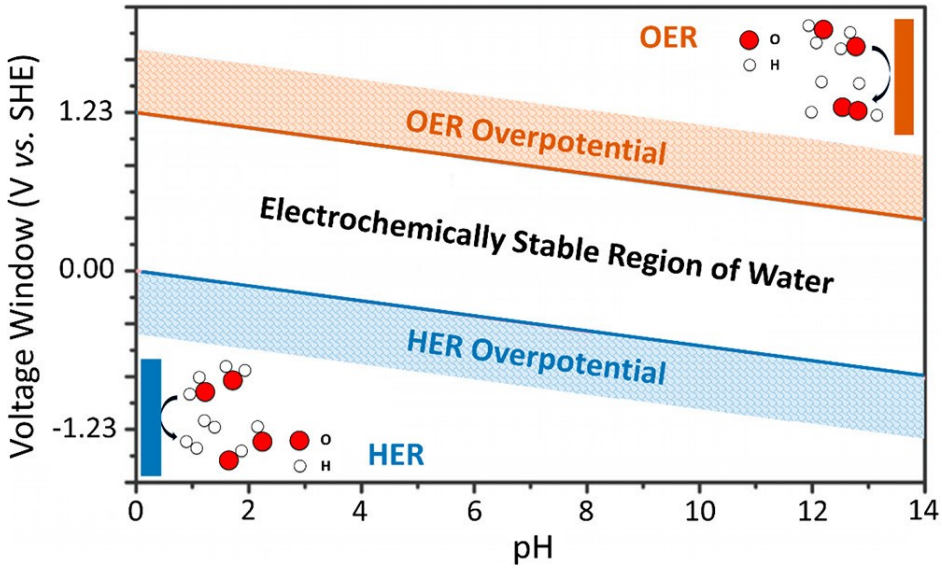

Figure 2.9*. Pourbaix diagram of water. The orange line and blue line indicate the upper and lower thermodynamically stable potentials as a function of pH values, where the orange and blue areas represent the overpotentials toward water oxidation (OER) and water reduction (HER), respectively.*[35]

The major bottleneck is OER due to the sluggish kinetics of this four-electrons transfer reaction; moreover, OER involves more complex reaction mechanisms compared to the HER, where many intermediates and radical species are involved, such as hydroxyl radicals (•OH) and active oxygens (O*), making the reaction more susceptible to energy losses and side reactions, increasing the overpotential required to favor the reaction. Electrocatalysts play a key role by facilitating the required electron transfer, and the formation and breaking of chemical bonds, lowering the activation energy and speeding up the reactions. Transition metal oxide electrocatalysts (such as perovskite, spinels, rock salt, and rutile) sparked intensive interest in catalyzing the OER with impressive activity, thanks to their low cost and superior oxidation resistance in alkaline electrolyte and, particularly upon high oxidation potentials during the OER.[36] The difference between the potential at which the catalyst operates at a specific current under specific conditions and the equilibrium potential for a given reaction is defined as overpotential. In alkaline media the OER follows **Eqn. 2.19**.

$$4OH^- \rightarrow O_2 + H_2O + 4e^- \quad \textbf{(2.19)}$$

A general mechanism for OER is the adsorbate evolution mechanism (AEM), which is typically assumed to involve four concerted proton-electron transfer reactions centered on the metal ion. A proton is injected into the electrolyte at each step, eventually combining with a transferred electron at the cathode. In particular, OH^- first adsorbs on the active site (*) to generate *OH radical (**Eqn. 2.20**). Then, *OH deprotonates to produce *O, which is accompanied by the release of an electron and a water molecule (**Eqn. 2.21**). After that, the nucleophilic attack of OH^- on *O yields the intermediate *OOH (**Eqn. 2.22**). Finally, a further proton-coupled-electron transfer process results in the generation of one oxygen molecule as well as a free active site (**Eqn. 2.23**).[36]

$$* + OH^- \rightarrow *OH + e^- \quad \textbf{(2.20)}$$

$$*OH + OH^- \rightarrow *O + H_2O + e^- \quad \textbf{(2.21)}$$

$$*O + OH^- \rightarrow *OOH + e^- \quad \textbf{(2.22)}$$

$$*OOH + OH^- \rightarrow * + O_2 + H_2O + e^- \quad \textbf{(2.23)}$$

Other materials, like perovskite, prefer the lattice oxygen participation mechanism (LOM). The dehydrogenation of *OH on the oxygen anion sites produces *OO species and V_O (**Eqn. 2.24**), then the *OO species evolves back to *OH, while releasing O_2 and electrons (**Eqn. 2.25**). V_O is re-occupied by *OH during this step, and an adjacent surface lattice oxygen is protonated (**Eqn. 2.26**). Finally, *OH is regenerated during deprotonation (**Eqn. 2.27**).[36]

$$*OH + OH^- \rightarrow (V_O + *OO) + H_2O + e^- \quad \textbf{(2.24)}$$

$$(VO + *OO^-) + OH^- \rightarrow O_2 + (VO + *OH) + e^- \quad \textbf{(2.25)}$$

$$(VO + *OH) + OH^- \rightarrow (OH^- + *OH) + e^- \quad \textbf{(2.26)}$$

$$(OH^- + *OH) + OH^- \rightarrow *OH + H_2O + e^- \quad \textbf{(2.27)}$$

In both mechanisms, AEM and LOM, any possible elementary step can be the rate-determining depending on the material and the pH of the medium. A schematic catalytic cycle of these two mechanisms is presented in **Figure 2.10**.

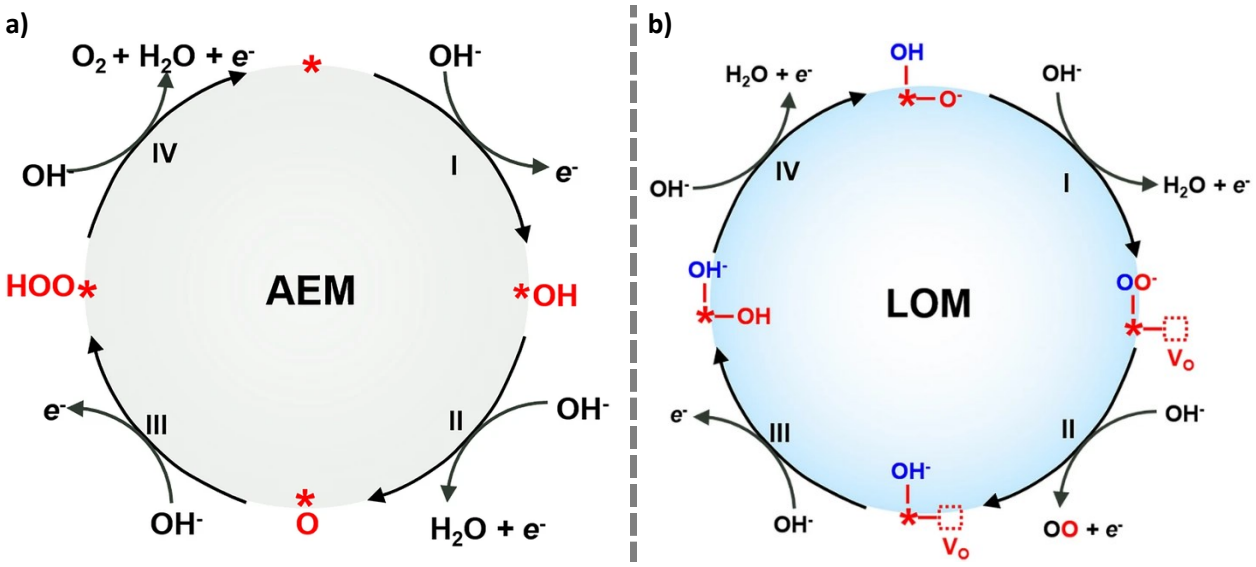

Figure 2.10. *The OER catalytic cycle based on* ***a)*** *AEM and* ***b)*** *LOM. Here, * represents the surface-active TM cation, and the red dotted square represents the oxygen vacancy V_O. The four elementary steps I, II, III, IV correspond to Eqns. 2.20–2.23 and 2.24-2.27 respectively.*[36]

According to these conventional OER mechanisms on transition metal oxides, all of the intermediates interact with the surface of transition metal oxides through an oxygen atom, and the bonding interactions (M-O, M is a catalytically active metal center) within the intermediates (MOH, MO, and MOOH) are crucial for the overall OER activity.[37] Sabatier's principle suggests that for a heterogeneous chemical reaction it is possible to plot the rate constant versus the adsorption energy (ΔG_{ads}) of the chemical species which assumes a typical volcano shape. In electrocatalysis, the volcano graph is constructed by reporting the activity of the catalyst (such as the current density of the overpotential) on the ordinate and on the abscissa the bond distance M-adsorbed species determined, for example, by X-ray diffraction (XRD) or X-ray absorption (XAS) measurements or the ΔG_{ads} (or the ΔH_f) determined by DFT calculations.[38] The volcano trend for a catalyst implies that the activity will have its maximum value when the bonding strength is not too large but not too much small (**Figure 2.11**).

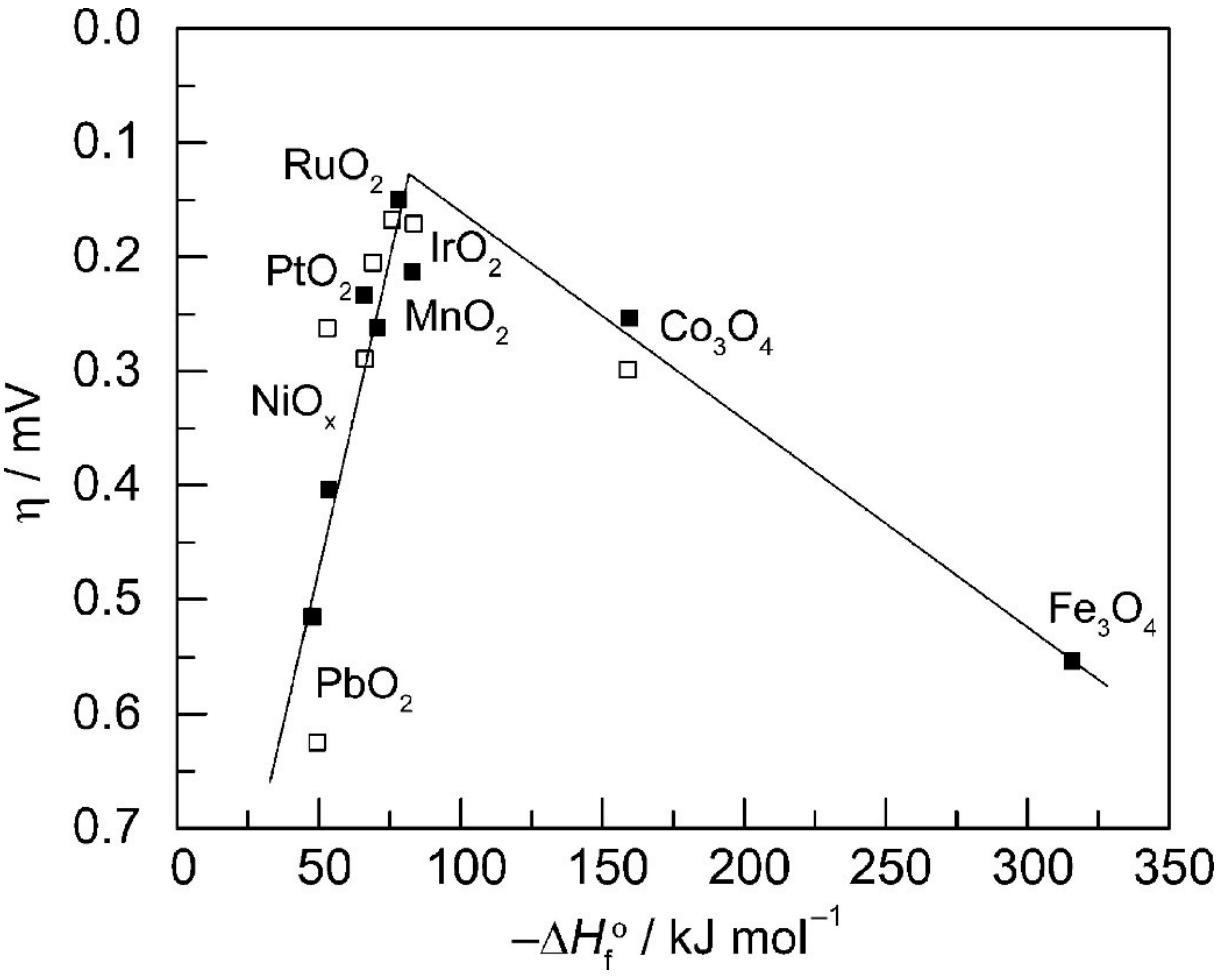

Figure 2.11. *Volcano plot showing activity for O_2 production on metal oxide surfaces versus the enthalpy of transition of the oxide in acidic (■) and basic (□) solution. Overpotential measured relative to 0.1 mA cm^{-2} current density.*[39]

On the ascending part of the volcano plot are the oxides with weaker interaction with oxygen, so the adsorption is more difficult, making the catalysis inefficient. On the descending part there are the oxides with a stronger interaction with the oxygen: the easier the adsorption of OH and the more difficult the desorption of O_2 becomes, blocking the active site. On the apex of the volcano there is RuO_2 followed by IrO_2 that have an oxygen adsorption energy neither too low nor too high: these two oxides represent the state of art of oxygen evolution reaction. They can efficiently electrocatalyze the OER, but their low-reserves and high-cost limit their large-scale commercial utilization.

However, the OER mechanism varies for different oxides having different surface morphology. Oxides with similar compositions display different kinetics due to differences in preparation methods leading to different structures and thickness of their oxide layers.

Ru- and Ir- based materials

Ru- and Ir-based materials are the best performers for OER. Cherevko et al. studied the activity and the stability of metallic and oxidized Ru and Ir thin film electrodes in acid and alkaline conditions; their major results are presented in **Figure 2.12**.[40]

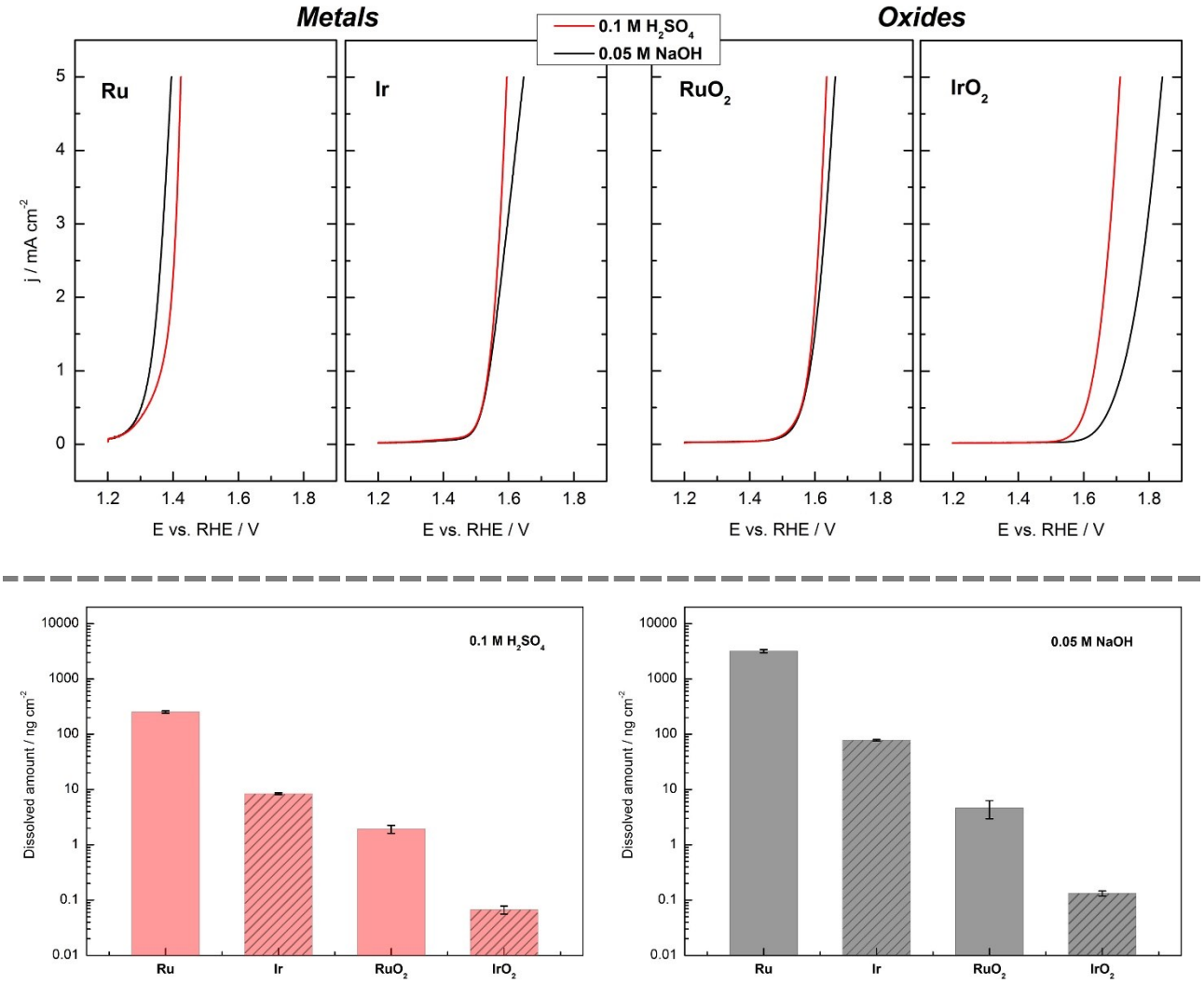

Figure 2.12. *On the top, the current–potential curves starting from E = 1.2 V vs RHE and going to the anodic direction for Ru, Ir, RuO_2, and IrO_2. Scan rate: 10 mV s^{-1}. Electrolyte: 0.1 M H_2SO_4 (red lines) and 0.05 M NaOH (black lines). On the bottom, amount of dissolved metal from Ru, Ir, RuO_2, and IrO_2 electrodes in the same conditions presented on the top.*[40]

Both metals achieve significant current densities at a lower potential than the oxides, but their dissolution rate is too high to be used as electrocatalysts, particularly in alkaline media. Meanwhile, the metal oxides present a good stability in both acid and alkaline conditions, with the overpotential of RuO_2 being lower than IrO_2. From the current-potential curve of RuO_2 in basic media (case of interest), it can be estimated the overpotential at 5 mA cm^{-2} which is roughly 430 mV. As said, the morphology plays a crucial role, and a RuO_2 mesoporous double gyroid thin film reaches an overpotential at 5 mA cm^{-2} of about 170 mV.[41] Many studies and novel materials target the performance standards given by ruthenium oxide, but it undoubtedly remains the benchmark material for OER; however, Ru is a critical raw material, so price and availability limit its usage. A possible solution to reduce the dosage of noble metals for catalytic applications is through stable hybrid systems made of supported Ru-based NPs, e.g. performing an exsolution process on a Ru-doped perovskite-type material.

Perovskite-type materials

The term "perovskite" refers to the mineral of $CaTiO_3$, discovered by Gustav Rose and named by the Russian mineralogist Luv Perovski. In contrast, the term "perovskite-type (or like)" is referred to all the materials with a formula ABX_3 or A_2BX_4 (the latter are called double perovskites),[42] even if only "perovskites" is commonly misused to indicate this class of materials. The family of perovskites are candidates for energy transition, the main fields of application being catalysis, solar cell, optoelectronics, and SOFC.[43–46] The wide application potential is given by the wide compositional and structural variability. In fact, more than 90% of metallic elements are stable in the perovskite structure, characterized also by easily tunable proprieties, high stability and typical low cost. In the formula ABX_3, A and B are two metal cations with A being larger than B; the A cation can be a lanthanide, alkaline, or alkaline-earth cation, while the B cation is typically a metallic element from the 3d, 4d, or 5d configuration, and X commonly is oxygen, but it can also be chlorine or fluorine.[47] Recently hybrid organic-inorganic perovskites have been studied for flexible solar cell (e.g. $CH_3NH_3PbI_3$).[48,49] The ideal crystalline structure is cubic with A in cuboctahedral and B octahedral coordination. Still, there are many deviations, important geometric factors that determine stability are the octahedral factor in **Eqn. 2.28** (stable octahedra have a value > 0.41), and the Goldschmidt factor in **Eqn. 2.29**, useful for predicting the structure that will occur based on the combination of cations (**Figure 2.13**).[50]

$$\mu = {}^{r_B}/_{r_X} \qquad > 0.41 \qquad \textbf{(2.28)}$$

$$t = \frac{r_A + r_X}{\sqrt{2}(r_B + r_X)} \qquad 0.9 < t_{cubic} < 1 \qquad \textbf{(2.29)}$$

In addition to the cubic structure, perovskite-like materials can occur in other different crystalline structure and are stable above 0.75 of the Goldschmidt factor; below this value the dimensions of the cations are almost identical and another group of materials, Ilmenite (e.g. $TiFeO_3$), instead is formed. For Goldschmidt factor between 0.9 and 1, the cubic one is stable (e.g. $SrTiO_3$); if the dimensions of A and B are too different, there is a tolerance factor greater than 1 (e.g. hexagonal $BaNiO_3$, tetragonal $TiPbO_3$), in the opposite case the tolerance factor is lower than 0.9 (e.g. orthorhombic $GdMnO_3$, rhombohedral $LaMnO_3$).

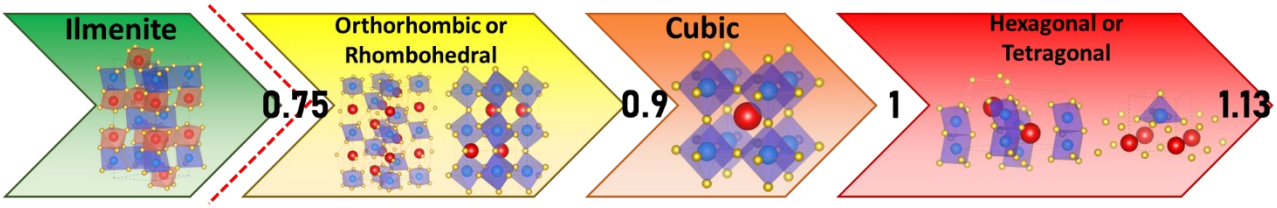

Figure 2.13. *Evolution of the crystalline structure with the increasing of Goldschmidt factor. A-cations are represented with red spot, B-cations with the blue one and oxygen in yellow.*

However, this factor is valid in broad terms: numerous other factors can distort the structure, such as polar cation displacements, Jahn-Teller effect, octahedra tilts, temperature and pressure.[51] The structure determines many properties of the perovskite such as ionic and electronic conductivity, which can also be tunable thanks to doping. The role of A-site cation is mainly structural in lanthanides perovskites, whereas B-site elements determine the catalytic activity. Due to the minor effects of the A site cations on catalysis and its high abundance, La-based perovskite oxides have been the most frequently studied.[52] Interesting B-cations are Co, Ni, Cu, Cr, Mn and Fe; the latter in general possess the lower catalytic activity in the group but, thanks to its high availability, low price of iron precursors and negligible toxicity, interest on this cation remains constant.[53] For the future, perovskites are very promising alternatives for PGMs in various catalytic

applications, mainly due to their ease of synthesis and low cost compared to PGMs and the extraordinary capability of their structure to accommodate a wide range of substituting and doping elements, allowing tailoring their properties to better targeting their applications. Furthermore, the catalytic performance of these materials could be improved by making composites or exploiting nanoparticle exsolution techniques.[54] However PGMs remain the better option in performance for catalysis and a strategy to optimize their use is through exsolution. Excellent parent oxides for the exsolution process are $LaFeO_3$-based perovskites,[55] very stable materials whose components are abundant (at low price) and their lack of intrinsic activity can be improved by using ruthenium.

Exsolution

In the exsolution method the active (i.e., exsolvable) elements are substituted in a host lattice under oxidizing conditions, forming an oxide solid solution, and released as metallic particles upon exposure to reducing conditions, leaving behind the host lattice as support (**Figure 2.14a**). The most common crystal structure that supports the formation of solid solution used for exsolution is the perovskite lattice (but also fluorite, spinel, and rutile can be exploiled). In perovskite-type materials, the A-site cation has a very high ΔG of reduction, making them non-reducible to a metallic state in typical conditions; therefore generally, only the B-site cations are exsolved, and very reducible ions are noble metals. Since the exsolution occurs under a reducing atmosphere, a general driving force of exsolution is an oxygen vacancy formation in the perovskite oxides. The oxygen vacancy formation destabilizes the lattice stoichiometry, causing the segregation of B-site cations to maintain structural stability. Several driving forces, such as temperature, non-stoichiometry by A-site defect, voltage biasing, strain, phase transition, and topotactic ion exchange, have been introduced to form the oxygen vacancy.[56] Therefore, exsolution is a chemically driven heterogeneous phase transition, arising from the four physical processes of diffusion, reduction, nucleation, and growth (**Figure 2.14b**). Exsolving dopant cations first diffuse from the bulk to the surface and then are reduced to metal. Reduced metals are assembled into small nanoparticles that grow in size on the surface.

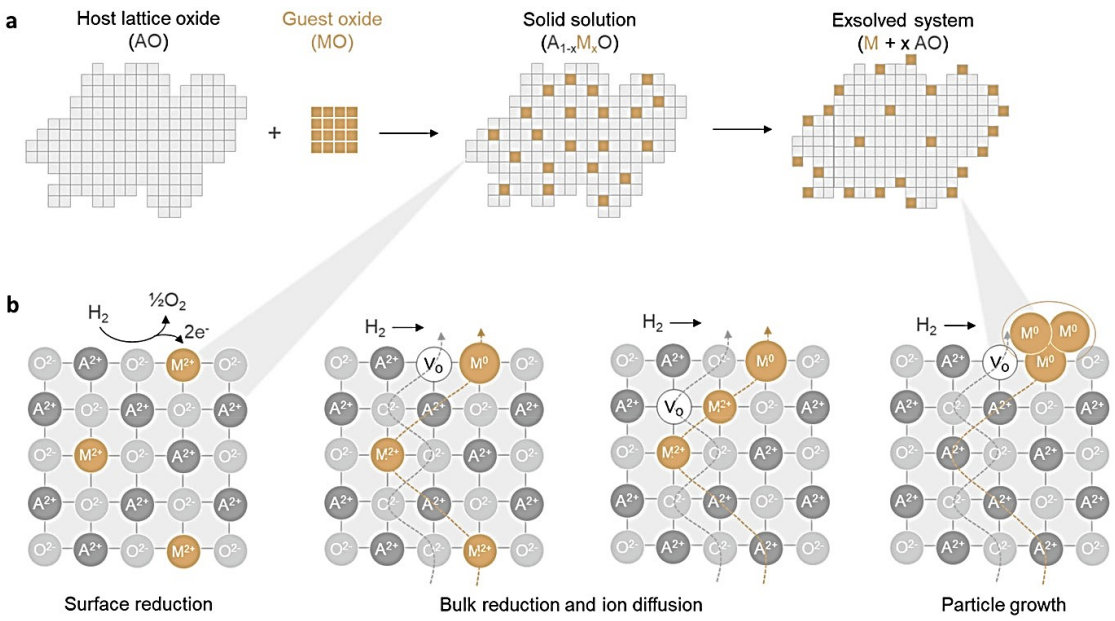

Figure 2.14. *A schematic illustration of the process.* ***a)*** *The exsolution method and* ***b)*** *key processes fundamental to exsolution.*[57]

Exsolution, like impregnation, leads to a nanocomposite system made by supported nanoparticles, but differently how impregnation, it is less wasteful in terms of precursor requirements, occurs in a single step, offers a better control of the process, it is cheaper and generally faster. Moreover, the exsolved NPs have unique proprieties not obtained through impregnation; indeed they are partially embedded ("socketed") in the support phase and there is a crystallographic alignment between the exsolved and host phases. [57] The socketed epitaxial NPs has proven to unlock many unique properties which make the system more stable and durable:

- Resistance towards agglomeration and poisoning.[58]
- Higher activity with respect to the normal deposited counterparts (socketing induced strain).[59]
- Regeneration: in some cases the exsolution is reversible and the NPs can redissolve in the substrate lattice regenerating the original material (**Figure 2.15**).[60,61]

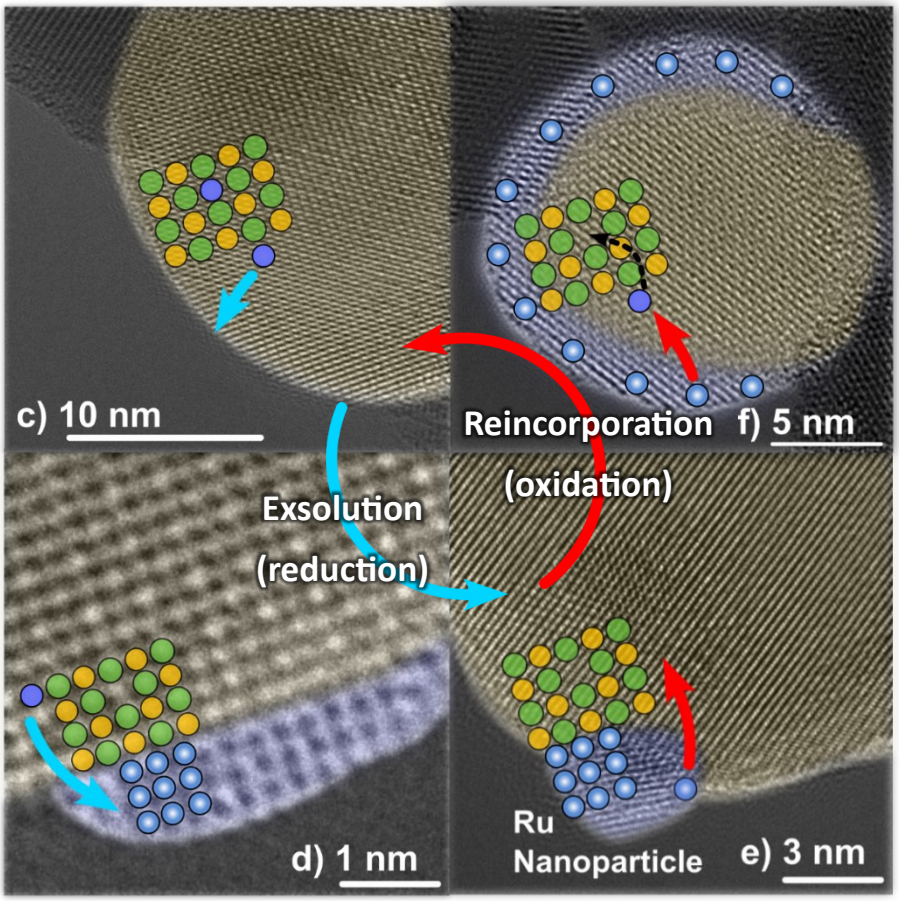

Figure 2.15. *TEM images of $LaFe_{0.9}Ru_{0.1}O_3$* ***(c)*** *that undergoes to exsolution* ***(d, e)*** *and reincorporation* ***(f)****. Green and yellow spot represent the parent oxide lattice, while the blue ones represent ruthenium atoms. Image provided by Dr. Jaime Gallego.*

The morphology of the materials plays an important role in exsolution. In high specific surface area powders or thin films, surface nucleation would be more important than ion diffusion, since the distances the ions would be required to travel to the surface would be shorter. On the other hand, surface restructuring phenomena could be more prominent in these samples and thus could hinder exsolution. At the same time, aspects such as a high specific surface area, porosity, and structural defects could promote exsolution at low temperatures. In porous and high specific surface area material the diffusion exsolution pathway is shorter, so shorter time and lower temperature are needed for the process. The pores limit the NPs dimension leading to higher particle numerical density, and thus a higher surface of the exsolved material; if this material is catalytically active, the performances increase. Therefore, using mesoporous materials for electrocatalysis benefits both in mass transport, as well known, as well as in activity by promoting exsolution.

In **Table 2.1**, various significative lanthanum ferrite-based perovskites are reported with their overpotential at 10 mA cm^{-2} for OER in alkaline media, before and after exsolution, with additional oxidation treatment where indicated. These perovskites are usually doped with cobalt as a non-noble metal and ruthenium to increase the activity for OER. There are several examples in which exsolution has a positive effect on the performances of the original perovskites and in some cases, successive oxidation can further increase them, but both can also lead to a worsening of the catalytic performances.

Perovskite	η_{10} (mV) *Before*	**Treatments**	**NPs composition**	η_{10} (mV) *After*	**Ref.**
$La_{0.9}Co_{0.1}Fe_{0.9}O_3$	430	5% H_2/Ar at 500 °C for 3 hours	CoFe alloy	400	62
$La_{0.9}Co_{0.2}Fe_{0.8}O_3$	440	5% H_2/N_2 at 350 °C for 2 hours	Co	417	63
$La_{0.95}Co_{0.2}Fe_{0.8}O_3$	402	5% H_2/Ar at 500 °C for 4 hours	CoFe alloy	452	64
		5% H_2/Ar at: 600 °C 700 °C 800 °C for 4 hours	Co	400 377 378	
$(La_{0.8}Sr_{0.2})_{0.9}Co_{0.1}Fe_{0.9}O_{3-\delta}$	480	5% H_2/Ar at 800 °C for 3 hours	CoFe alloy	371	65
$(La_{0.8}Sr_{0.2})_{0.9}Co_{0.1}Fe_{0.8}Ru_{0.1}O_{3-\delta}$	393	5% H_2/Ar at 800 °C for 3 hours	CoFeRu alloy	347	
$La_{0.9}FeO_{.92}Ru_{0.08}O_{3-\delta}$	480	5% H_2/N_2 at 600 °C for 15 hours	Ru	430	66
		+ oxidation in air at 500 °C for 1 hour	Ru/RuO_2	380	
$La_{0.9}Fe_{0.92}Ru_{0.08}O_3$	490	5% H_2/Ar at 550 °C for 5 hours	Ru	460	67
		+ oxidation in air at: 400 °C 550 °C for 4 hours	Ru/RuO_2	420 480	

***Table 2.1**. Summary of results in exsolution and post-treatments on lanthanum ferrite-based perovskites for OER in alkaline media.*

Inspired by these cited studies, in particular from that of Jiang et all,[67] on which the present work is based, whose aim is not to identify the best catalyst for OER, but rather to provide a comprehension on the effects of the exsolution process and of the post-oxidation treatments in lanthanum ferrite based perovskite, more precisely in Ru-doped ones, so on how to optimize the noble metal content.

Chapter 3

Synthesis and Heat Treatments

Sol-Gel auto-combustion

Ru-doped La-Fe perovskite-type powders are obtained through sol-gel auto-combustion.

The sol-gel process is a bottom-up method to obtain ceramic materials.[68,69] Typically, silica or titania-based materials are obtained through the traditional route (**Figure 3.1**) that starts from a solution containing the alkoxide precursor and continues with the following steps:

1. Synthesis of the sol[a] from hydrolysis and partial condensation of alkoxides.
2. Formation of the gel[b] via polycondensation to form metal–oxo–metal or metal–hydroxy–metal bonds.
3. Syneresis or aging, where condensation continues within the gel network, often shrink it and results in solvent expulsion.
4. Drying the gel either in an uncontrolled way to form a dense xerogel or powders via the collapse of the porous network or in a controlled manner to form an aerogel, for example through supercritical drying.
5. Sintering and removal of surface M–OH groups and organic residues through calcination at high temperature (if required).

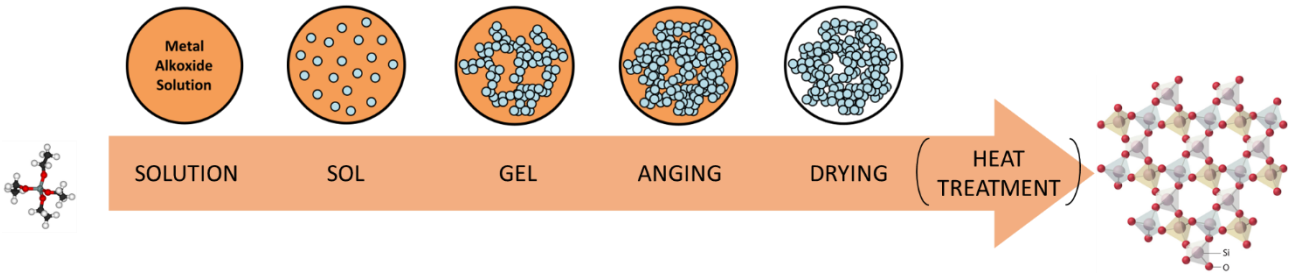

***Figure 3.1**. Schematic representation of traditional sol-gel process steps for silica, starting from TEOS as precursor.*

[a] In a suspension (sol) solid particles are dispersed in a liquid; a colloidal suspension is one in which the size of the particles lies in the colloidal range.[70]

[b] Non-fluid colloidal network or polymer network that is expanded throughout its whole volume by a fluid. Notes: A gel has a finite, usually rather small, yield stress.[71]

The traditional alkoxide route is limited by the number of elements that readily form stable alkoxides and also by the high reactivity of many of these compounds. For this reason, new routes have been adopted that use metal salts as precursors; indeed, hydrolysis and condensation (the latter takes place in two possible ways, olation and oxolation) can also occur between hydrated metal species (**Eqns. 3.1**, **3.2** and **3.3**).[72]

Hydrolysis: $[M(H_2O)_N]^{z+} + hH_2O \leftrightarrow [M(OH)_h(H_2O)_{N-h}]^{(z-h)+} + hH_3O^+$ **(3.1)**

Olation $M - OH + M - H_2O \rightarrow M - OH - M + H_2O$ **(3.2)**

Condensation:

Oxolation $M - OH + M - OH \rightarrow M - O - M + H_2O$ **(3.3)**

One of these routes is the auto-combustion (also known as solution-combustion, SC): a time/energy saving methodology for the preparation of a large variety of inorganic powders that combine the sol-gel with the propellant chemistry that makes it fast, simple, efficient, versatile and provide very high-quality final products with a discrete specific surface area. The SC is based on a fast and self-sustained redox reaction initiated by a source of energy (thermal or electric) between a fuel and an oxidant in the presence of metal cations.[73,74]

Usually, oxidants are metal precursors themselves and the fuel is any organic material capable to chelate the metal ions of interest.

The overall synthesis can be divided into three main steps:

1. Combustion mixture formation.
2. Gel formation.
3. Combustion of the gel.

The final product's morphology is a fluffy sponge-like powder, whose features are strictly related to the chosen synthesis parameters. The main ones are the metal cation precursor, the fuel type, and the reducers-to-oxidizers ratio.

The metal salt precursors can have three types of counter anions groups: reducers, neutrals, or oxidants. Reducers as the case of oxalates, alkoxides, acetates, and acetylacetonates precursors, need additional oxidants to the combustion process regulation, since the net valence of the counter anion is positive. The most common combustion aids are nitric acid (HNO_3) and ammonium nitrate (NH_4NO_3). Neutral precursors are chlorine-based, since the anions do not contribute to the redox reaction during combustion. However, chlorine-based precursors are not desirable for SC due to possible contaminations in the final powder and the release of HCl as a by-product. The oxidants, hydrated nitrates, are preferable not just because of the high oxidizing power (negative charge), but also due to their excellent solubility in water or polar organic solvents and their low decomposition temperature (Td), as observed in **Figure 3.2**,[75] due to the electrostatic interactions between the metal and the nitrate group. For these reasons nitrate precursors are chosen in this project.

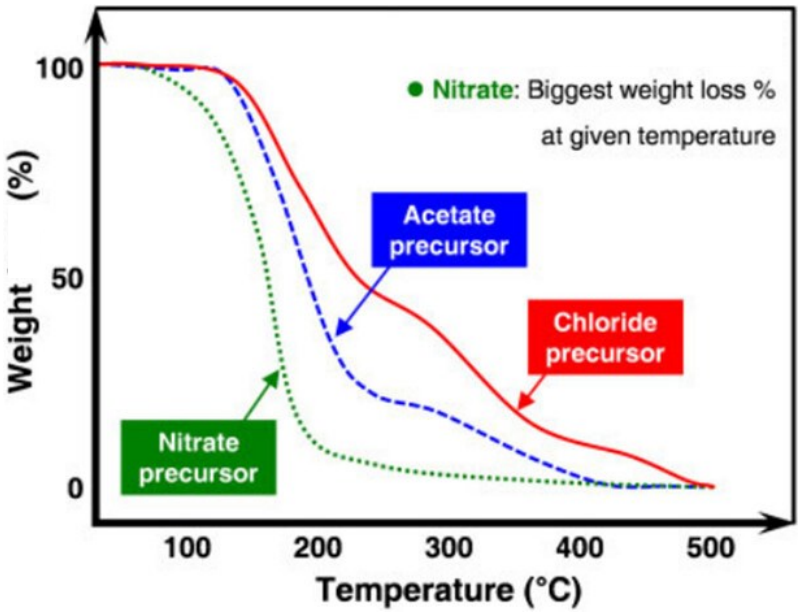

***Figure 3.2**. Thermogravimetric analysis of acetate, chloride and nitrate precursor.*[75]

The fuel plays a double function in SC, acting as a reducer and as chelating agent. It is composed of organic groups, like carboxylic (-COOH) and amino ($-NH_2$), that can react with an oxidant, starting the combustion reaction. During combustion, the oxidants oxidize the fuel to gaseous products, whereas metal cations take the oxygen from the oxidants are converted to oxides. The chelating ability prevents precipitation and maintains the metal cations' homogeneity. During water evaporation, if the fuel is able to form complexes with metal cations, first a sol and then a gel network are easily formed. The role of this network is to maintain the metal cations homogenously fixed in their position and mixed on a molecular scale during the combustion process and to establish a good molecular interaction between the fuel and the oxidant moieties.

Desirable characteristics of an ideal fuel are:[76]

- Soluble in the same solvent of the metal precursors, usually water.
- Low ignition temperature (<500 °C).
- The combustion reaction should be controlled and not lead to explosion.
- Evolution of a large amount of low molecular weight and harmless gasses during combustion.
- Yield no other residual mass except the oxide in question.
- Cheap and readily available or easy to prepare.

The most widely used fuels are citric acid, urea and glycine. Glycine is chosen as the fuel for the synthesis of Ru-doped La-Fe perovskite, because the glycine molecule has a carboxylic acid group at one end and an amine group at the other end, both of which can chelate the metal ions, despite citric acid or urea that have respectively only one of the two groups. This zwitterionic character (with more than one functional group containing at least one positive and one negative charge, being the molecule electrically neutral) allows effective complexation with metal cations of varying ionic size. The carboxylic acid group most effectively coordinates alkali and alkaline-earth cations, while many transition metals are most effectively complexed by the amine group (**Figure 3.3**),[77] so this complex agent is suitable for the La, Fe, and Ru cations in the combustion mixture.

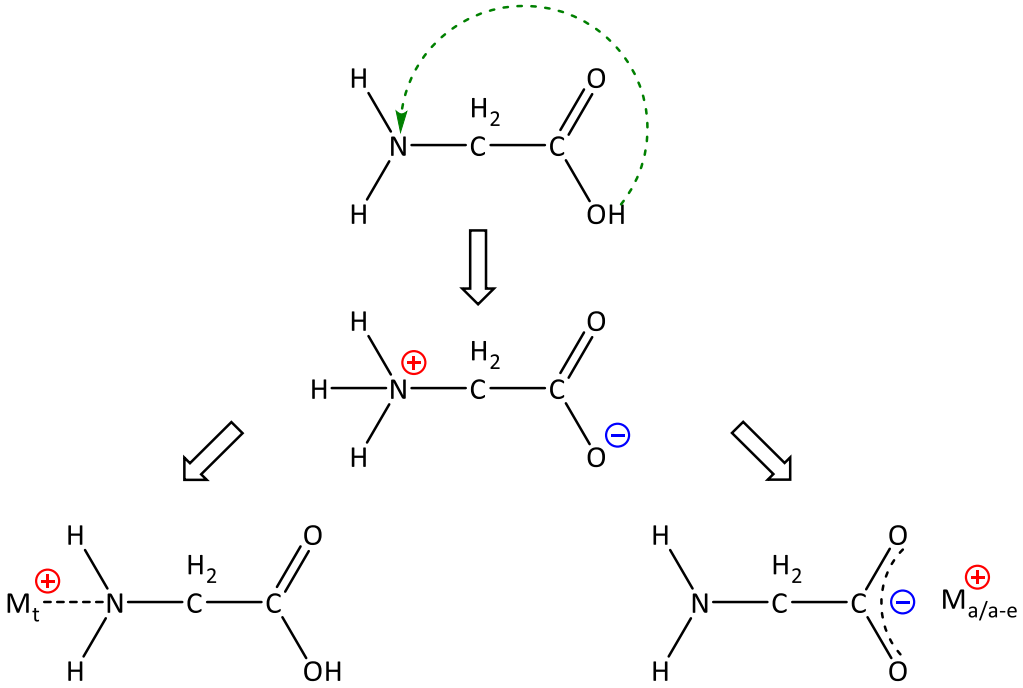

***Figure 3.3**. Schematic representation of chemical structure of glycine, its zwitterionic form and the general complex that form with metal cations, especially with transition (M_t) and alkali/alkali-earth metals ($M_{a/a-e}$).*

The last important parameter is the molar ratio between reducers and oxidants. In fuel-rich conditions the probability of finding impurities (carbon and carbonates) in the final product is higher due to the larger quantity of fuel. The stoichiometric condition grants a self-combustion reaction and auto-ignition process with a highly exothermic behavior reaching high temperatures through a uniform distribution. Thus, when a stoichiometric combustion occurs, an optimal amount of oxygen and fuel mix generates the highest heat possible, and the maximum combustion efficiency is reached. The stoichiometric ratio would be optimal for the final characteristic of the perovskite, but it is not chosen for environmental reasons. The combustion can be complete or incomplete and lead to two different products of complete and incomplete combustion (PCC and PIC respectively), presented in **Eqns. 3.4** and **3.5**.

Complete combustion Products of Complete Combustion (**PCC**)

$$xM^{n+} + yNO_3^{-1} + zNH_2CH_2COOH \rightarrow \overbrace{aM_aO_b + bH_2O + cCO_2 + dN_2} \quad \textbf{(3.4)}$$

Incomplete combustion Products of Incomplete Combustion (**PIC**)

$$xM^{n+} + yNO_3^{-1} + zNH_2CH_2COOH \rightarrow \overbrace{aM_aO_b + bH_2O + cCO_2 + dN_2 + eNO_2 + fNO + gCO + hC} \quad \textbf{(3.5)}$$

The incomplete reaction presents the additional formation of NO_x and CO by-products, which are well known to be environmentally harmful. They are toxic and smog-forming chemicals, and their emissions are strictly regulated. Commonly PIC are kinetically and thermically favorable when the duration of exposure is short and at high temperature, respectively. On account of this, a fuel deficient condition (glycine/nitrate, G/N, ratio of 1:3) is chosen, in this regime: as a consequences the total amount of by-products is lower, having less reactants but also the moles of escaped gases to moles of perovskite ratio is lower.[78]

It was also proven that CO is present in lower amount using lower glycine to nitrate molar ratios (**Figure 3.4**).[79] Furthermore, the combustion is slower than in other regime and the flame does not reach the stoichiometric regime's very high temperature. In addition, there are less carbonaceous residues. A lower glycine to nitrate molar ratio than that used in this work can negatively compromise the complexation with the metals and can give flameless smoldered reaction resulting in large evolution of gases, many of which are NO_x, this condition is called extremely fuel deficient combustion and it is performed when the thermal stability of the product is low.

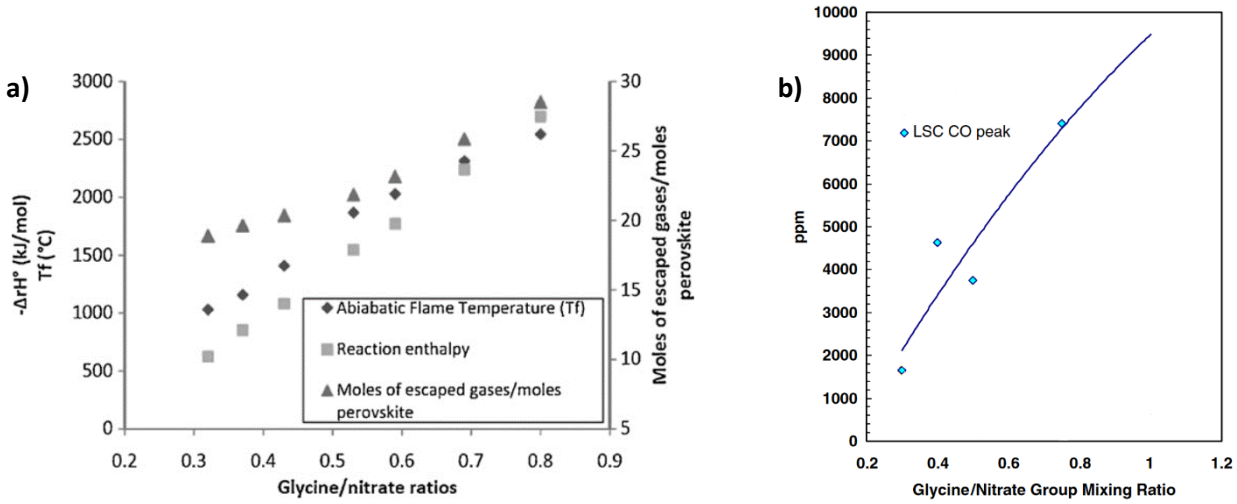

Figure 3.4. a) *Thermodynamic characteristic of the combustion reaction as function of glycine to nitrate ratios,[78] and* ***b)*** *peak carbon monoxide concentrations in self-combustion synthesis of La-based perovskite.[79]*

The combustion reaction is very fast, and the flame does not reach a very high temperature due to the low amount of fuel, giving a product with low-crystallinity, **Figure 3.5.** The as-burned powder is raw, presenting the typical reflections of perovskites, especially the reflection of (121) is well evident, but the material is not well crystallized. An additional heat treatment in air is needed to obtain a single crystalline phase; more in detail, the diffraction pattern matches with an orthorhombic crystal system (space group N° 62, Pnma, see **Figure 3.5**). No other phases, especially ruthenium oxide, are detectable. This fact could indicate that Ru is successfully doped into the $LaFeO_3$ lattice as $LaFe_{0.9}Ru_{0.1}O_3$.

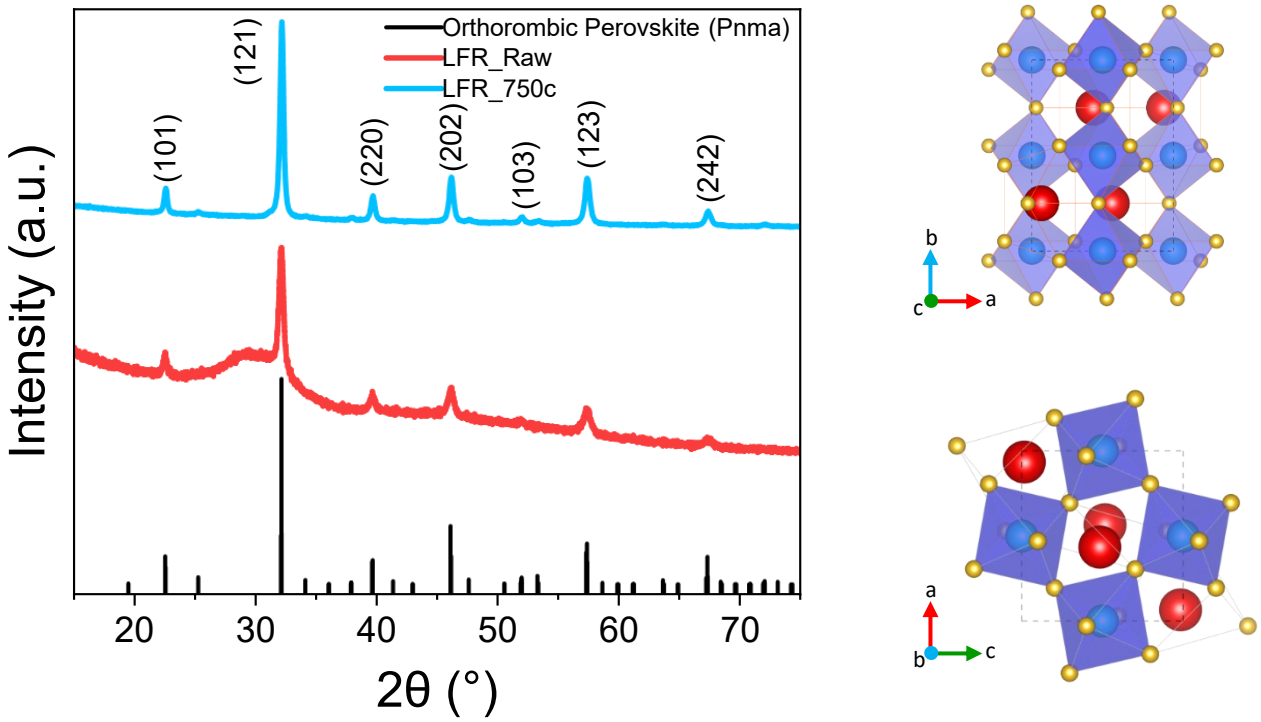

Figure 3.5. *On the left, XRD diffractogram of raw LFR, LFR calcinated at 750 °C and the orthorhombic perovskite reference (ICSD: 98-023-6154). On the right, an orthorhombic perovskite ABO_3 is presented from two different point of view, A-cations in red, B-cations in blue, and oxygen in yellow.*

The criteria of the synthesis are chosen based on general trends regarding lanthanum-based perovskites-like materials through the survey of scientific literature. In summary, pure single-phase Ru-doped La-Fe perovskite-type oxide is prepared using an aqueous solution of metal nitrates as precursors, due the low decomposition temperature and avoiding contamination. Glycine is used as fuel due to its capability of complex efficiently the metal cations, with a G/N ratio of 1:3 to reduce the PIC amount and a calcination step is needed to achieve the crystalline structure without impurities; a scheme is present in **Figure 3.6**. Two different types of La-Fe perovskite-like with a Ru-doping in B site equal to 10% (in atomic fraction) are obtained. One is stoichiometric (A/B=1) $LaFe_{0.9}Ru_{0.1}O_3$ (*LFR_750c*) and one is non-stoichiometric (A/B<1) with a deficit of the A cation $La_{0.9}Fe_{0.9}Ru_{0.1}O_3$ (*L0.9FR_750c*).

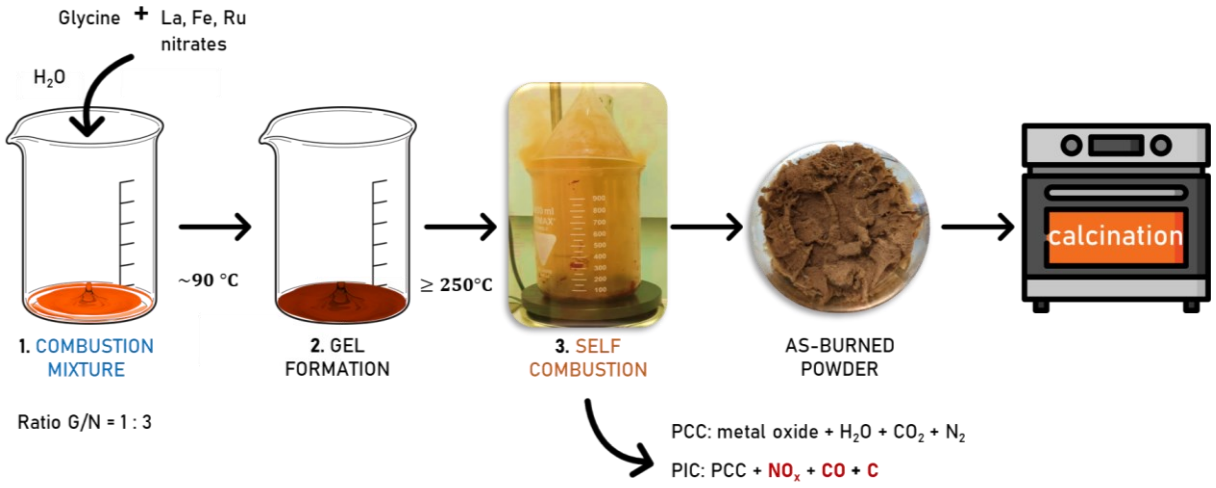

Figure 3.6. *Schematic diagram illustrating the different steps involved in Ru-doped La-Fe perovskite-like self-combustion synthesis.*

The calcination is performed at 750 °C, a common temperature retrieved in literature that allows to achieve crystallization and removal of all the contamination in particular carbonaceous residues. Actually, successive thermogravimetric analysis combined with mass spectrometry proves that a lower temperature could be also effective, as shown in **Figure 3.7**.

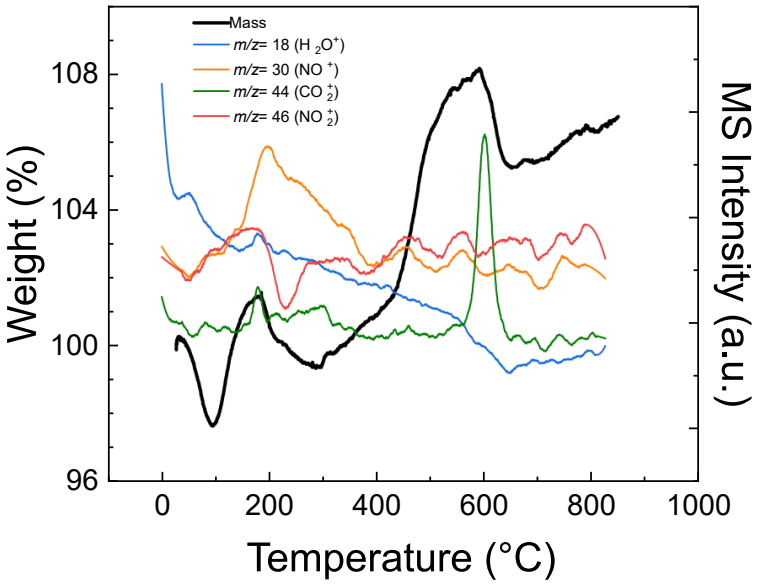

Figure 3.7. *TGA and MS curves of raw LFR, performed in synthetic air (80% N_2, 20% O_2, in volumetric fraction).*

A first weight drop can be noticed in the TGA curve at ca. 100 °C due to the release of physisorbed water after which there is an increase of the weight, probably due to the inclusion of oxygen in the reticular positions to form the crystalline structure and the storage of oxygen in the interstitial sites of the lattice; this rise seems to be present during the whole analysis and increase the weight over the initial value. A second drop of mass occurs around 200 °C to 300 °C accompanied by an increase in the M/Z 30. It is related to the thermal decomposition of the remaining nitrates that do not react throughout the time of combustion, so the nitrates do not participate in the redox reaction and do not decompose with the energy supplied by the flames. A last drop occurs at roughly 600 °C caused by the release of the carbonaceous material, left in turn by the glycine. A lower temperature between 600-650 °C can yield a pure final product in a single crystalline phase, as shown in the XRD pattern of LFR calcinated at 600 °C in **Figure S1**.

A fluffy powder is obtained at the end of the synthesis, and SEM images (**Figure 3.8**) show a sponge-like morphology.

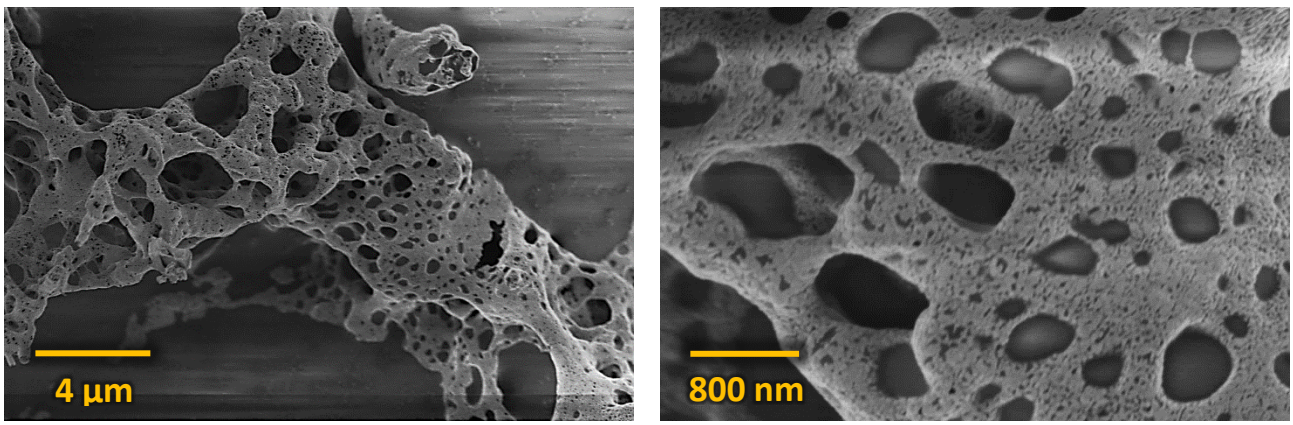

Figure 3.8. *SEM images of LFR_750c that presents a sponge-like morphology typical of the SC.*

Heat Treatments

After the synthesis of *LFR_750c* and *L0.9FR_750c*, further heat treatments are carried out to follow the exsolution process for further application as catalyst for oxygen evolution reaction (OER). The diagram below (**Figure 3.9**) shows all the thermal treatments performed in this work. The samples' characterization results are described in the following chapter.

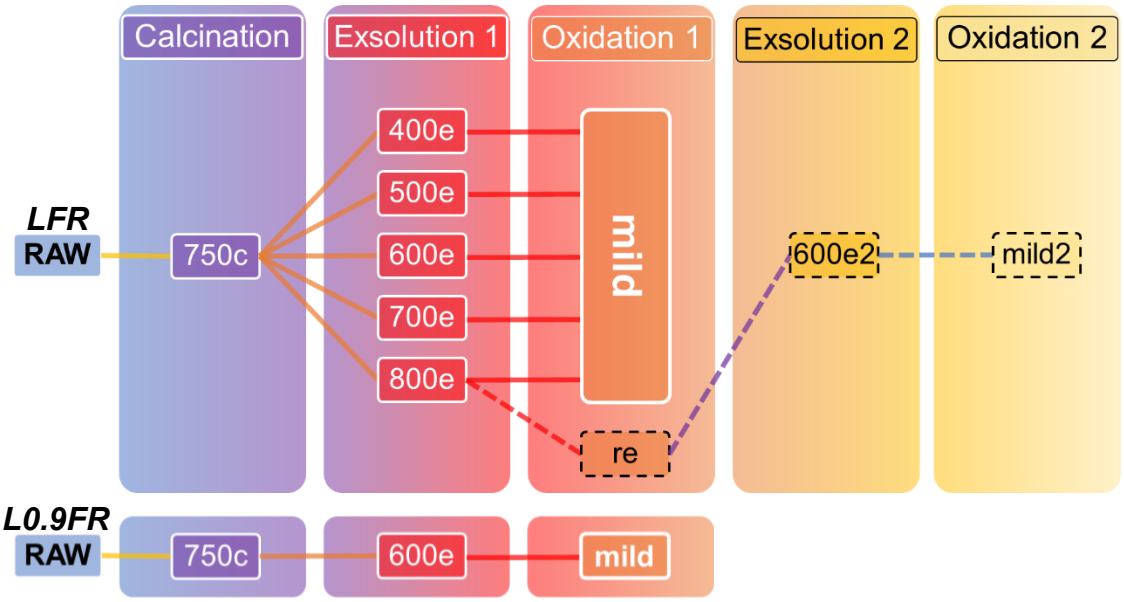

Figure 3.9. *Diagram of the treatment steps for LFR and L0.9FR. All treatments are performed with a heating rate of 5 °C min^{-1} with a 3-hour isotherm at the desired temperature.*

The samples are labelled and abbreviated according to **Table 3.1**.

Sample	***Name***	***Abbreviation***
$LaFe_{09}Ru_{0.1}O_3$ as-burned powder, not well crystallized	*LFR_raw*	*/*
LFR_raw after the calcination at 750 °C	*LFR_750c*	*750c*
LFR_750c after the exsolution at X00 °C	*LFR_750c_X00e*	*X00e*
LFR_750c_X00e after the mild oxidation at 400 °C	*LFR_750c_X00e_400m*	*X00m*
LFR_750c_X00e after the high oxidation at 750 °C	*LFR_750c_X00e_750h*	*750h*
LFR_750c_X00e_750h after a second exsolution at 600 °C	*LFR_750c_X00e_750h_600e2*	*600e2*
LFR_750c_X00e_750h_600e2 after the mild oxidation at 400 °C	*LFR_750c_X00e_750h_600e2_400m2*	*600m2*
X represent an integer between 4 and 8 inclusive		
The labelling of $La_{0.9}Fe_{09}Ru_{0.1}O_3$-based samples are analogous to the LFR-based ones, but the first part of the samples name is "*L0.9FR*" instead of "*LFR*" and the abbreviations have suffix "*0.9_*"		

Table 3.1*. Labelling of the samples studied in this work.*

After the calcination, treatment at different temperatures in a reductive atmosphere (96% Ar, 4% H_2, in volumetric fraction) is realized for the stoichiometric sample. Among the exsolved samples, the one prepared at 600 °C presents the lower overpotential at 5 mA cm^{-2} (η_5) for OER, as is described in the next chapter. During the exsolution step, the ruthenium atoms are reduced and driven to the surface where nucleate and grown to form nanoparticles, but Ru is not the only element that emerges; lanthanum can also do that, especially at high temperatures, but this negatively affects the catalytic activity for OER. To clean the surface from the La oxide, a mild oxidation at 400 °C in air is needed, which however causes the oxidation and partial re-incorporation of Ru in the parent oxide.
An alternative approach different than the mild oxidation is implemented starting from the sample exsolved at 800 °C. the underlying idea is to make a catalyst that can be regenerated. This sample has the highest quantity of exsolved ruthenium precisely because the process was carried out at higher temperatures, but also the one in which we expect a thicker layer of lanthanum oxide, which passivates or isolates the ruthenium nanoparticles. Instead of making a mild oxidation, an oxidation at 750 °C is made in which all the segregated and emerged material is re-incorporated in the matrix, thus returning to a condition like the initial calcined sample. Still, a substantial difference is expected: an enrichment of the noble metal towards the near-surface of the perovskite. Starting from this perovskite enriched in ruthenium on the surface, a second exsolution is carried out at 600°C (the temperature at which the best performances are obtained in the first exsolution), and a second mild oxidation. However, this group of regenerated samples shows worse performance.
For the calcined non-stoichiometric sample only the exsolution at 600 °C and the mild oxidation are performed. This set of experiments is performed to investigate whether the A ion deficit affects the process.

More details and explanations are present in the following chapter.

The treatments do not affect the type of morphology that remains a sponge-like structure (**Figure S2**). The first noticeable effect of the exsolution is the formation of nanoparticles on the surface, as seen in **Figure 3.10**, in high-resolution scanning electron microscopy. In the SEM micrographs, the NPs are well distinguished from the matrix, both after the exsolution at 800 °C and its mild oxidation, and it seems that there are no differences in dimension; in the two samples, the average diameter is around 20 nm.

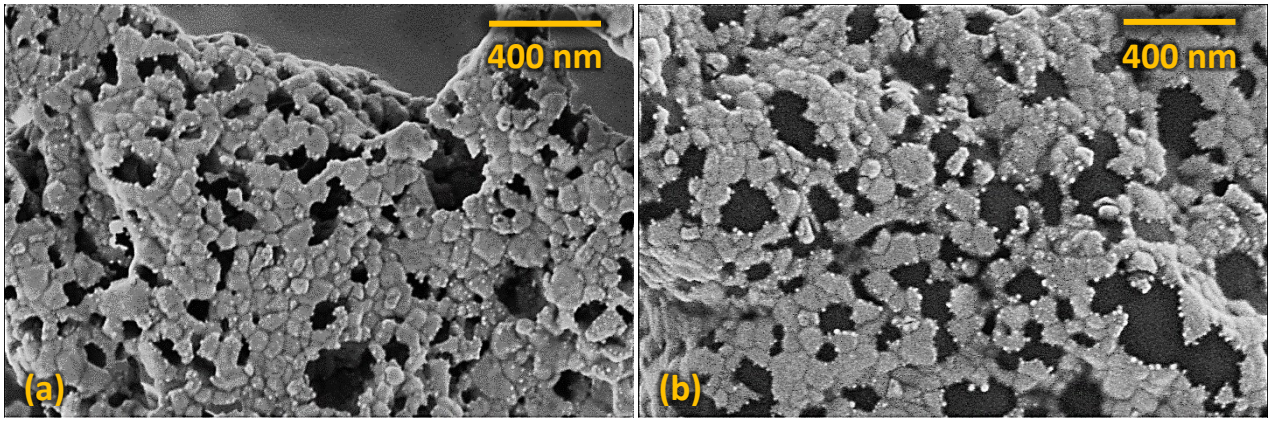

Figure 3.10. *SEM images of LFR_750c_800e* ***(a)*** *and LFR_750c_800e_400m* ***(b)****, the little bright dots are the nanoparticles. Inside the brackets the standard deviations are reported.*

The NPs are not seen in the samples exsolved at 600 °C and below because the NPs are too small to be detected by the SEM, but their existence is proved by TEM image at least for the sample exsolved at 600 °C (**Figure S3**). Unfortunately, it was impossible to analyze the chemical composition of the single nanoparticle. Still, since both the perovskite and the exsolution process are well-known and studied in the literature, it is reasonable to assume that these nanoparticles are composed of ruthenium.

Other effects of the heat treatments concern the porosity and the crystal structure. The physisorption analysis of the powder pre- and post-treatment of exsolution and mild oxidation is presented in **Figure 3.11**. According to the IUPAC classification, the samples show type IV isotherms, and exhibit hysteresis loop proper of a mesoporous material.[80,81] The calcined sample presents a specific BET surface area of 13 $m^2 g^{-1}$, slightly lower than that reported in the literature for a SC synthesis with glycine,[78] probably due to the fuel deficit, which leads to less gasses evolution and requires the additional calcination step. Unsurprisingly, the post-treatments favor sintering, closing and collapsing of the pores, resulting in a slight decrease in the specific surface area and the pore volume. However, the pore mode remains unchanged at 5 nm. The adsorption is performed with N_2 so there is no information about microporosity, but since the pore distributions start from the near zero it is probably that porosity under 2 nm is not significative.

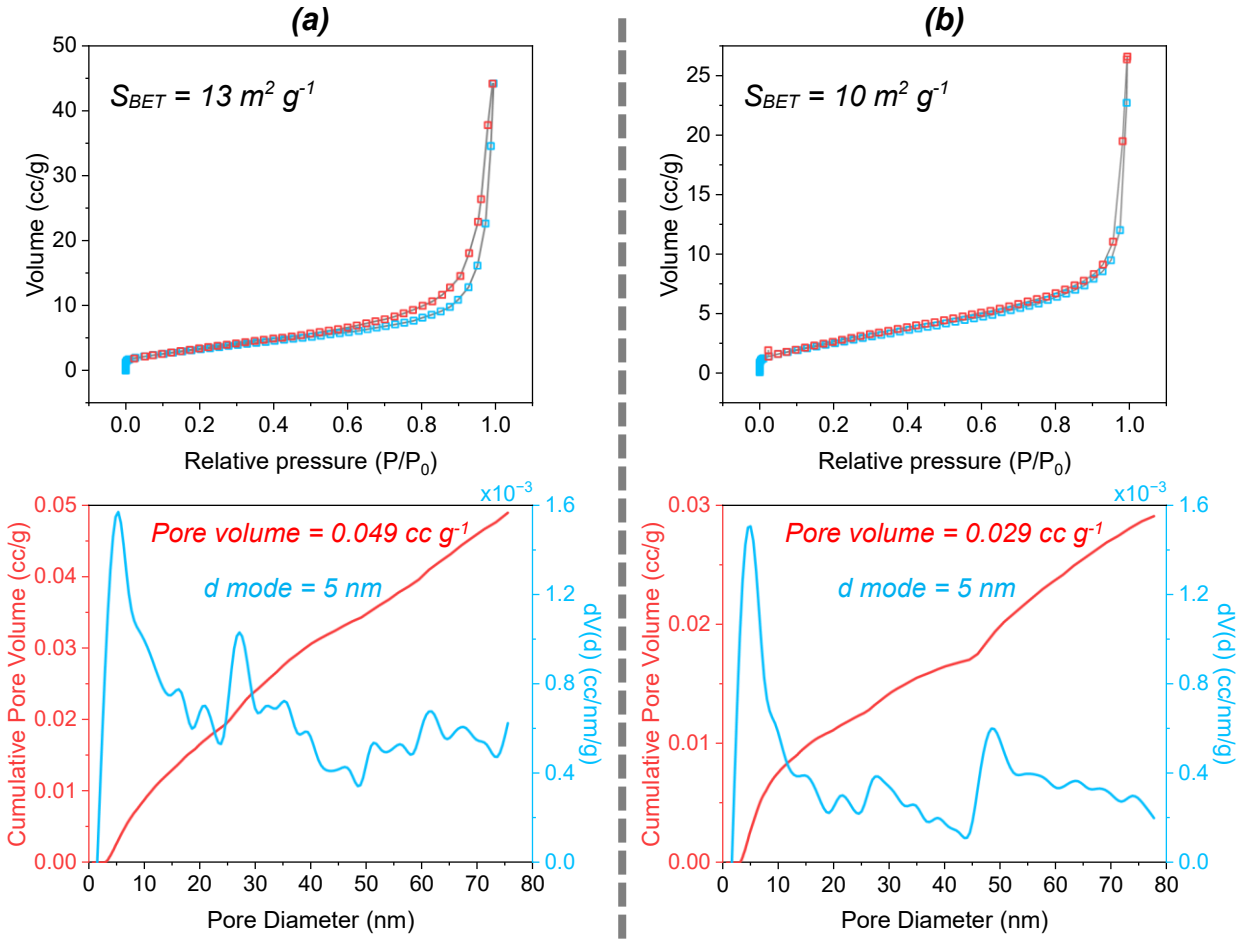

Figure 3.11. *N_2 physisorption isotherms (top) and relative pore size distribution calculated by the adsorption branch by applying the NLDFR kernel (bottom) for LFR calcinated **(a)** and mild oxidated after the exsolution at 800 °C **(b)**.*

After the heat treatments, the main crystalline phase remains the orthorhombic perovskite in both stoichiometric and non-stoichiometric samples. Still, new small reflections appear, identified only through the Rietveld refinement (**Figure 3.12**) and belonging to the lanthanum oxide and hydroxide. Another change concerns the main diffraction peak (121) which is slightly shifted to smaller angles, suggesting an enlargement of the primitive cell due to the presence of vacancies left by the migration of Ru and the partial reduction of the iron atoms that pass from an oxidation state *+3* to *+2*, thus increasing the size (ionic radio of Fe^{3+} is 0.645 Å, while the one of Fe^{2+} is 0.78 Å). Metallic ruthenium is not present, and a possible explanation could be that its amount in a crystalline phase is too low to be detected by XRD.

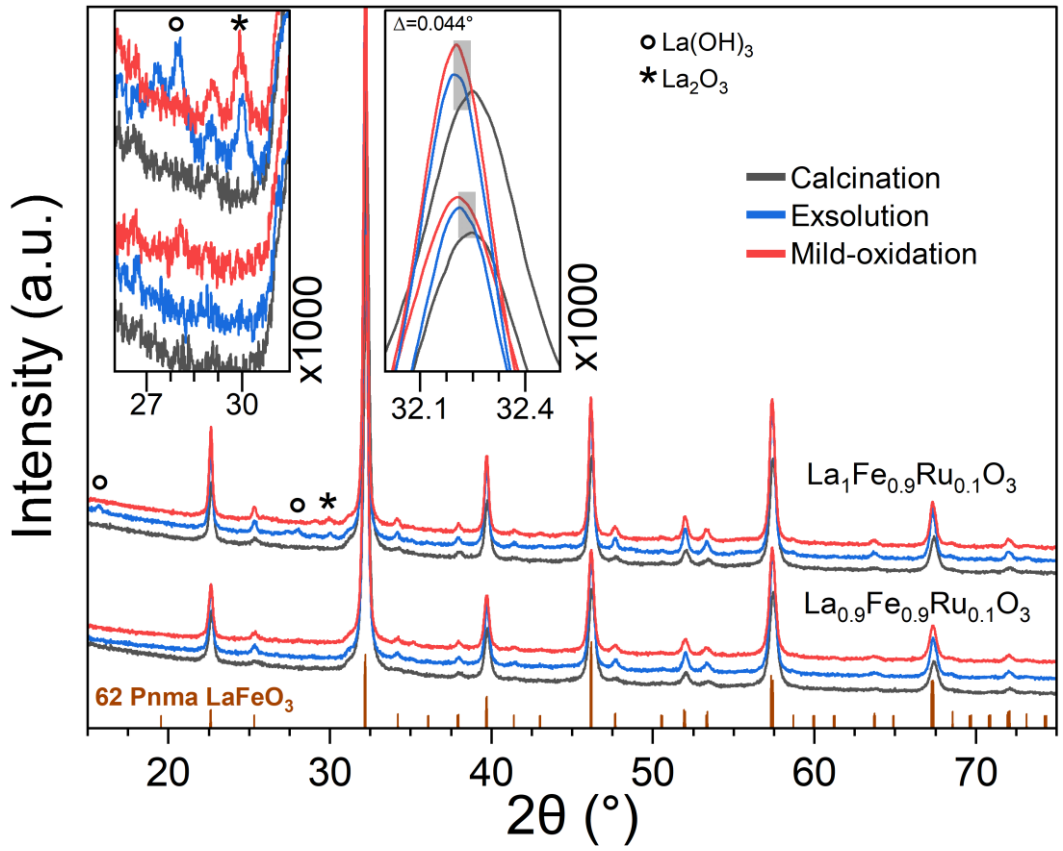

Figure 3.12. *XRD diffractogram of LFR calcinated, exsolved at 800 °C, mild oxidated, and of L0.9FR calcinated, exsolved at 600 °C, mild oxidated.*

Another predictable effect is the increasing crystallite size with the increasing of temperature and steps as shown in **Table 3.2**. The crystallite sizes are estimated by applying the Scherrer **Eqn. 3.6** at the main signal around 32 ° which is composed by many reflections. The most intense reflection is the (121) at 2θ value of 32.2 °, while the other diffraction peaks have a lower intensity than the (121); therefore, considering the entire main signal as (121) reflection is a good approximation, resulting in a slightly overestimation of the crystallite size.

Scherrer equation: $$L = \frac{K\,\lambda}{\beta_{hkl}\cos\theta} \qquad \textbf{(3.6)}$$

L : crystallite size – in nm
K : lattice constant - in most cases as 0.9
λ : wavelength – here is the Cu-K_α one (0.154 nm)
βhkl : full width at half maximum (FWHM) of the intensity of the reflection - in radians
θ : half of the Bragg angle 2θ - in radians

LFR (nm)

750c					
25					
400e	***500e***	***600e***	***700e***	***800e***	
26	27	28	33	34	
				mild ox	***high ox***
				36	38
					600e2
					39
					mild ox 2
					40

L0.9FR (nm)

750c
26
600e
29
mild ox
30

Table 3.2. *Crystallite size dimensions, calculated with Scherrer equation using the FWHM of the main signal of the diffractogram, that is a good approximation of the (121) reflection.*

Chapter 4

Results and discussion

Initial considerations

This chapter describes the study of the surface's oxide characterization through different techniques such XPS and electrocatalytic analysis during OER (LSV, EIS and CV). It is also study through the same techniques the surface reconstruction after different thermal treatments, such as exsolution and oxidation at low and high temperature. The study is made of three parts:

- LFR which underwent the first exsolution and mild oxidation treatments.
- "Regenerated" LFR: starting from LFR exsolved at 800 °C, high oxidation is carried out, so exsolution and mild oxidation steps are repeated.
- L0.9FR which underwent exsolution at 600 °C and mild oxidation.
- Electrochemical active surface area analysis.

To carry out electrochemical analyses, it is necessary to prepare an ink, i.e. a suspension containing the sample to be analyzed. To increase the conductivity of the perovskite powder, carbon black (CB) is added: they are grinded together and suspended in isopropanol with Nafion as binder (ionomer), put in an ultrasonic bath (for 10 min) and subsequently the deposition is carried out via drop casting onto a glassy carbon electrode; a scheme is presented in **Figure 4.1**.

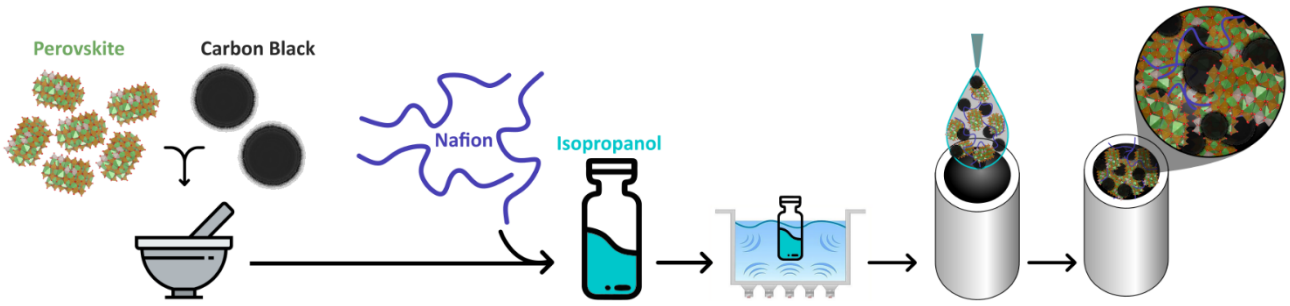

Figure 4.1. *Schematic illustration of the preparation of the ink and of the drop casting on the glassy carbon electrode.*

The deposited powder is composed of perovskite regions partially covered and dispersed in carbon black as can be seen in SEM image (**Figure 4.2**).

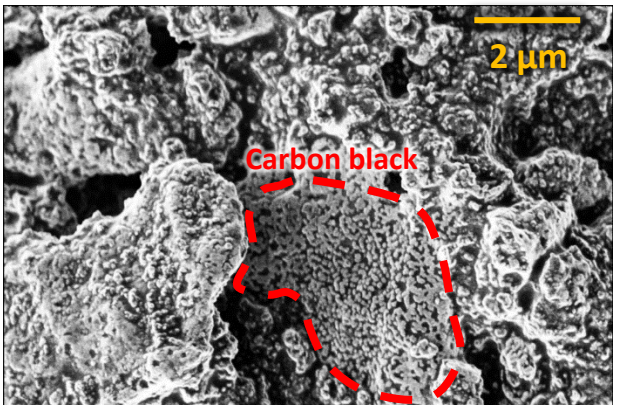

Figure 4.2. *SEM image of perovskite-CB deposited powder.*

The main methodology adopted to analyze and compare the activity towards the OER of different samples is the linear sweep voltammetry (LSV). In the discussion, LSVs data are presented without iR-correction, therefore the results obtained have slightly overestimated voltages and therefore the overpotential (η). The overvoltage in literature is commonly reported at a current density of 10 mA cm^{-2}, however in this study a lower value, 5 mA cm^{-2}, was chosen for the comparison because not all the current densities of the samples reached 10 mA cm^{-2} in the scanning range (1 V - 1.9 V vs RHE) and increasing the voltage led to excessive bubble formation which compromised the measurement. Nevertheless, a current density of 5 mA cm^{-2} instead of 10 mA cm^{-2} is also more desirable since ensures a kinetic control avoiding diffusional process.

XPS is used to follow the modification of the surface's chemical composition (elemental identification and their relative abundances (expressed in atomic percentages) on the surface) and the oxidation state of ruthenium atoms on the surface, during all the treatments. The three investigated regions are presented in **Figure 4.3**, in particular the region between 276 eV and 294 eV is used to investigated Ru 3d; however, signals of the adventitious carbon (C 1s) appear also in this region, thus complicating the deconvolution and the quantification analysis. The deconvolution is only made for ruthenium spectra (**Figure 4.3a**) while for lanthanum and iron spectra (**Figure 4.3b**,**c**) are used only to estimate the total intensity of the signals for the relative atomic quantification on the surface.

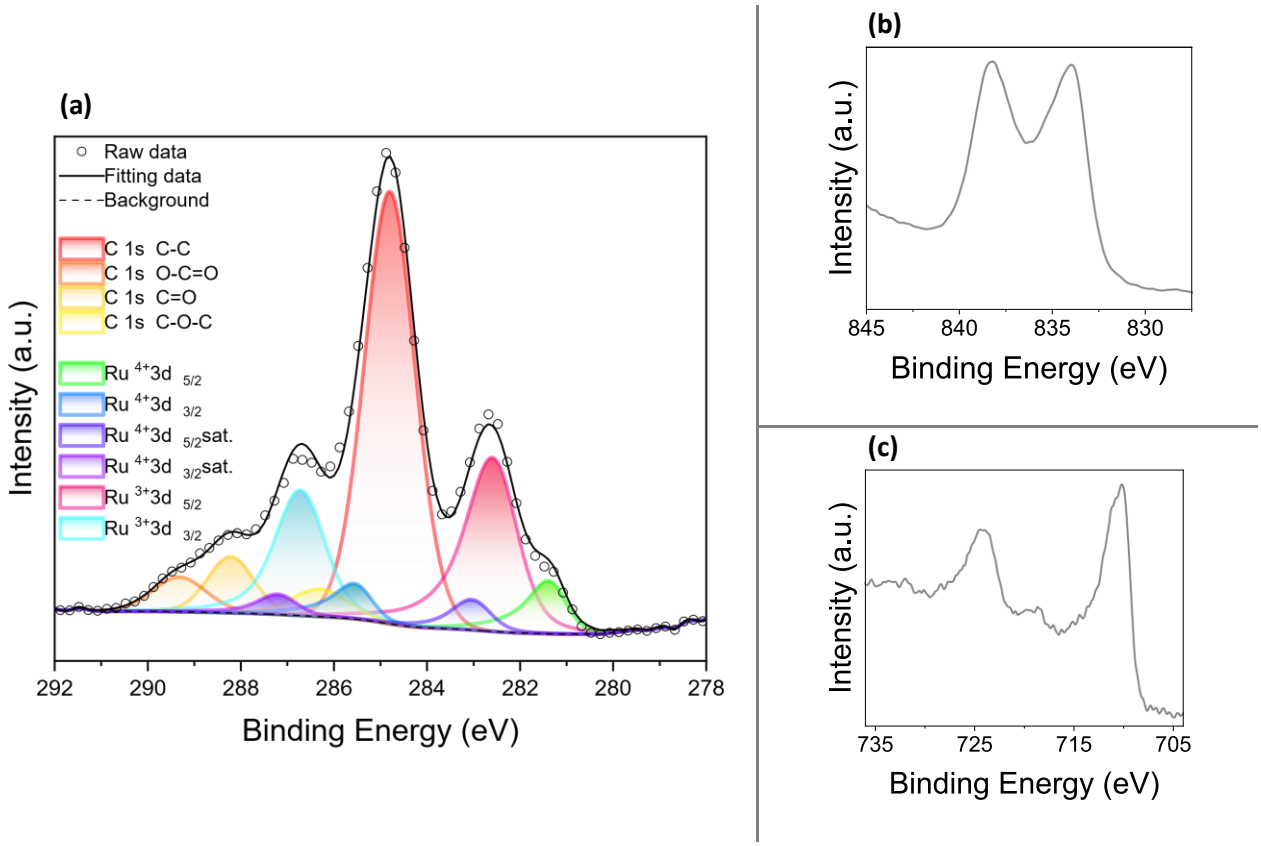

*Figure 4.3. XPS spectra of LFR_750: **(a)** Ruthenium (Ru 3d) and Carbon (C 1s) spectra and their deconvolution, **(b)** Lanthanum (La $3d_{5/2}$) and **(c)** Iron (Fe 2p) spectra on the top and bottom right respectively.*

As can be seen in **Figure 4.3a**, mainly four adventitious carbon signals can be identified which overlap with the ruthenium signals. In the following discussion, for an easier and more immediate visualization of the data, the carbon signals will not be shown but only the ruthenium deconvolution peaks, grouped in different colors for each oxidation state. The complete XPS data and deconvolutions for the Ru 3d are reported in **Figure S4-19**. There are three signals of ruthenium for each electronic state (oxidation state) and represent the noble metal in different chemical environments. Ru^{3+} is related to the ruthenium incorporated into the perovskite-like lattice, indeed Ru substitutes the iron and to maintain the electroneutrality it assumes the oxidation state 3+ (so it is not different form the Ru in the perovskite bulk). Ru^0 appears during the exsolution when H_2 reacts with O^{2-} in the lattice and transfers the electrons to the more oxophilic atom, Ru in this case. These reduced metallic Ru atoms migrate to the surface to form NPs. Finally, the signal located at around 281.2 eV could be ascribed to atoms surrounded by two different types of chemical environments: the one related to oxide RuO_2 and the other one related to ruthenium atoms located into the perovskite-type structure accompanied by oxygen vacancies, therefore shifting the binding energy to lower values compared to those ones fully coordinated. The latter type of atoms includes the atoms proven to be exsolved (via the 4% v/v H_2/Ar treatment) and re-incorporated in the parent oxide (via an oxidative treatment), in both case the atoms of ruthenium are not fully coordinated by the other atoms of perovskite and for this reason their chemical environment is different with respect to that of atoms fully coordinated into the perovskite-like (~ 283 eV). It is not possible to distinguish the different contributions for the Ru^{4+}, but it is reasonable to think that the partially coordinated ruthenium species is significantly present compared to the ruthenium oxide in cases where the Ru exsolved on the surface is not much, therefore in the pre-treatment cases and in samples from low temperatures of exsolution.

Exsolution and mild oxidation of $La_1Fe_{0.9}Ru_{0.1}O_3$ - LFR

During the exsolution, ruthenium atoms from the lattice of the perovskite migrate to the surface where they are reduced by a redox reaction with H_2. Increasing the temperature and time, a larger amount of ruthenium can reach the surface thanks to the diffusion (**Figure 4.4**).

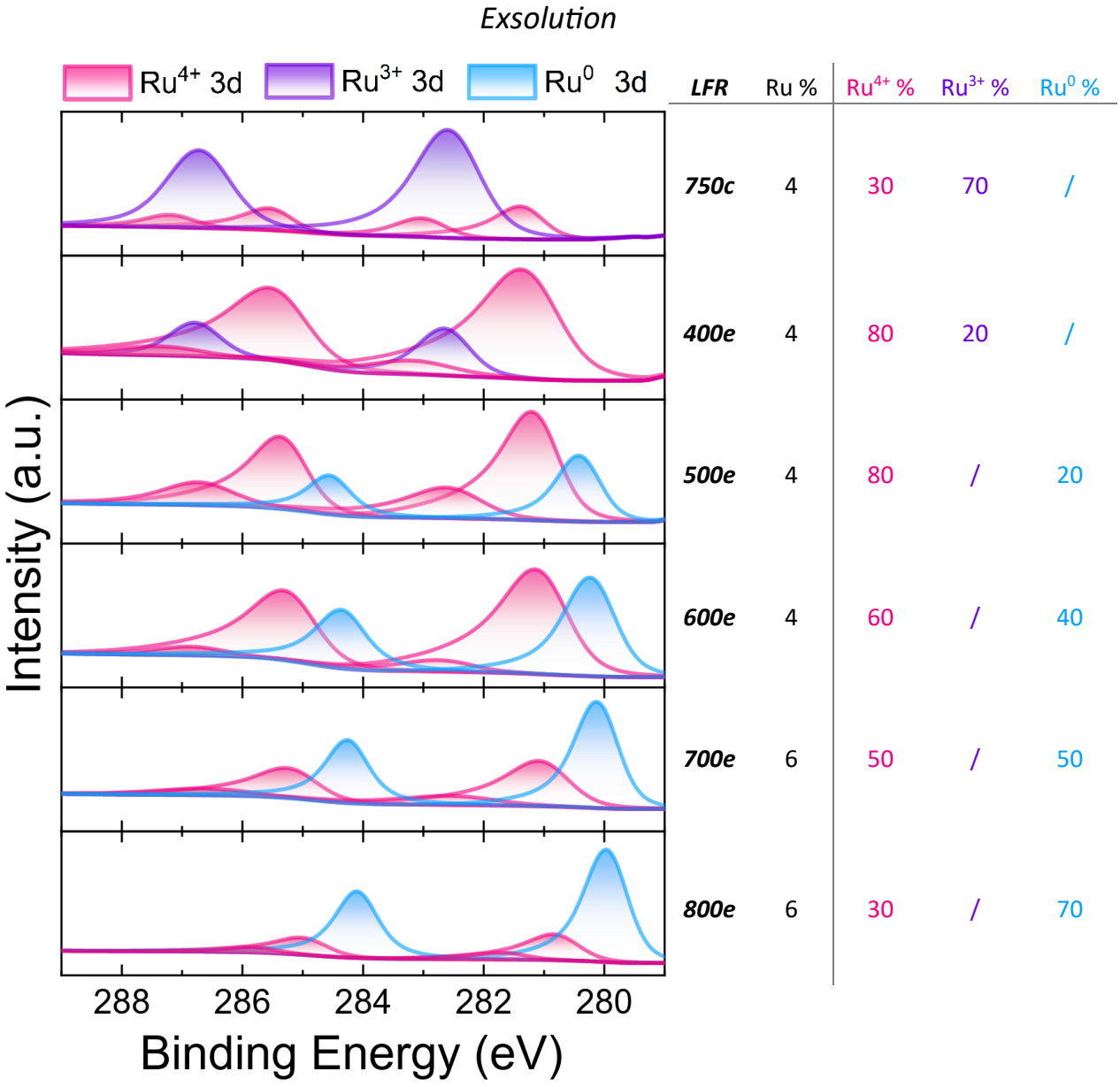

LFR	Ru %	Ru^{4+} %	Ru^{3+} %	Ru^0 %
750c	4	30	70	/
400e	4	80	20	/
500e	4	80	/	20
600e	4	60	/	40
700e	6	50	/	50
800e	6	30	/	70

Figure 4.4. *Ru 3d deconvoluted peaks from XPS spectra of LFR_750c and LFR_750c_X00e (left), atomic percentage in weight of Ru with respect to the total metals of the perovskite-type and the percentages of its oxidation state (right).*

The theoretical quantity of ruthenium with respect to the overall metals in the perovskite is 5% (mass fraction) and the value of the sample before exsolution (*LFR_750c*) is very similar. After exsolution, an increase of Ru content on the surface is expected but it remains roughly constant because, while the exsolved ruthenium reaches the surface of the parent oxide, the XPS detects the overall surface of the system formed by parent oxide and exsolved Ru. XPS is a surface technique that typically manages to investigate up to 5 nm in depth, and when the exsolution occurs the ruthenium already present in a uniform manner on the surface will concentrate in specific points where the nanoparticle will grow. When these are formed, they protrude from the matrix, thus increasing the roughness of the system. In particles with a smaller diameter than the detection depth, all the ruthenium present in the NPs is detected but shadow areas are generated under the NPs which are not detected with respect to the case of a flat surface in the calcined sample. In these shadow areas the ruthenium in the matrix is not detected, Ru atoms may already be present pre exsolution or arrive by diffusion from the bulk of the perovskite. In particles with a diameter larger than the detection depth, part of the ruthenium of the NPs is not detected due to the limitations of the technique (**Figure 4.5**). Due to this effect, the measured quantity of ruthenium remains almost constant and only when the dimensions of the NPs become considerable, up to covering a large part of the surface, the measured Ru content increases (all these considerations are valid also for the following XPS spectra).

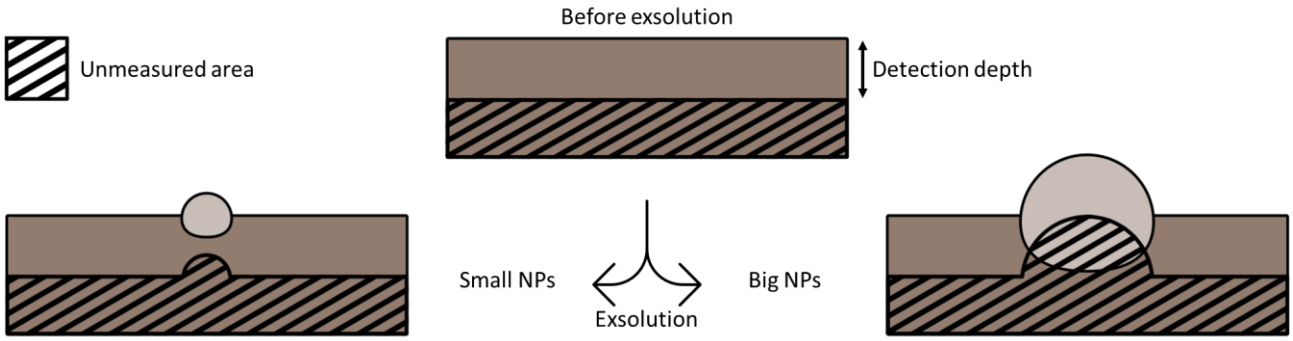

Figure 4.5. *Representation of the samples XPS measurement in the case of pre-exsolution (top centre), of nanoparticle smaller and bigger than the scanning depth (bottom left and bottom right respectively).*

However, the effect of the temperature on the exsolution process is appreciable considering the relative percentages of ruthenium for the various oxidation states (0, +3, +4). In addition, increasing the temperature, Ru^{3+} disappears and the metallic one increases. When removed from the oven used for the exsolution, the samples are exposed to the air and therefore the ruthenium in contact with atmospheric oxygen is oxidized. At the same time, the one present in the bulk of the nanoparticle remains metallic. It can be seen that the sample exsolved at 400 °C does not present metallic ruthenium because, rather than nanoparticles, small clusters are formed which are entirely oxidized to Ru^{4+} in air (there is also Ru^{3+} evidently because not all the ruthenium in the near-surface has been able to diffuse and increase the nanoparticles). In contrast, for the samples at higher exsolution temperatures, there is an increase of metallic ruthenium (NPs bulk) with respect to RuO_2 (NPs surface, considering the quantity of Ru partially coordinated not significant. Therefore, it is assumed that the dimensions increase.

So, increasing the temperature, the quantity of exsolved Ru increases and better electrochemical performances are expected, but not at high temperature, as seen in **Figure 4.6**.

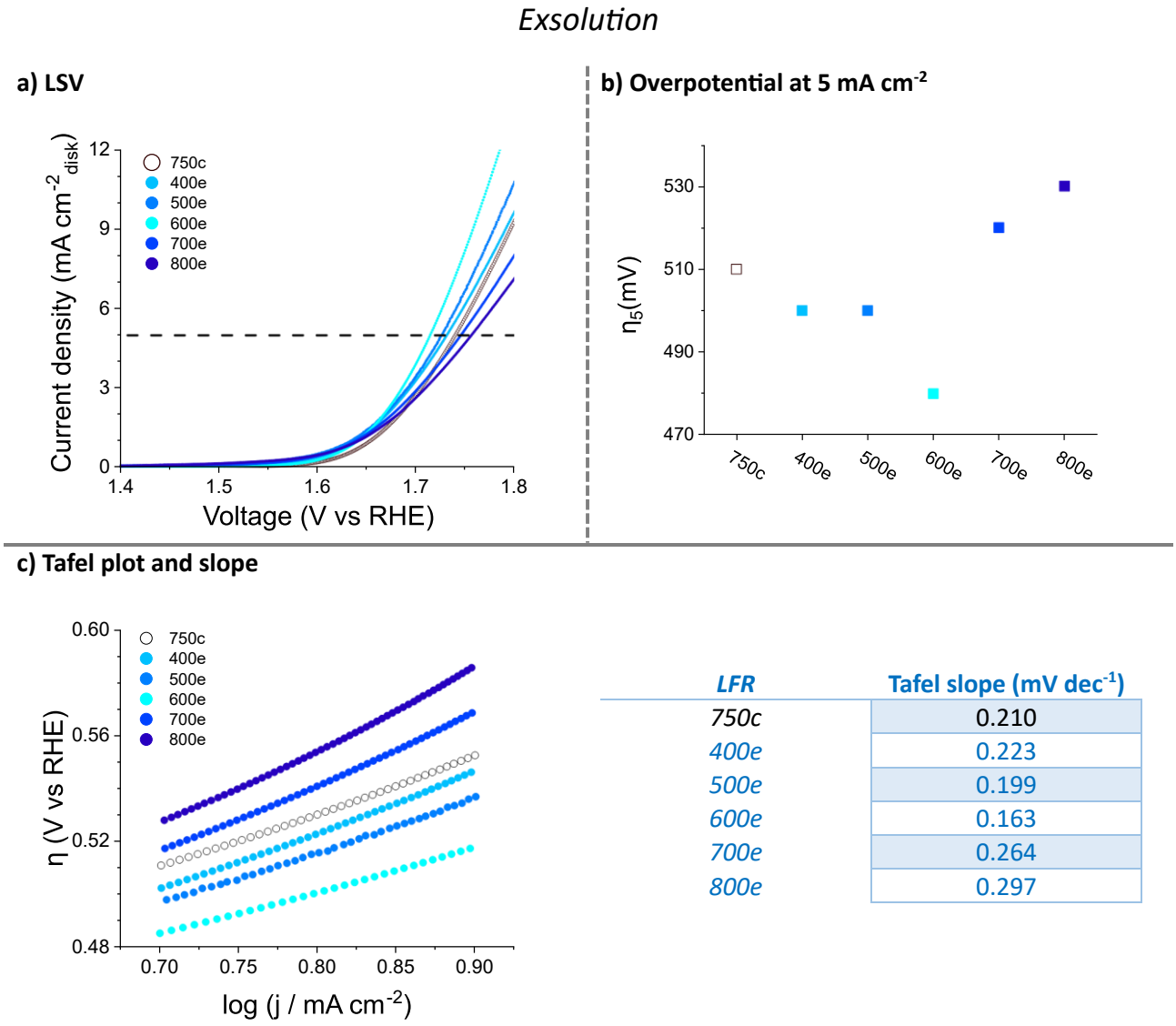

LFR	Tafel slope (mV dec^{-1})
750c	0.210
400e	0.223
500e	0.199
600e	0.163
700e	0.264
800e	0.297

Figure 4.6. a) *Linear sweep voltammetry curves for OER on glassy carbon electrode of LFR_750c and LFR_750c_X00e, dashed line indicates a current density of 5 mA cm^{-2} and from the intersection between this line and LSV curves is obtained* ***b)*** *η_5, overpotentials calculated with respect to the standard oxygen reduction potential (+1.23 V).* ***c)*** *Tafel plot on the left and value of Tafel slope on the right.*

The η_5 implies the use of more energy than thermodynamically expected to drive a reaction, so lower values of η_5 are preferred. The Tafel plot is related to the kinetics of the reaction and less pendent lines are preferred, because with a slightly increase of the overpotential, the current density has a greater increase. It is possible distinguish two groups of samples: the first, exsolved up to 600 °C, have an overpotential lower than the starting perovskite (*LFR_750c*), the second, exsolved at 700 and 800 °C, have higher η_5.

In the first samples η_5 decreases after the exsolution, due to the quantity of ruthenium migrated to the surface. There is not significant difference between *400e* and *500e* samples for this parameter but the Tafel slope of *500e* is lower, while *600e* has the best performance in terms of η_5 and kinetics among the samples of this group. For the samples exsolved at 700 °C and 800 °C, one would expect a higher ruthenium content on the surface and therefore better performance, but on the contrary there is an increase in η_5. A possible

explanation is the formation of a core-shell nanoparticles, where the core is made by ruthenium, while the shell by a lanthanum-based layer (e.g. oxide, hydroxide, carbonate) that covers the core with the consequence of a dramatically reduction of the catalytic activity becoming lower than the starting perovskite. Comparing *700e* and *800e* samples it is possible that the thickness of the La-based capping layer increases with the temperature since *800e* possess higher η_5 and Tafel slope. Moreover, this additional shell layer negatively affects the measured Ru content in the XPS analysis. La_2O_3 is present after the exsolution and starting from a temperature of 600 °C, as evidenced by the Rietveld refinement in the previous chapter. One explanation is that, when ruthenium is segregated, the parent oxide becomes an unstable B cation deficient perovskite, and to return in a stable condition also segregated lanthanum oxide, but at high temperature seems this oxide covers the Ru-NPs due to strong metal-support interaction - SMSI. In view of this hypothesis, it is possible that La_2O_3 partially covers also the exsolved samples at lower temperatures, but not significantly. Summarizing the effect of the exsolution process in the studied perovskite-like, the increase in the exsolution temperature progressively leads to an increase of Ru content on the surface and to better electrocatalytic performances up to 600 °C and after they progressively decrease due the formation of thicker and thicker lanthanum-base covering layer over NPs, presumably La_2O_3.

A similar phenomenon, in which there is a decrease of the catalytic performance for exsolution at high temperature, is reported in Wang Y. et al. work concerning the same type of perovskite but applied in thermocatalysis. **Figure 4.7** (where LFO is referred to $LaFeO_3$ and LFRO to $LaFe_{0.9}Ru_{0.1}O_3$, while 800R is the exsolution performed at 800 °C) shows that the performance of the exsolved sample at a temperature of 800 °C is worse than that without treatment in the first cycle; furthermore, they proved the presence of lanthanum oxide which covered the ruthenium nanoparticles with a decrease of the performance. Of particular interest are the results of the second thermocatalysis cycle in which there is an increase in the performance of the exsolved sample which becomes even better than the sample without treatments. During the thermocatalysis cycle the temperature reaches up to 400 °C and it is hypothesized that the surface of the nanoparticle is cleaned out of lanthanum oxide, thus increasing its performance. Furthermore, various samples exsolved at 800 °C and with mild oxidation at various temperatures were tested, confirming that the temperature of 400 °C is the most suitable for catalysis. For this reason, in the following work, after the exsolution, a mild oxidation at 400 °C is performed.[82]

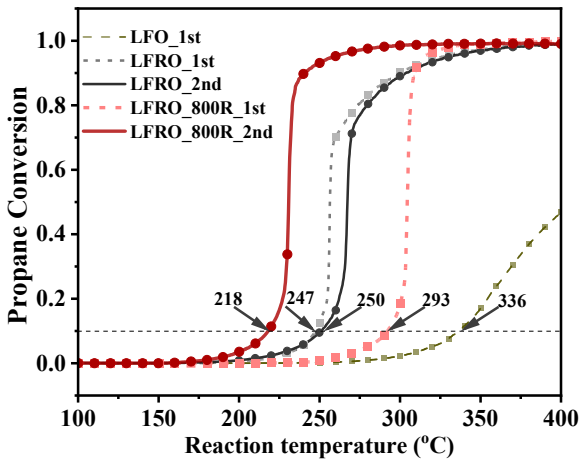

Figure 4.7. *Light-off curves (LFO_1st; LFRO_1st; LFRO_800R_1st, dashed lines) for propane combustion are shown for LFO (Ru-free), LFRO (Ru-doped), and LFRO_800R (Ru exsolved). Propane conversion is measured from room temperature to 400 °C admitting a reaction mixture of C3H8: O2: Ar = 1:10:89 (in volumetric fraction) at a flow rate of 100 mL min^{-1} (standard conditions), and employing 20 mg of catalyst diluted with 40 mg of inert quartz sand. For LFRO_800R the conversion is also measured during natural cooling of the reactor down to room temperature under the reaction stream (LFRO_800R_1st_Cooling).*[82]

After the mild oxidation metallic ruthenium is no longer present in the surface, as confirmed by XPS (**Figure 4.8**), indeed all the ruthenium on the surface is oxidated: part of the metallic ruthenium in nanoparticles becomes RuO_2 while the other part is reincorporated in the parent oxide as Ru^{3+} (or Ru^{4+} in the case the atoms are not fully coordinated in the lattice).

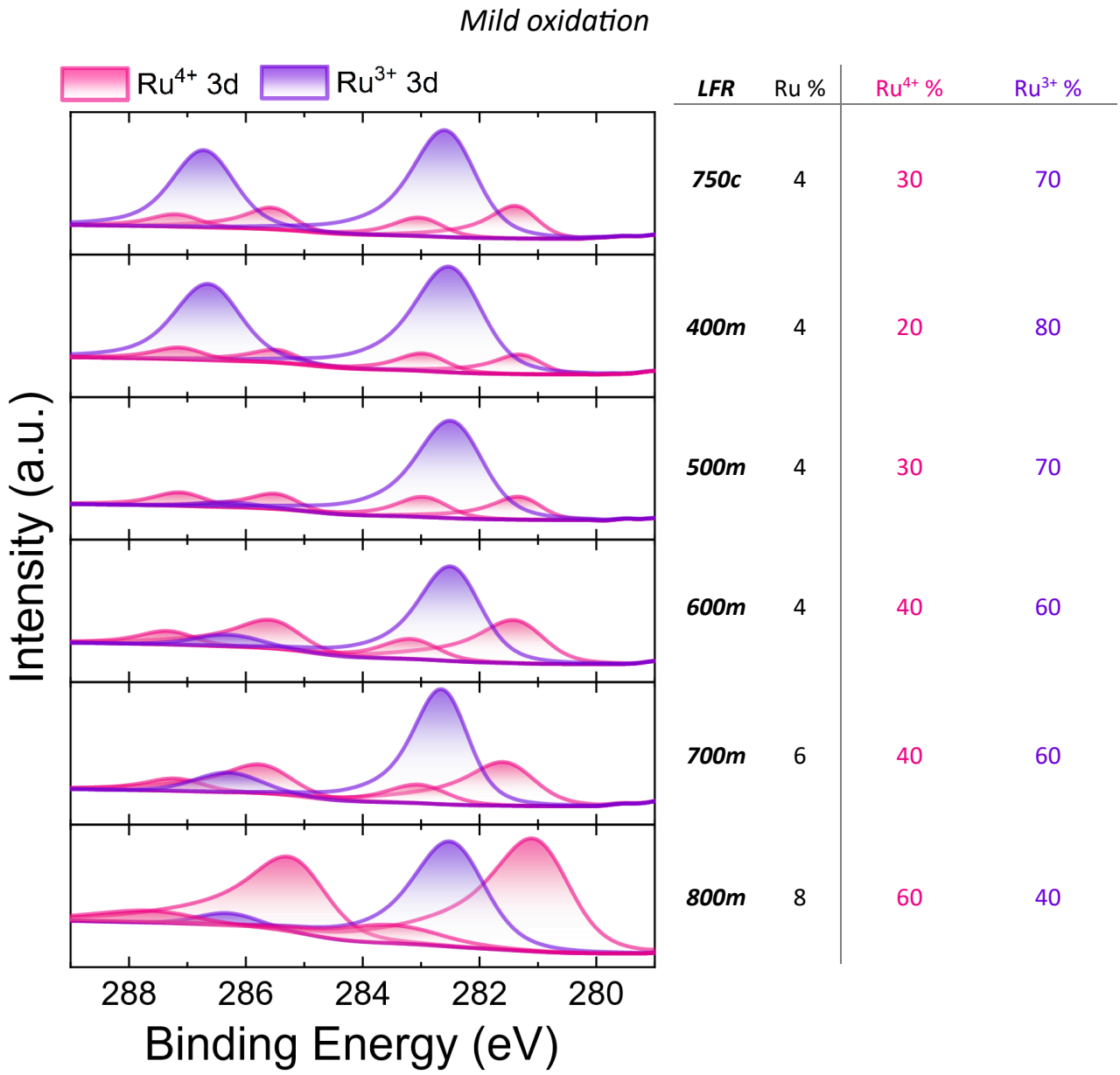

LFR	Ru %	Ru^{4+} %	Ru^{3+} %
750c	4	30	70
400m	4	20	80
500m	4	30	70
600m	4	40	60
700m	6	40	60
800m	8	60	40

Figure 4.8. *Ru 3d deconvoluted peaks from XPS spectra of LFR_750c_X00e_400m (left), atomic percentage in weight of Ru with respect to the total metals of the perovskite-type and the percentages of its oxidation state (right).*

In the case of mild oxidated samples exsolved at 400 °C and 500 °C, the content and the percentage of Ru^{3+} are very similar or lower with respect to the calcinated perovskite, therefore probably all the Ru exsolved is reincorporated, bringing back the surface without NPs in a situation similar to the starting point. Furthermore, the measured Ru content in the mild oxidated samples exsolved at 800 °C increases, despite the possible partial reincorporation, probably because the La_2O_3 no longer covers the NPs. For the mild oxidated sample exsolved at 700 °C the measured Ru content is not changed due to a possible balance between the cleaning of NPs from La-based layer, that increases the measured Ru, and the partial reincorporation of Ru in the parent oxide Since the diameter of the NPs does not change before and after the mild oxidation (SEM image in the previous chapter, **Figure 3.10**), it is likely that the La_2O_3 reacts with the ruthenium of the NPs to form a La, Ru based perovskite-type.

The effect of the mild oxidation on the electrocatalytic activity is presented in **Figure 4.9**.

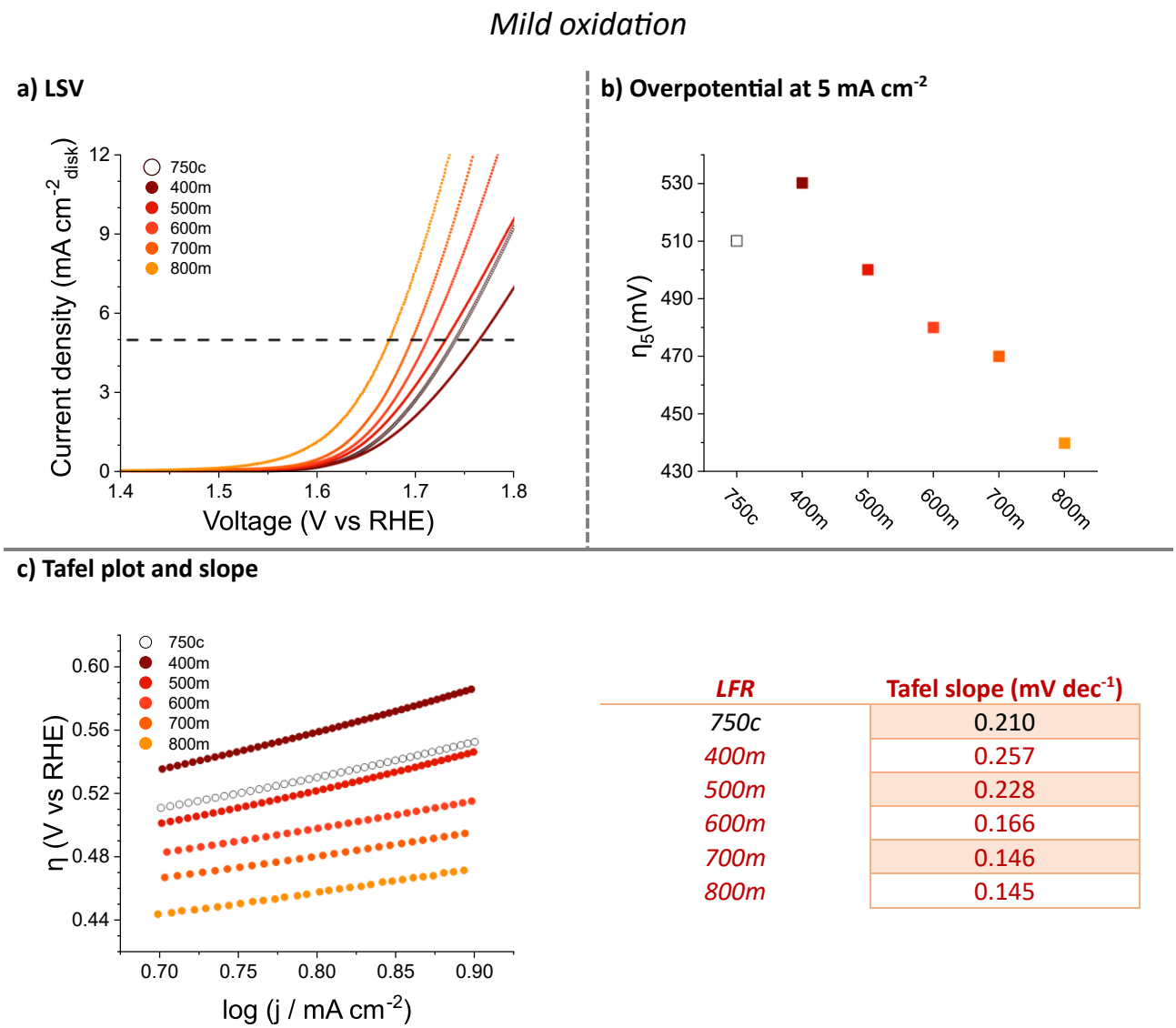

LFR	Tafel slope (mV dec^{-1})
750c	0.210
400m	0.257
500m	0.228
600m	0.166
700m	0.146
800m	0.145

Figure 4.9. a) *Linear sweep voltammetry curves for OER on glassy carbon electrode of LFR_750c and LFR_750c_X00e_400m, dashed line indicates a current density of 5 mA cm^{-2} and from the intersection between this line and LSV curves is obtained* ***b)*** *η_5, overpotentials calculated with respect to the standard oxygen reduction potential (+1.23 V).* ***c)*** *Tafel plot on the left and value of Tafel slope on the right.*

After the mild oxidation new monotonous trends of η_5 and Tafel slope are obtained, and these parameters decrease with the increase of the previous exsolution temperature and follow the content of Ru^{4+}. In the samples *400m* and *500m,* both η_5 and Tafel slope are higher than *LFR_750c* and support the hypothesis that mild oxidation leads the two samples in a pretreatments condition without NPs, while in the other samples, the performances are better than the calcinated, so NPs are probably still presents but made entirely by RuO_2 and no longer covered by La_2O_3 since *700m* and *800m* display the best performances.

A comparison between η_5 of exsolved and mild oxidated samples is presented in **Figure 4.10**, and the effect of mild oxidation is:

- negative for the sample exsolved at 400 °C because the great majority of the ruthenium on the surface if not all is reincorporated in the perovskite-like, so η_5 increases (and also the Tafel slope);
- neutral for the sample exsolved at 500 and 600 °C, the η_5 remains unchanged; a possible explanation is that there is a balance between the re-incorporated ruthenium and the cleaning of the NPs from lanthanum oxide which may be present although not such as to compromise its performance (even if the Tafel slope increase);
- positive for samples exsolved at 700 and 800 °C thanks to the removal of the La_2O_3 layer.

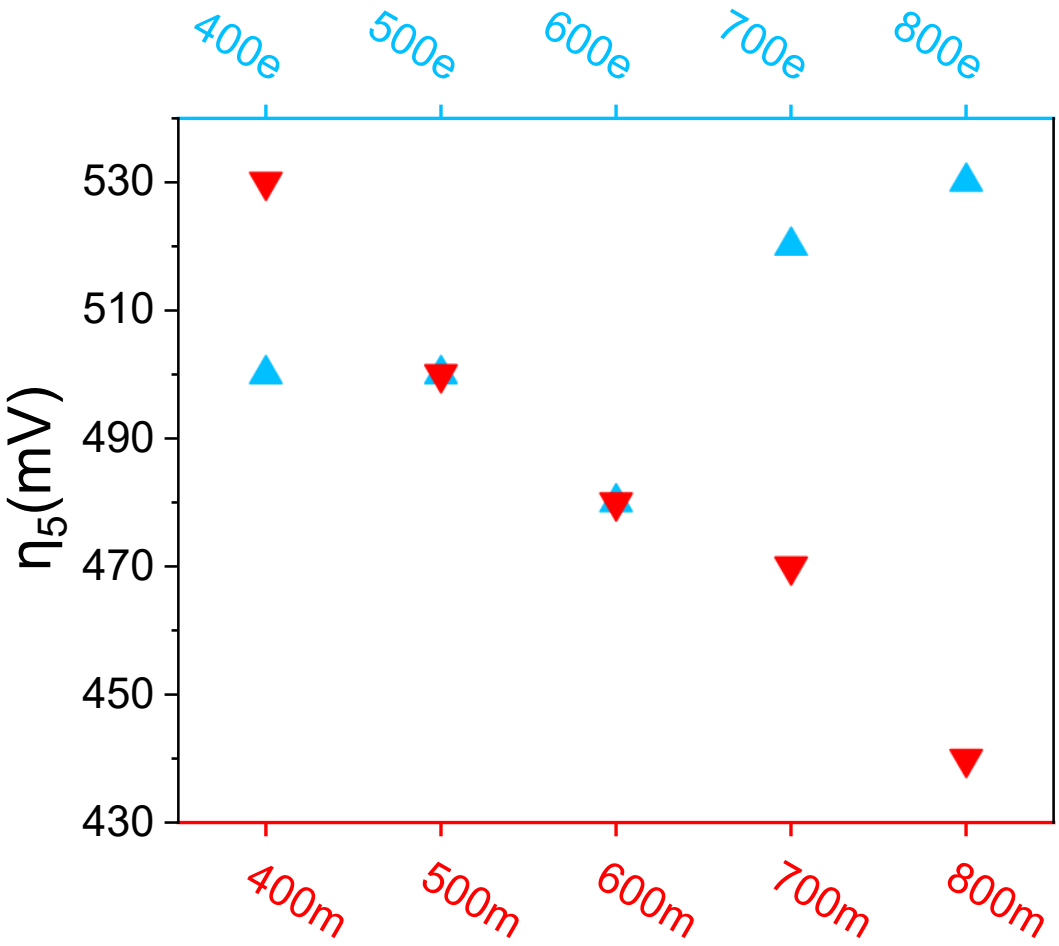

Figure 4.10. *Comparison between the overpotentials at 5 mA of LFR_750c_X00e in sky blue and LFR_750c_X00e_400m in red.*

A summary scheme of how the two treatments modify the surface of the perovskite-like powder is presented in **Figure 4.11**. During the exsolution the ruthenium is brought to the surface generating nanoparticles, the amount of ruthenium on the surface increases as the temperature increases, in addition to the segregation of metallic ruthenium, also lanthanum oxide is formed which will significantly cover the NPs at temperatures higher than 700 °C in the case studied (it is possible that the temperature is lower for samples with greater specific surface area and lower wall thickness), thus decreasing their electrocatalytic performance. When exsolved powders are exposed to air, the surface of the NPs is oxidized, and consequently the actual and effective catalyst in OER is RuO_2. Through a mild exsolution at 400 °C, the NPs are oxidized and are cleaned from the La_2O_3 layer (probably this is combined with process of the ruthenium of the NPs forming a La, Ru based perovskite-type) but a secondary effect is the partial reincorporation of Ru in the matrix.

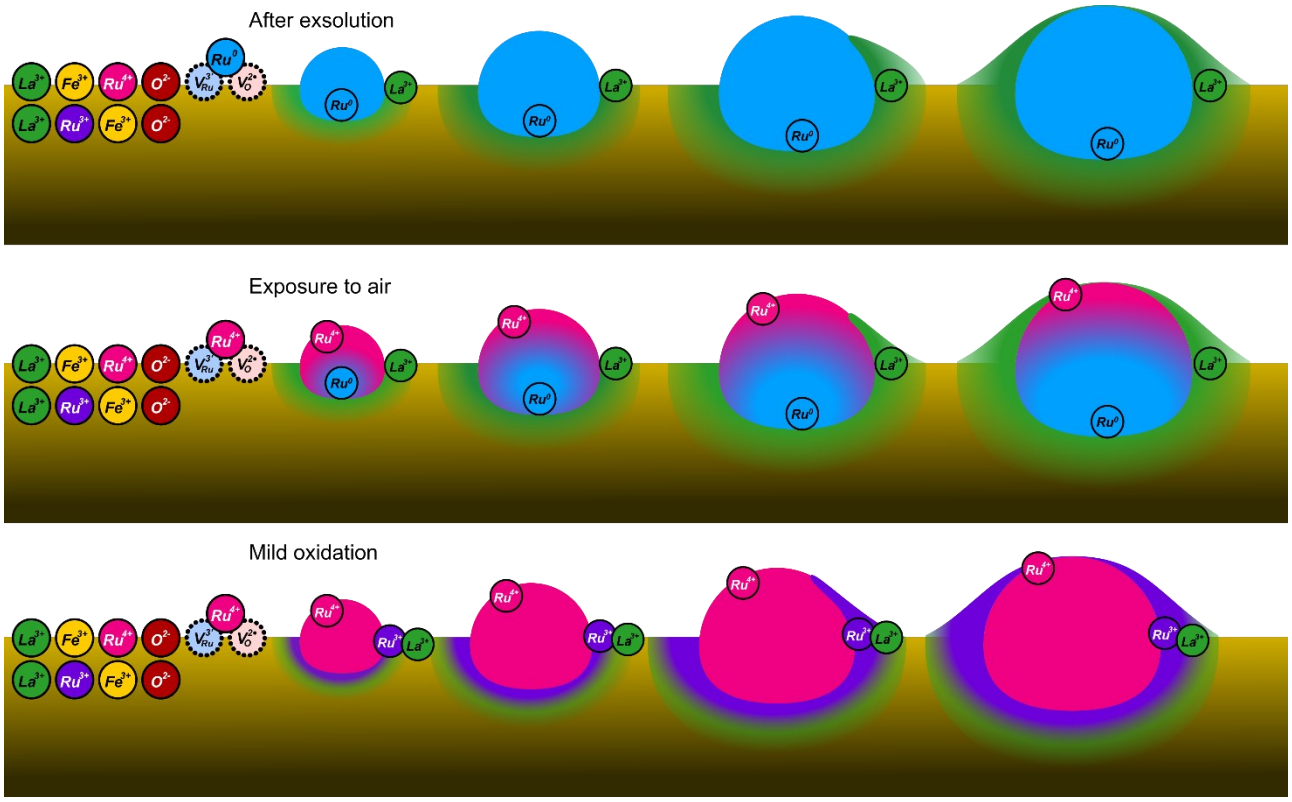

Figure 4.11. *Schematic representation for the surface reconstruction due to the exsolution followed by air exposure and mild oxidation. Image provided by Dr. Jaime Gallego.*

La_2O_3 in the stoichiometric perovskite considerably influences the electrochemical performances of the exsolved samples at high temperatures, by covering the ruthenium NPs drastically lowers the catalytic activity towards OER. Moreover, being La_2O_3 a very strong insulator, it can influence the conductivity of the entire material. Electrochemical impedance spectroscopy is performed for *750c*, *800e* and *800m* where the La_2O_3 has a dominant role because it is mostly present and covers the NPs of *800e*, but also for *600e* and *600m* where lanthanum oxide is present but in smaller quantities and not totally covers the NPs of *600e* the results are presented in **Figure 4.12**. Depending upon the sample, the powder could be made by the following component (with their typical value of bulk energy gap, in brackets): $LaFe_xRu_{1-x}O_3$ (~ 1.9 eV)[83], RuO_2 (~0.5 eV)[84], metallic ruthenium (conductor) and La_2O_3 (~5.5 eV)[85]. It should be reminded that EIS (and the other electrochemical measurements) are not conducted on the perovskite alone but on the system obtained from the deposition of the ink, i.e. consisting of perovskite, carbon black and Nafion.

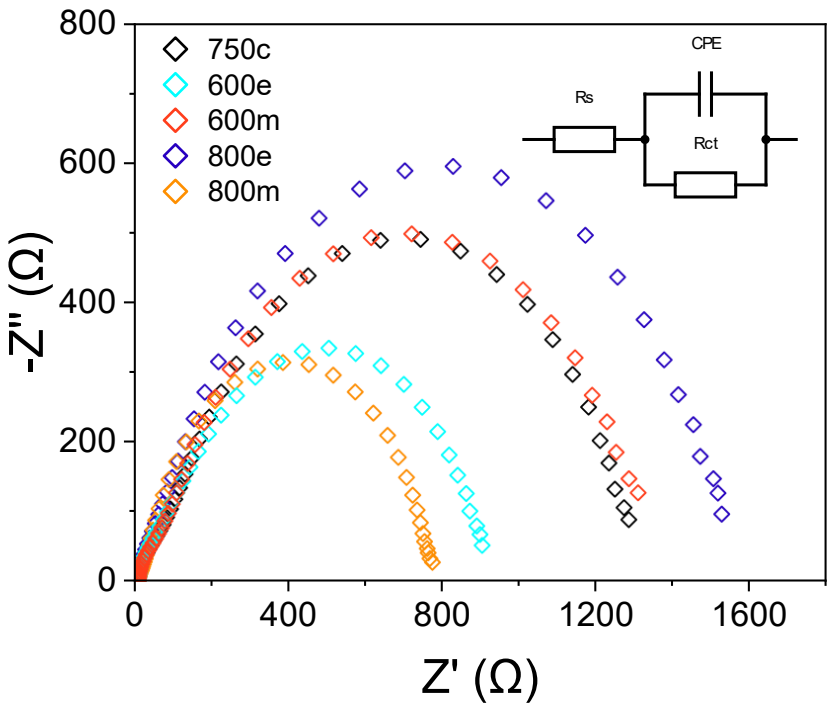

EIS	R_{ct} (Ω)
750c	1300 ± 19
600e	920 ± 13
600m	1340 ± 20
800e	1540 ± 15
800m	759 ± 5

Figure 4.12. *On the left, Nyquist plot curves of EIS for LFR_750c, LFR_750c_600e, LFR_750c_600e_400m, LFR_750c_800e and LFR_750c_800e_400m catalysts recorded 0.6 V (vs Ag/AgCl) in the frequency range 100 kHz to 0.1. The inset is an electrical equivalent circuit used to simulate the impedance data. On the right, the values of R_{ct} obtained from the fitting using the equivalent circuit.*

CPE is the constant phase element and R_s represents the ohmic series resistance, which is mainly caused by the uncompensated electrolyte resistance and by the connection of the electrodes to the instrument, in the case studied is negligible. R_{ct} represents the charge transfer impedance of the materials and, visually in Nyquist plot, is roughly the diameter of the arc curve for the studied samples. After exsolution, *600e* decreases its impedance thanks to the formation of ruthenium NPs and this metallic component in the system increases the conductivity, while in *800e* the impedance increases due the coverage of the NPs by La_2O_3 that isolates the particles from the rest of the system. The mild oxidation has an opposite effect with respect to the exsolution: *600m* returns to possess a resistance very similar to *750c* whereas *800m* shows the lowest resistance of the group. A possible reason for the negative effect in *600m* could be that the oxidation provokes a substantial reincorporation of ruthenium; indeed the XPS results of *600m* are near to *750c*, so even if there are NPs of RuO_2 on the surface, they are very small and do not provide a significative contribution to the conductivity; furthermore possible La_2O_3 residues lead to an increase of impedance In *800m,* the NPs are cleaned from lanthanum oxide and larger than those of *600m* so this positively affects the conductivity.

Regenerated LFR

Instead of performing the mild oxidation, it is possible to do an oxidation at higher temperature, 750 °C, capable of reincorporating all the ruthenium on the surface even in the samples exsolved at highest temperature. The underlying idea to perform this treatment is to regenerate the catalyst, therefore bringing back the exsolved sample in a condition like the starting one *750c*. Compared to *750c* which has a homogeneous distribution of the doped Ru-atoms, the regenerated catalyst has a ruthenium enrichment close to the surface. Performing a second exsolution in the regenerated powder, more quantity of Ru exsolved is expected than the analogous non-regenerated sample exsolved at the same temperature because the Ru atoms are nearer to the surface.[61]

The sample chosen to be regenerate is *800e* , which has worse electrochemical performances due to the presence of La_2O_3 that covers the NPs, but it possesses the major quantity of exsolved ruthenium, and therefore when the high oxidation is performed there is a higher enrichment of ruthenium on the parent oxide surface. The second exsolution is at 600 °C, a temperature that has proved to be optimal for bringing the highest quantity of ruthenium to the surface without a significant presence of lanthanum oxide which would compromise the catalysis performances. A representation of the entire process with the expected desirable result is presented in **Figure 4.13**.

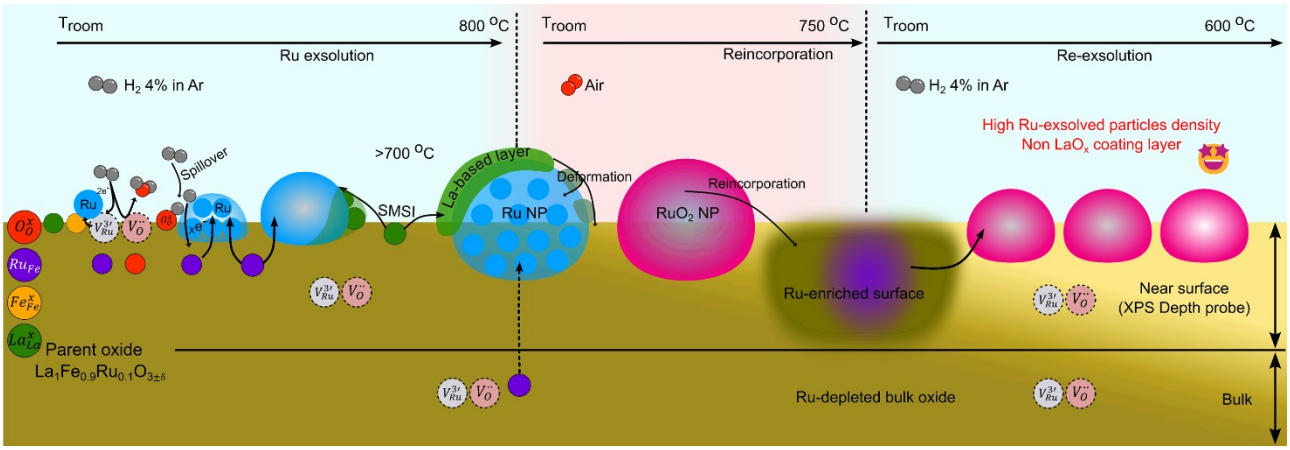

Figure 4.13. *Schematic representation of the exsolution in H_2 at 800 °C (increasing the temperature bigger nanoparticles are formed and starting from 700 °C lanthanum oxide cover the NPs), oxidation in air at 750 °C (a mild one oxidates the metallic ruthenium of NPs to RuO_2 while a high one at 750 °C reincorporates the ruthenium in the parent oxide enriching the surface) and second exsolution in H_2 at 600 °C (since the surface is enriched of the noble metal, more ruthenium is exsolved respect to the first exsolution). Image provided by Dr. Jaime Gallego.*

These initial hypotheses are confirmed by XPS spectra, in **Figure 4.14**, where all the samples obtained by each step are presented to follow the evolution of the entire process which starts from the initial perovskite *750c* to the last mild oxidated sample exsolved for the second time.

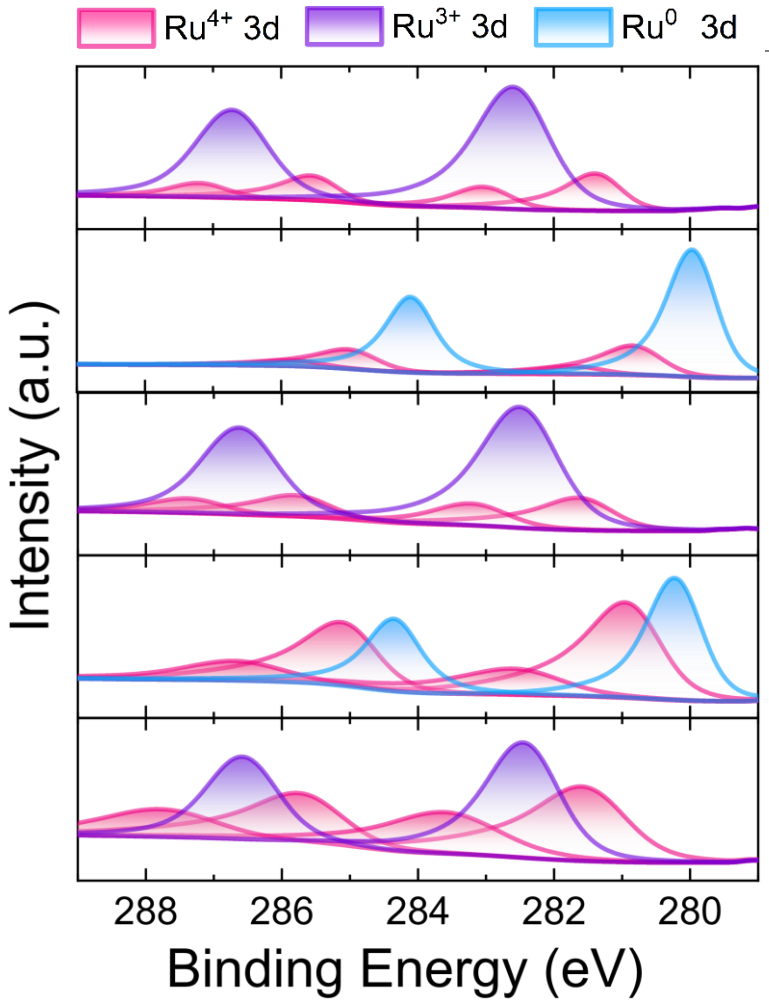

LFR	Ru %	Ru^{4+} %	Ru^{3+} %	Ru^{0} %
750c	4	30	70	/
800e	6	30	/	70
750h	8	30	70	/
600e2	7	60	/	40
600m2	10	60	40	/

Figure 4.14. *Ru 3d deconvoluted peaks from XPS spectra of LFR_750c, LFR_750c_800e, LFR_750c_800e_750h, LFR_750c_800e_750h_600e2 and LFR_750c_800e_750h_600e2_400m2 (left), atomic percentage in weight of Ru with respect to the total metals of the perovskite-type and the percentages of its oxidation state (right).*

The regenerated sample, *750h*, has a higher Ru amount on surface than the *750c*, confirming the ruthenium enrichment after the oxidation at high temperature; moreover, the relative quantities of Ru^{3+} and Ru^{4+} are equal in the two samples, suggesting that all the ruthenium comes back in the parent oxide. After the second exsolution the measured ruthenium content is lower than *750h*, this could be due to shadow effect and presence of La_2O_3, however Ru-content is higher than the analogous *600e* (derived from *750c*) and even higher than *800e*. After a mild oxidation of *600e2*, the measured amount of the noble metal increases. An increase following the mild oxidation was found previously in the *LFR_750c_800e_400m* where the lanthanum oxide is cleaned from NPs, therefore it is possible that *600m2* is in a similar condition. Indeed, in *600e2*, there is significant amount of La_2O_3 precisely because the amount of exsolved ruthenium is greater, even if the coverage of nanoparticles is only partial.

Despite the excellent quantities of ruthenium on the surface, the electrochemical measurements give undesirable results, presented in **Figure 4.15**. The entire regenerated group (*750h*, *600e2* and *600m2*) has very bad electrochemical performances, and a negative memory effect regarding the presence of lanthanum oxide is supposed (see below).

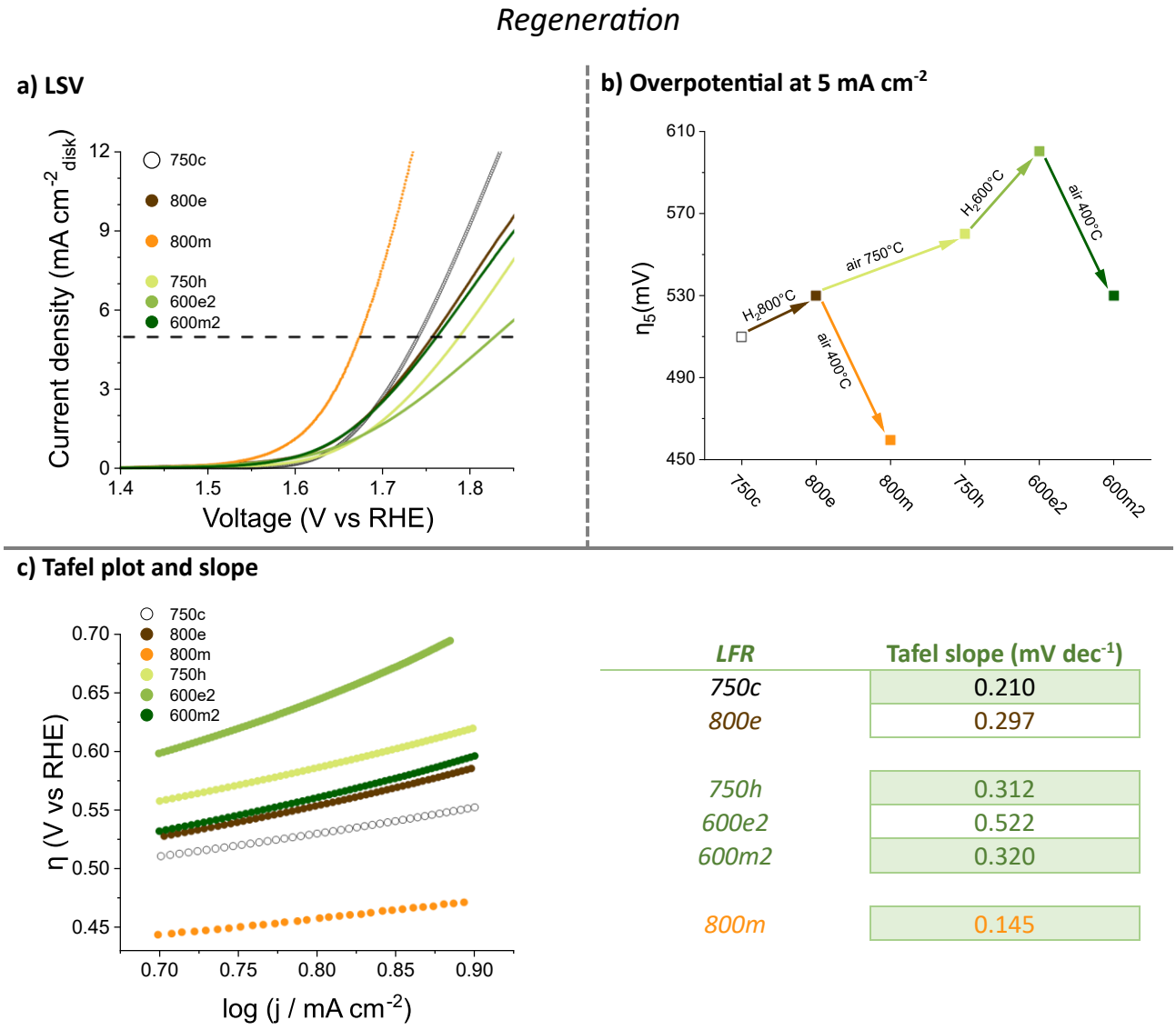

LFR	Tafel slope (mV dec^{-1})
750c	0.210
800e	0.297
750h	0.312
600e2	0.522
600m2	0.320
800m	0.145

Figure 4.15. a) *Linear sweep voltammetry curves for OER on glassy carbon electrode of LFR_750c, LFR_750c_800e, LFR_750c_800e_400m, LFR_750c_800e_750h, LFR_750c_800e_750h_600e2 and LFR_750c_800e_750h_600e2_400m2, dashed line indicates a current density of 5 mA cm^{-2} and from the intersection between this line and LSV curves is obtained* ***b)*** *η_5, overpotentials calculated with respect to the standard oxygen reduction potential (+1.23 V).* ***c)*** *Tafel plot on the left and value of Tafel slope on the right.*

The η_5 and Tafel slope of *750h* are higher than the analogous *750c,* and even than *800e* that has NPs covered by lanthanum oxide. After the second exsolution there is a worsening of performance, suggesting a critical role for La_2O_3, even if it doesn't totally cover the NPs. The mild oxidation cleans the surface from La_2O_3, and *600m2* has the highest amount of ruthenium among all the stoichiometric samples, so the highest performances are expected, but they increase slightly. The sample *600m2* has better performance than *600e2*, probably due to the cleaning of the surface from lanthanum oxide, but the overall performance is still bad, failing even to match the η_5 and Tafel slope of *750c*. These results suggest that the cause of the failing of the regeneration for electrocatalysis is not related to the surface of the materials: it is possible that in the

near surface and in the bulk the lanthanum oxide is stabilized by the oxidation at high temperature, forming an isolate layer. With the second exsolution the amount of La_2O_3 increases, enhancing the electrical isolation and partially covering the NPs; after the mild oxidation the RuO_2 NPs are cleaned but the isolated layer remains. The route of mild oxidation is preferred to the high one, in which the regeneration achieves the ruthenium enrichment of the surface, but probably also generates an isolating layer of La_2O_3 which makes the material unsuitable for electrocatalysis. This regeneration process on the stoichiometric perovskite could be used for thermocatalysis where electrical conductivity has not a crucial role.

Exsolution and mild oxidation of $La_{0.9}Fe_{0.9}Ru_{0.1}O_3$ – L0.9FR

A non-stoichiometric LFR is prepared with a deficit of lanthanum ($La_{0.9}Fe_{0.9}Ru_{0.1}O_3$), leading to a A/B (La/(Fe+Ru)) ratio of 0.9. This non-stoichiometric perovskite-type should attenuate the problem derived by La_2O_3. In ABO_3 the exsolution leads to the formation of B and of an unstable B-deficient perovskite, the latter forms the relative stoichiometric species and an A-oxide to re-establish the stability (**Eqn. 4.1**). Meanwhile, the A-deficient perovskite starts from an unstable condition of non-stoichiometry and through exsolution releases the excess (or a part) of B and forms the analogous stable composition (**Eqn. 4.2**).

Stoichiometric: $$ABO_3 \xrightarrow{Exsolution} AB_{1-\alpha}O_{3-\delta'} + \alpha B \rightarrow (1-\alpha)ABO_{3-\delta''} + \alpha AO + \alpha B \quad \textbf{(4.1)}$$

A-deficient: $$A_{1-\alpha}BO_{3-\delta} \xrightarrow{Exsolution} (1-\alpha)ABO_3 + \alpha B \quad \textbf{(4.2)}$$

Moreover, an A-deficient perovskite, $A_{1-\alpha}BO_{3-\delta}$, presents more oxygen vacancies than the stoichiometric type, so the exsolution process is favored. Indeed, the general driving force of exsolution is oxygen vacancies, which destabilize the perovskite lattice and therefore B-site species are exsolved to reach the stability, establishing a stoichiometric perovskite-like material. Starting from the La-deficit sample, where oxygen vacancies are already present in the structure, the exsolution should lead to more ruthenium on surface than the case of stoichiometric LFR.

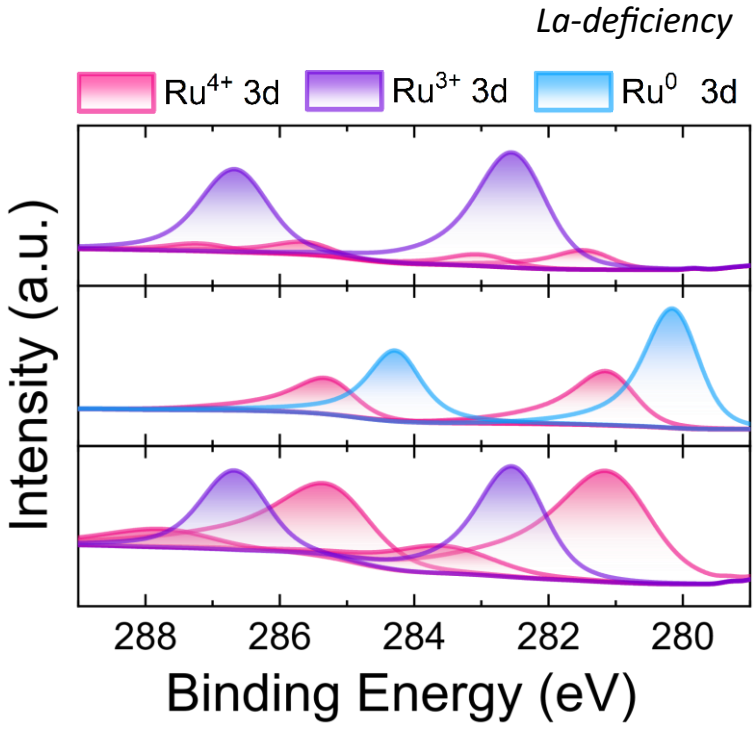

L0.9FR	Ru %	Ru^{4+} %	Ru^{3+} %	Ru^0 %
750c	4	20	80	/
600e	5	40	/	60
400m	4	70	30	/

Figure 4.16. *Ru 3d deconvoluted peaks from XPS spectra of L0.9FR_750c, L0.9FR_750c_600e, L0.9FR_750c_600e_400m (left), atomic percentage in weight of Ru with respect to the total metals of the perovskite-type and the percentages of its oxidation state (right).*

In the XPS spectra (**Figure 4.16**), L0.9FR_750c presents an amount of the total measured ruthenium on the surface equal to the case of *LFR_750c* (previously studied). After exsolution the Ru-content slightly increases in *0.9_600e*, while in the analogous *LFR_750c_600e* it remains constant at the value of *750c*, so the exsolution process is favored in L0.9FR sample. After the mild oxidation, the Ru-content decreases due to the partial reincorporation of the noble metal in the perovskite lattice, and the metallic ruthenium is oxidated like the stoichiometric case, even if the relative amount of Ru^{4+} is more than *600m*. Despite of the similar results of the La-deficit samples with respect to the stoichiometric one in total measured Ru-content, the electrochemical data are quite different (**Figure 4.17**). For a quicker comparison, the electrochemical results of LFR are repeated.

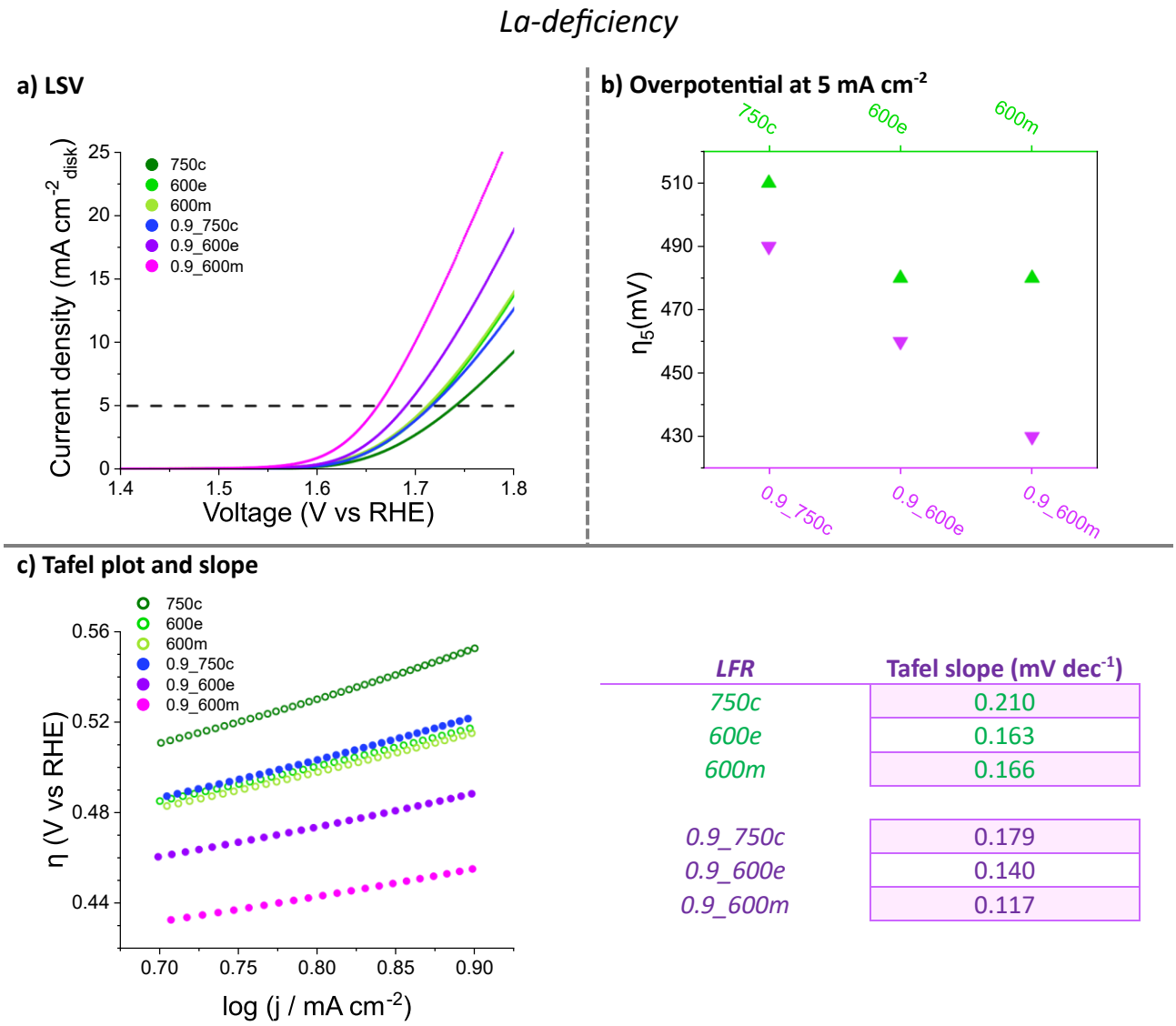

LFR	Tafel slope (mV dec^{-1})
750c	0.210
600e	0.163
600m	0.166
0.9_750c	0.179
0.9_600e	0.140
0.9_600m	0.117

Figure 4.17. a) *Linear sweep voltammetry curves for OER on glassy carbon electrode of L0.9FR_750c, L0.9FR_750c_600e, L0.9FR_750c_600e_400m and the analogous LFR for comparison, dashed line indicates a current density of 5 mA cm^{-2} and from the intersection between this line and LSV curves is obtained* ***b)*** *η_5, overpotentials calculated with respect to the standard oxygen reduction potential (+1.23 V).* ***c)*** *Tafel plot on the left and value of Tafel slope on the right.*

Both η_5 and Tafel slope are lower in the *0.9_750c* than the analogous stoichiometric sample: indeed it is well known that oxygen vacancies especially on the surface can enhance the OER[86], affecting the adsorption of intermediates on the catalyst surface, changing the rate-determining step, modifying the electronic structure

and enhancing electronic conductivity. Moreover, the typical mechanism of perovskite for OER is LOM, and oxygen vacancies can increase the number of active sites. After exsolution, *0.9_600e* possesses lower η_5 and Tafel slope than *600e* because the quantity of exsolved ruthenium is higher and possible traces of lanthanum oxide are lower. An unexpected result is given by the mild oxidation, as already mentioned this treatment is responsible for the partial reincorporation of the exsolved ruthenium in the parent oxide and of the cleaning of the NPs. The latter influences more the stoichiometric sample than L0.9FR because the amount of La_2O_3 formed during the exsolution should be greater, although in *600m*, the two effects compensate each other and the electrochemical performances are roughly the same of *600e*. In *0.9_600e*, since the La_2O_3 should be even less than the stoichiometric case, the mild oxidation should only deplete the surface of ruthenium, leading to a decrease in the performance and not to an increase as it actually occurs. A possible explanation for this increase should be related to the overall system including both the surface and the bulk, in particular to a decrease of the impedance as shown in **Figure 4.18**.

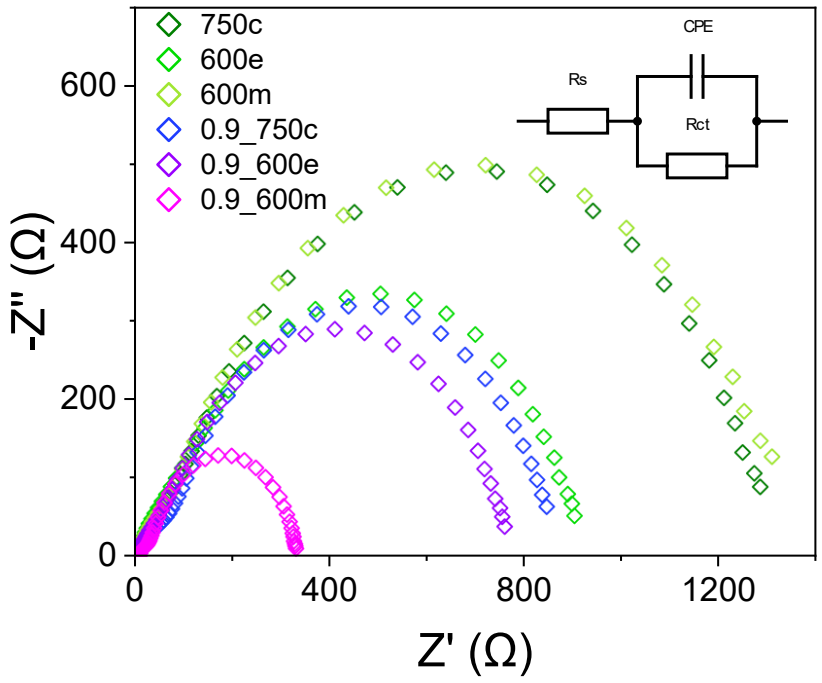

EIS	R_{ct} *(Ω)*
750c	1300 ± 19
600e	920 ± 13
600m	1340 ± 20
0.9_750c	860 ± 15
0.9_600e	760 ± 10
0.9_600m	322 ± 4

Figure 4.18. *On the left, Nyquist plot curves of EIS for L0.9FR_750c, L0.9FR_750c_600e, L0.9FR_750c_600e_400m catalysts and the analogous LFR for comparison recorded at 0.6 V (vs Ag/AgCl) in the frequency range 100 kHz to 0.1 Hz. The inset is an electrical equivalent circuit used to simulate the impedance data. On the right, the values of R_{ct} obtained from the fitting using the equivalent circuit.*

In general, the impedance of the L0.9FR's group is lower than LFR's. The deficit of the A cation generates a deficit of positive charge in the material; to achieve the electroneutrality, oxygen vacancies can be formed, and also the oxidation state of part of B cations can change, thus resulting in redox couples (in the case studied: Fe^{3+}-Fe^{2+} and Ru^{4+}-Ru^{3+}-Ru^{2+}, but the latter is unstable and could disproportionate) which increase the electrical conductivity. In *0.9_600e*, even if the quantity of redox couples decreases, the formation of metallic NPs slightly increases the conductivity (furthermore a little quantity of lanthanum oxide is segregated). The RuO_2 NPs remain after the mild oxidation, moreover a part of the Ru on the surface is brought back in the parent oxide, so redox couples are partially re-established; the significative presence of both factors results in the lower impedance in the *0.9_600m*.

Electrochemical active surface area

Another investigated property is the electrochemical active surface area (ECSA), which represents the area of the electrode material that is accessible to the electrolyte, and it is used for charge transfer and/or storage. The chosen samples belong to the three studied groups (stochiometric, regenerated and non-stoichiometric) in the same condition of exsolution at 600 °C. The values are shown in **Table 4.1**, and a common trend among the three groups can be noticed: ECSA decreases after the exsolution and increases after the mild oxidation.

ECSA ($mm^2 g^{-1}$)	***LFR_750c***	***LFR_750c_ 800e_750h***	***L0.9FR_750c***
Before Treatments	46.4 (0.28)	55.1 (0.18)	60.3 (0.31)
Exsolution at 600 °C	38.6 (0.10)	36.4 (0.25)	34.2 (0.10)
Mild oxidation	55.4 (0.15)	80.9 (0.26)	81.3 (0.10)

Table 4.1. *ECSA of 750c, 600e, 600m, 750h, 600e2, 600m2, 0.9_750c, 0.9_600e and 0.9_600m. ECSA is calculated dividing the double layer capacitance of the sample with the typical specific capacitance in alkaline media (40 $\mu F\ cm^{-2}$) and normalizing to the catalyst loading. Inside the brackets are reported the standard deviation.*

Giving an explanation to this trend of ECSA is very difficult because the samples at each step undergo morphological and chemical changes on the surface, and also the conductivity of the catalysts change. Possible errors in the evaluations of ECSA can be related to the specific capacitance: indeed, the same C_S value can be used by assuming that the studied catalysts are equally conductive; moreover, C_S is a propriety related both to the electrolyte and the catalyst material, which is modified by the thermal treatments. Furthermore, ECSA can be affect by OH^- ion adsorption and intercalation. However, a similar a trend is found by Lei fu et al. and they explain the decrease of ECSA after exsolution to a decrease of specific surface area, while the increase after the mild oxidation signifies that in-situ growth of RuO_2 nanoparticles is more beneficial to catalyze OER.[66]

Chapter 5

Experimental section

Methods

Preparation of Ru-doped $LaFeO_3$-based perovskite powders

In the case of $LaFe_{0.9}Ru_{0.1}O_3$, in a beaker of 1 L, 1.73 g (4 mmol) of $La(NO_3)_3 \cdot 6H_2O$ (99.99 %, Chempur), 1.45 g (3.6 mmol) of $Fe(NO_3)_3 \cdot 9H_2O$ (> 98 %, Sigma Aldrich), 2.70 g (0.4 mmol) of $Ru(NO)(NO_3)_3$ (typical 1.5 % in mass of equivalent Ru in dilute HNO_3, Sigma Aldrich) and 0.60 g (8 mmol) of glycine (> 99 %, Sigma Aldrich), are dissolved in a minimal quantity of distilled water necessary to have a solution. While being stirred the solution is heated on a hot plate to vaporize most of the water at 80 °C – 90 °C. Once the solution became a gel with a honey-like consistency, it is removed from the heating plate. The temperature of the hot plate is raised to 300 °C and, after reaching this temperature the beaker is put back on top. Then the combustion occurs giving the burned powder. In the case of $La_{0.9}Fe_{0.9}Ru_{0.1}O_3$ the procedure is analogous, except for the quantity of $La(NO_3)_3 \cdot 6H_2O$ which is 1.56 g equal to 3.6 mmol.

Heat treatments

All the thermal treatments (calcination, exsolution and oxidation) are performed with a heating rate of 5 °C min^{-1} and with 3 hours isotherm at the target temperature. Calcination is performed in air at 750 °C. The exsolution process is carried out in 4% v/v H_2/Ar at 400 °C, 500 °C, 600 °C, 700 °C and 800 °C. The oxidation treatment is performed in air at 400 °C (mild oxidation) or 750 °C (high oxidation).

Preparation of the ink

The preparation procedure for the preparation of the ink is adapted from Jiang et al.[67]. The powders are ground and 9 mg of them are mixed with 3 mg of acetylene black (AB) to enhance the conductivity. 8 mg of this mixture are then dispersed in a solution of 2 mL isopropanol and 20 µL of Nafion solution (5 % mass fraction – Sigma Aldrich) using an ultrasonic bath for 10 min. Finally, 5 µL of the ink is deposited dropwise (2 depositions of 2.5 µL each) on a glassy carbon working electrode (diameter 3 mm), letting it dry naturally. The final loading of the perovskite is about 0.283 mg cm^{-2}.

Characterization techniques

N_2 physisorption

N_2 physisorption is performed at 77 K, recording the isotherms with the hysteresis loops to determine the samples' specific surface area and pore size distribution. All the powders are degassed under vacuum at 100 °C for 12 h before to the measurement. Then, the data are analyzed using the software ASiQwin (Version 5.21, Quantachrome Corporation). The specific surface area is calculated using the Brunauer-Emmett-Teller (BET) method in the relative pressure range of $P P_0^{-1}$ = 0.11 to 0.31.[80,81] The pore size distribution is determined by applying the nonlocalized density functional theory (NLDFT) kernel of nitrogen at 77 K on silica/zeolites to the adsorption branch of the isotherm, assuming a cylindrical pore geometry.

XRD

To verify the final crystallographic phases, powder diffraction is performed using a Panalytical X'Pert PRO diffractometer equipped with a Cu-K_α radiation (λ = 1.5418 A) source operated at 40 kV and 40 mA. XRD patterns in the 2θ range of 15° - 75° are collected with a step size of 0.013° and an integrated counting time of 2 s per step. Then, the diffractograms are fitted with the software HighScore Plus (Version 3.0.5, PANalytical).

XPS

To investigate the surface reconstruction during exsolution and oxidation, X-ray photoelectron spectroscopy is performed with a PHI 5000 VersaProbe II Scanning ESCA Microprobe (Physical Electronics GmbH) with monochromatized Al-K_α X-ray source (1486.6 eV) in high power mode (beam size 1300 µm x 100 µm, X-Ray power: 100 W). Time steps of 50 ms, a step size of 0.2 eV and an analyzer pass energy of 46.95 eV are used for measuring the detailed spectra. For the general spectra "survey" 1 sweep is performed and 30 sweeps or a P/N ratio equal to 180 are set for the detailed region. The sample surface is charge neutralized with slow electrons and argon ions, and the pressure is in the range from 10−7 Pa to 10−6 Pa during the measurement. Data analysis is performed using the CasaXPS software (Version 2.3.18, Casa Software Ltd.) setting to 284.8 eV the C 1s signal and using the Shirley background.

SEM-EDX

To analyze the morphology and the chemical composition of the samples, Scanning Electron Microscopy and Energy-Dispersive X-ray spectroscopy are performed respectively. The former analysis is carried out with a ZEISS GeminiSEM 560, equipped with an in-lens detector for high resolution, setting an acceleration voltage of 1.00 kV, and automatically adjusted current, at a working distance of 2.0 mm. For the latter, an X-Max 50 detector (Oxford Instruments) at a working distance of 5 mm, acceleration voltage of 50 keV, and a current of 2.2 nA is used.

TGA-MS

Thermogravimetric analysis coupled with mass spectrometry is applied to better understand the processes of polymer and nitrates decomposition inside the pores as well as to check the presence of carbonaceous material left. The measurements are performed on a STA409PC Luxx thermogravimetric analyzer (Netzsch) over a temperature range from 25 °C to 850 °C with a heating rate of 5 °C min^{-1} in synthetic air (80 % N_2, 20 % O_2, in volumetric fraction). At the same time, mass spectra are recorded on a QMS 403 Ae olos Quadro quadrupole mass spectrometer (Netzsch) connected inline to the TGA. The following peaks of m/z 12, 14, 18, 28, 30, 44, 46 are selected to monitor C^+, N^+, H_2O^+, CO^+, NO^+, CO_2^+, N_2O^+, respectively.

Electrochemical measurement

The electrocatalytic OER activity of the samples is studied with a PGSTAT204 (AutolabMetrhom) used as potentiostat and equipped with an impedance module. A standard three-electrodes cell system is adopted for all the measurements performed at 25 °C in a KOH 1 M solution prepared with Milli-Q water. The working electrode is a glassy carbon one (GC, 0.07 cm^2), which, before drop-casting, is pre-polished on a polishing cloth with a 50 nm alumina slurry, rinsed with Milli-Q water, and let dry in air. A Pt plate is used as the counter electrode, and the reference one is a saturated Ag/AgCl electrode. The electrochemical measurements are performed in the following order. First, cyclic voltammetry (CV) is run 5 times with 0.01 V steps in the potential range 0 V to 1 V (vs Ag/AgCl) with a scan rate of 0.05 V s^{-1} to activate the electrode. Then, for the calculation of the double layer capacitance, CV scans are run 5 times with 0.01 V steps in the potential range 0 V to 0.15 V (vs Ag/AgCl) with a rate of 0.2 V s^{-1}, 0.4 V s^{-1}, 0.6 V s^{-1}, 0.8 V s^{-1}, 1 V s^{-1}, and 1.2 V s^{-1} for every set of 5 scansions. The OER activity is evaluated by performing linear sweep voltammetry (LSV) with 0.01 V steps in the potential range 0 V to 1 V (vs Ag/AgCl) with a rate of 0.01 V s^{-1}. Finally, electrochemical impedance spectroscopy (EIS) is measured at 0.6 V (vs Ag/AgCl) in the frequency range 100 kHz to 0.1 Hz.

Chapter 6

Conclusions and outlooks

This Master Thesis work investigates, describes and discusses the influence of the exsolution process and subsequent treatments on physico-chemical and electrocatalytical properties of Ru-doped $LaFeO_3$-based perovskite, with an eventual enhancement of the starting material's activity toward the electrocatalytic oxygen evolution reaction (OER). The catalysts are synthesized via sol-gel auto-combustion, a fast and simple method to obtain ceramic materials. After calcination, XRD diffractograms show a single crystalline phase. The calcination is carried out at 750 °C under static air. TGA-MS highlights that a lower temperature around 650 °C could be used. The single phase belongs to the orthorhombic crystalline system typical of $LaFeO_3$; no one else phase is detected, indicating the effective substitution of Ru-atom in the perovskite lattice, therefore, the success of doping. Following the exsolution, the main perovskite-type phase remains, but secondary phases appear in small quantities, such as lanthanum oxide and hydroxide, starting from a temperature of 600 °C. SEM does not always distinguish the dimensions of NPs at all temperature but the NP reach a maximum diameter of 20 nm after exsolution at 800 °C. N_2 physisorption analysis prove that the calcinated powders are mesoporous and possess a discrete specific surface area of 13 $m^2 g^{-1}$ that slightly decreases after the thermal treatments.

In the stoichiometric perovskite, as the exsolution temperature increases, the amount of ruthenium on the surface (tracked by the Ru signals in XPS spectra) increases, therefore the catalytic activity increases up to 600 °C. In addition to forming metallic ruthenium, lanthanum also segregates forming a La-based compound (e.g. oxide, hydroxide, carbonate), which at high temperatures (starting from 700 °C in the studied samples) covers the ruthenium NPs due to the strong metal support interaction, dramatically reducing their catalytic performance. Mild oxidation treatment is required to clean the Ru nanoparticles from the La-based layer, making the samples exsolved at 700 °C and 800 °C the best catalyst for OER among the samples of the stoichiometric group. The side effect of mild oxidation is the partial re-incorporation of the exsolved ruthenium into the matrix, it is significant when the amount of ruthenium on the surface is not high, and therefore, for samples exsolved at low temperatures, the mild oxidation makes them worst performing. The presence of NPs decreases the impedance of the catalyst while the La-based isolating capping layer increases it. The mild oxidation removes this layer but reincorporates part of the exsolved ruthenium; therefore, depending on the sample, it can positively or negatively affect the impedance.

The high oxidation aims to reincorporate all the exsolved ruthenium by regenerating the perovskite. It is applied to the sample exsolved at 800 °C because it has the greatest quantity of Ru on the surface. It brings the Ru in the parent oxide, but with the difference of having the area close to the surface already rich in ruthenium thanks to the previous exsolution process. Starting from this "regenerated" perovskite, a second exsolution is carried out at 600 °C (temperature at which there is the largest quantity of exsolved ruthenium without the lanthanum-based layer significantly covering the NPs), compared to the first, the noble metal on the surface it is greater because it is already present in its vicinity. Unfortunately, the performances of these perovskites are very bad despite the large amount of Ru on the surface, this finding to be ascribed to the impedance of the material, most likely following the repeated segregations an insulating La-based layer is formed between the surface and the bulk, making the sample not suitable for electrocatalysis.

The performances of the non- stoichiometric samples are better than their analogous stoichiometric ones. In $La_{0.9}Fe_{0.9}Ru_{0.1}O_{3-\delta}$, the exsolution process is more performing thanks to the A-site deficit which leads to the formation of oxygen vacancies, i.e. the driving force of the exsolution. Furthermore, it is reasonable to think that the quantity of lanthanum compounds is lower; in this case, the perovskite starts from a situation of instability and, through the segregation of the ruthenium (B-site cation) in excess, becomes a perovskite closer to the stoichiometric ratios. Furthermore, the deficit of lanthanum generates redox couples (mainly Fe^{3+}-Fe^{4+}), which decrease the impedance, especially *L0.9FR_750c_600e_400m* presents the lower impedance thanks to the presence of both NPs and a significative number of redox couples, achieving the best electrocatalytic performance among all the samples.

Electrochemical active surface area is affected by the redox treatments, but deeper studies are needed to understand its correlation to the catalytic activity.

La-deficit perovskite is promising to be regenerated, because the amount of lanthanum compounds formed after exsolution is lower than the stoichiometric. An attractive option to increase the performance of this system is an additional doping of strontium, which substitutes part of lanthanum, that should generate additional oxygen vacancies and redox couples since its oxidation state is 2+; moreover, in a suitable quantity, it induces a cubic crystal structure which enhances the electron mobility. This study tries to provide reasonable explanations on the effects of exsolution and subsequent treatments in Ru-doped La-Fe based perovskites; however, further studies are needed to corroborate them. Further investigation should also be done to understand the surface reconstruction and the changing on impedance and ECSA, and a possible technique useful to this purpose is high resolution scanning transmission electron microscopy (HR-STEM), capable of detecting and distinguishing smaller NPs and La-based layers. Overall, this work provides a valuable insight into the exsolution process, possibly implementable to La-Fe perovskites doped with noble or non-noble metals to make their use more efficient.

References

(1) Institute, E. *Home*. Statistical review of world energy. https://www.energyinst.org/statistical-review/home (accessed 2023-09-22).

(2) Perera, F.; Nadeau, K. Climate Change, Fossil-Fuel Pollution, and Children's Health. *N. Engl. J. Med.* **2022**, *386* (24), 2303–2314. https://doi.org/10.1056/NEJMra2117706.

(3) *Temperatures*. https://climateactiontracker.org/global/temperatures/ (accessed 2023-09-23).

(4) *Global Warming of 1.5 °C —*. https://www.ipcc.ch/sr15/ (accessed 2023-09-22).

(5) *Global Energy Crisis – Topics*. IEA. https://www.iea.org/topics/global-energy-crisis (accessed 2023-09-22).

(6) *Paris Agreement*; 2016. https://eur-lex.europa.eu/legal-content/EN/TXT/?uri=CELEX:22016A1019(01) (accessed 2023-10-06).

(7) *COMMUNICATION FROM THE COMMISSION TO THE EUROPEAN PARLIAMENT, THE EUROPEAN COUNCIL, THE COUNCIL, THE EUROPEAN ECONOMIC AND SOCIAL COMMITTEE AND THE COMMITTEE OF THE REGIONS The European Green Deal*; 2019. https://eur-lex.europa.eu/legal-content/EN/TXT/?qid=1576150542719&uri=COM%3A2019%3A640%3AFIN (accessed 2023-10-06).

(8) Ajanovic, A.; Sayer, M.; Haas, R. The Economics and the Environmental Benignity of Different Colors of Hydrogen. *Int. J. Hydrog. Energy* **2022**, *47* (57), 24136–24154. https://doi.org/10.1016/j.ijhydene.2022.02.094.

(9) European Commission. Joint Research Centre. *Assessment of the Methodology for Establishing the EU List of Critical Raw Materials :Background Report.*; Publications Office: LU, 2017.

(10) *European Critical Raw Materials Act*. European Commission - European Commission. https://ec.europa.eu/commission/presscorner/detail/en/ip_23_1661 (accessed 2023-09-23).

(11) CRMs_for_Strategic_Technologies_and_Sectors_in_the_EU_2020.Pdf. https://rmis.jrc.ec.europa.eu/uploads/CRMs_for_Strategic_Technologies_and_Sectors_in_the_EU_2020.pdf (accessed 2023-09-23).

(12) *Study on the Critical Raw Materials for the EU 2023 - Final Report*. https://single-market-economy.ec.europa.eu/publications/study-critical-raw-materials-eu-2023-final-report_en (accessed 2023-09-23).

(13) Durante C. Dispense del corso di *Electrochemistry of materials. University of Padua. 2020, unpublished.*

(14) Pilon, L.; Wang, H.; d'Entremont, A. Recent Advances in Continuum Modeling of Interfacial and Transport Phenomena in Electric Double Layer Capacitors. *J. Electrochem. Soc.* **2015**, *162* (5), A5158–A5178. https://doi.org/10.1149/2.0211505jes.

(15) Bard, A. J.; Faulkner, L. R. *Electrochemical Methods: Fundamentals and Applications*, 2nd ed.; Wiley: New York, 2001.

(16) Kumsa, D. W.; Bhadra, N.; Hudak, E. M.; Kelley, S. C.; Untereker, D. F.; Mortimer, J. T. Electron Transfer Processes Occurring on Platinum Neural Stimulating Electrodes: A Tutorial on the *i* (V_e) Profile. *J. Neural Eng.* **2016**, *13* (5), 052001. https://doi.org/10.1088/1741-2560/13/5/052001.

(17) Vidal-Iglesias, F. J.; Solla-Gullón, J.; Rodes, A.; Herrero, E.; Aldaz, A. Understanding the Nernst Equation and Other Electrochemical Concepts: An Easy Experimental Approach for Students. *J. Chem. Educ.* **2012**, *89* (7), 936–939. https://doi.org/10.1021/ed2007179.

(18) Seeber, R.; Zanardi, C.; Inzelt, G. Links between Electrochemical Thermodynamics and Kinetics. *ChemTexts* **2015**, *1* (4), 18. https://doi.org/10.1007/s40828-015-0018-9.

(19) Kuratani, K.; Fukami, K.; Tsuchiya, H.; Usui, H.; Chiku, M.; Yamazaki, S. Electrochemical Polarization Part 1: Fundamentals and Corrosion. *Electrochemistry* **2022**, *90* (10), 102003–102003. https://doi.org/10.5796/electrochemistry.22-66085.

(20) Hack, H. P. *Galvanic Corrosion*; ASTM International, 1988.

(21) Guidelli, R.; Compton, R. G.; Feliu, J. M.; Gileadi, E.; Lipkowski, J.; Schmickler, W.; Trasatti, S. Defining the Transfer Coefficient in Electrochemistry: An Assessment (IUPAC Technical Report). *Pure Appl. Chem.* **2014**, *86* (2), 245–258. https://doi.org/10.1515/pac-2014-5026.

(22) Franklin, R. K.; Martin, S. M.; Strong, T. D.; Brown, R. B. Chemical and Biological Systems: Chemical Sensing Systems for Liquids. In *Reference Module in Materials Science and Materials Engineering*; Elsevier, 2016. https://doi.org/10.1016/B978-0-12-803581-8.00549-X.

(23) Niu, S.; Li, S.; Du, Y.; Han, X.; Xu, P. How to Reliably Report the Overpotential of an Electrocatalyst. *ACS Energy Lett.* **2020**, *5* (4), 1083–1087. https://doi.org/10.1021/acsenergylett.0c00321.

(24) Karmakar, A.; Kundu, S. A Concise Perspective on the Effect of Interpreting the Double Layer Capacitance Data over the Intrinsic Evaluation Parameters in Oxygen Evolution Reaction. *Mater. Today Energy* **2023**, *33*, 101259. https://doi.org/10.1016/j.mtener.2023.101259.

(25) Morales, D. M.; Risch, M. Seven Steps to Reliable Cyclic Voltammetry Measurements for the Determination of Double Layer Capacitance. *J. Phys. Energy* **2021**, *3* (3), 034013. https://doi.org/10.1088/2515-7655/abee33.

(26) McCrory, C. C. L.; Jung, S.; Peters, J. C.; Jaramillo, T. F. Benchmarking Heterogeneous Electrocatalysts for the Oxygen Evolution Reaction. *J. Am. Chem. Soc.* **2013**, *135* (45), 16977–16987. https://doi.org/10.1021/ja407115p.

(27) Elgrishi, N.; Rountree, K. J.; McCarthy, B. D.; Rountree, E. S.; Eisenhart, T. T.; Dempsey, J. L. A Practical Beginner's Guide to Cyclic Voltammetry. *J. Chem. Educ.* **2018**, *95* (2), 197–206. https://doi.org/10.1021/acs.jchemed.7b00361.

(28) Sandford, C.; Edwards, M. A.; Klunder, K. J.; Hickey, D. P.; Li, M.; Barman, K.; Sigman, M. S.; White, H. S.; Minteer, S. D. A Synthetic Chemist's Guide to Electroanalytical Tools for Studying Reaction Mechanisms. *Chem. Sci.* **2019**, *10* (26), 6404–6422. https://doi.org/10.1039/C9SC01545K.

(29) Orazem, M. E.; Tribollet, B. Electrochemical Impedance Spectroscopy, 2nd Edition.

(30) Huggins, R. A. Simple Method to Determine Electronic and Ionic Components of the Conductivity in Mixed Conductors a Review. *Ionics* **2002**, *8* (3–4), 300–313. https://doi.org/10.1007/BF02376083.

(31) Lazanas, A. Ch.; Prodromidis, M. I. Electrochemical Impedance Spectroscopy–A Tutorial. *ACS Meas. Sci. Au* **2023**, *3* (3), 162–193. https://doi.org/10.1021/acsmeasuresciau.2c00070.

(32) Raveendran, A.; Chandran, M.; Dhanusuraman, R. A Comprehensive Review on the Electrochemical Parameters and Recent Material Development of Electrochemical Water Splitting Electrocatalysts. *RSC Adv.* **2023**, *13* (6), 3843–3876. https://doi.org/10.1039/D2RA07642J.

(33) Song, J.; Wei, C.; Huang, Z.-F.; Liu, C.; Zeng, L.; Wang, X.; Xu, Z. J. A Review on Fundamentals for Designing Oxygen Evolution Electrocatalysts. *Chem. Soc. Rev.* **2020**, *49* (7), 2196–2214. https://doi.org/10.1039/C9CS00607A.

(34) *Hydrogen Production: Electrolysis*. Energy.gov. https://www.energy.gov/eere/fuelcells/hydrogen-production-electrolysis (accessed 2023-09-15).

(35) Sui, Y.; Ji, X. Anticatalytic Strategies to Suppress Water Electrolysis in Aqueous Batteries. *Chem. Rev.* **2021**, *121* (11), 6654–6695. https://doi.org/10.1021/acs.chemrev.1c00191.

(36) Li, J. Oxygen Evolution Reaction in Energy Conversion and Storage: Design Strategies Under and Beyond the Energy Scaling Relationship. *Nano-Micro Lett.* **2022**, *14* (1), 112. https://doi.org/10.1007/s40820-022-00857-x.

(37) Zhu, K.; Shi, F.; Zhu, X.; Yang, W. The Roles of Oxygen Vacancies in Electrocatalytic Oxygen Evolution Reaction. *Nano Energy* **2020**, *73*, 104761. https://doi.org/10.1016/j.nanoen.2020.104761.

(38) Laursen, A. B.; Varela, A. S.; Dionigi, F.; Fanchiu, H.; Miller, C.; Trinhammer, O. L.; Rossmeisl, J.; Dahl, S. Electrochemical Hydrogen Evolution: Sabatier's Principle and the Volcano Plot. *J. Chem. Educ.* **2012**, *89* (12), 1595–1599. https://doi.org/10.1021/ed200818t.

(39) Cook, T. R.; Dogutan, D. K.; Reece, S. Y.; Surendranath, Y.; Teets, T. S.; Nocera, D. G. Solar Energy Supply and Storage for the Legacy and Nonlegacy Worlds. *Chem. Rev.* **2010**, *110* (11), 6474–6502. https://doi.org/10.1021/cr100246c.

(40) Cherevko, S.; Geiger, S.; Kasian, O.; Kulyk, N.; Grote, J.-P.; Savan, A.; Shrestha, B. R.; Merzlikin, S.; Breitbach, B.; Ludwig, A.; Mayrhofer, K. J. J. Oxygen and Hydrogen Evolution Reactions on Ru, RuO 2 , Ir, and IrO 2 Thin Film Electrodes in Acidic and Alkaline Electrolytes: A Comparative Study on Activity and Stability. *Catal. Today* **2016**, *262*, 170–180. https://doi.org/10.1016/j.cattod.2015.08.014.

(41) Kibsgaard, J.; Hellstern, T. R.; Choi, S.-J.; Reinecke, B. N.; Jaramillo, T. F. Mesoporous Ruthenium/Ruthenium Oxide Thin Films: Active Electrocatalysts for the Oxygen Evolution Reaction. *ChemElectroChem* **2017**, *4* (10), 2480–2485. https://doi.org/10.1002/celc.201700334.

(42) Basavarajappa, M. G.; Chakraborty, S. Rationalization of Double Perovskite Oxides as Energy Materials: A Theoretical Insight from Electronic and Optical Properties. *ACS Mater. Au* **2022**, *2* (6), 655–664. https://doi.org/10.1021/acsmaterialsau.2c00031.

(43) Li, H.; Yu, J.; Gong, Y.; Lin, N.; Yang, Q.; Zhang, X.; Wang, Y. Perovskite Catalysts with Different Dimensionalities for Environmental and Energy Applications: A Review. *Sep. Purif. Technol.* **2023**, *307*, 122716. https://doi.org/10.1016/j.seppur.2022.122716.

(44) Green, M. A.; Ho-Baillie, A.; Snaith, H. J. The Emergence of Perovskite Solar Cells. *Nat. Photonics* **2014**, *8* (7), 506–514. https://doi.org/10.1038/nphoton.2014.134.

(45) Liu, X.; Wang, Y.; Wang, Y.; Zhao, Y.; Yu, J.; Shan, X.; Tong, Y.; Lian, X.; Wan, X.; Wang, L.; Tian, P.; Kuo, H.-C. Recent Advances in Perovskites-Based Optoelectronics. *Nanotechnol. Rev.* **2022**, *11* (1), 3063–3094. https://doi.org/10.1515/ntrev-2022-0494.

(46) Hanif, M. B.; Rauf, S.; Motola, M.; Babar, Z. U. D.; Li, C.-J.; Li, C.-X. Recent Progress of Perovskite-Based Electrolyte Materials for Solid Oxide Fuel Cells and Performance Optimizing Strategies for Energy Storage Applications. *Mater. Res. Bull.* **2022**, *146*, 111612. https://doi.org/10.1016/j.materresbull.2021.111612.

(47) He, C.; Liu, X. The Rise of Halide Perovskite Semiconductors. *Light Sci. Appl.* **2023**, *12* (1), 15. https://doi.org/10.1038/s41377-022-01010-4.

(48) Brittman, S.; Adhyaksa, G. W. P.; Garnett, E. C. The Expanding World of Hybrid Perovskites: Materials Properties and Emerging Applications. *MRS Commun.* **2015**, *5* (1), 7–26. https://doi.org/10.1557/mrc.2015.6.

(49) Gu, C.; Lee, J.-S. Flexible Hybrid Organic–Inorganic Perovskite Memory. *ACS Nano* **2016**, *10* (5), 5413–5418. https://doi.org/10.1021/acsnano.6b01643.

(50) Peña, M. A.; Fierro, J. L. G. Chemical Structures and Performance of Perovskite Oxides. *Chem. Rev.* **2001**, *101* (7), 1981–2018. https://doi.org/10.1021/cr980129f.

(51) Lufaso, M. W.; Woodward, P. M. Jahn–Teller Distortions, Cation Ordering and Octahedral Tilting in Perovskites. *Acta Crystallogr. B* **2004**, *60* (1), 10–20. https://doi.org/10.1107/S0108768103026661.

(52) Zhu, H.; Zhang, P.; Dai, S. Recent Advances of Lanthanum-Based Perovskite Oxides for Catalysis. *ACS Catal.* **2015**, *5* (11), 6370–6385. https://doi.org/10.1021/acscatal.5b01667.

(53) Dias, J. A.; Andrade Jr, M. A. S.; Santos, H. L. S.; Morelli, M. R.; Mascaro, L. H. Lanthanum-Based Perovskites for Catalytic Oxygen Evolution Reaction. *ChemElectroChem* **2020**, *7* (15), 3173–3192. https://doi.org/10.1002/celc.202000451.

(54) Royer, S.; Duprez, D.; Can, F.; Courtois, X.; Batiot-Dupeyrat, C.; Laassiri, S.; Alamdari, H. Perovskites as Substitutes of Noble Metals for Heterogeneous Catalysis: Dream or Reality. *Chem. Rev.* **2014**, *114* (20), 10292–10368. https://doi.org/10.1021/cr500032a.

(55) Pidburtnyi, M.; Zanca, B.; Coppex, C.; Jimenez-Villegas, S.; Thangadurai, V. A Review on Perovskite-Type $LaFeO_3$ Based Electrodes for CO_2 Reduction in Solid Oxide Electrolysis Cells: Current Understanding of Structure–Functional Property Relationships. *Chem. Mater.* **2021**, *33* (12), 4249–4268. https://doi.org/10.1021/acs.chemmater.1c00771.

(56) Kwon, O.; Joo, S.; Choi, S.; Sengodan, S.; Kim, G. Review on Exsolution and Its Driving Forces in Perovskites. *J. Phys. Energy* **2020**, *2* (3), 032001. https://doi.org/10.1088/2515-7655/ab8c1f.

(57) Kousi, K.; Tang, C.; Metcalfe, I. S.; Neagu, D. Emergence and Future of Exsolved Materials. *Small* **2021**, *17* (21), 2006479. https://doi.org/10.1002/smll.202006479.

(58) Neagu, D.; Oh, T.-S.; Miller, D. N.; Ménard, H.; Bukhari, S. M.; Gamble, S. R.; Gorte, R. J.; Vohs, J. M.; Irvine, J. T. S. Nano-Socketed Nickel Particles with Enhanced Coking Resistance Grown in Situ by Redox Exsolution. *Nat. Commun.* **2015**, *6* (1), 8120. https://doi.org/10.1038/ncomms9120.

(59) Han, H.; Park, J.; Nam, S. Y.; Kim, K. J.; Choi, G. M.; Parkin, S. S. P.; Jang, H. M.; Irvine, J. T. S. Lattice Strain-Enhanced Exsolution of Nanoparticles in Thin Films. *Nat. Commun.* **2019**, *10* (1), 1471. https://doi.org/10.1038/s41467-019-09395-4.

(60) Burnat, D.; Kontic, R.; Holzer, L.; Steiger, P.; Ferri, D.; Heel, A. Smart Material Concept: Reversible Microstructural Self-Regeneration for Catalytic Applications. *J. Mater. Chem. A* **2016**, *4* (30), 11939–11948. https://doi.org/10.1039/C6TA03417A.

(61) Lai, K.-Y.; Manthiram, A. Self-Regenerating Co–Fe Nanoparticles on Perovskite Oxides as a Hydrocarbon Fuel Oxidation Catalyst in Solid Oxide Fuel Cells. *Chem. Mater.* **2018**, *30* (8), 2515–2525. https://doi.org/10.1021/acs.chemmater.7b04569.

(62) Jiang, Y.; Geng, Z.; Sun, Y.; Wang, X.; Huang, K.; Cong, Y.; Shi, F.; Wang, Y.; Zhang, W.; Feng, S. Highly Efficient B-Site Exsolution Assisted by Co Doping in Lanthanum Ferrite toward High-Performance Electrocatalysts for Oxygen Evolution and Oxygen Reduction. *ACS Sustain. Chem. Eng.* **2020**, *8* (1), 302–310. https://doi.org/10.1021/acssuschemeng.9b05344.

(63) Tang, L.; Chen, Z.; Zuo, F.; Hua, B.; Zhou, H.; Li, M.; Li, J.; Sun, Y. Enhancing Perovskite Electrocatalysis through Synergistic Functionalization of B-Site Cation for Efficient Water Splitting. *Chem. Eng. J.* **2020**, *401*, 126082. https://doi.org/10.1016/j.cej.2020.126082.

(64) Ma, J.; Geng, Z.; Jiang, Y.; Hou, X.; Ge, X.; Wang, Z.; Huang, K.; Zhang, W.; Feng, S. Exsolution Manipulated Local Surface Cobalt/Iron Alloying and Dealloying Conversion in La0·95Fe0·8Co0·2O3 Perovskite for Oxygen Evolution Reaction. *J. Alloys Compd.* **2021**, *854*, 157154. https://doi.org/10.1016/j.jallcom.2020.157154.

(65) Liang, Y.; Cui, Y.; Chao, Y.; Han, N.; Sunarso, J.; Liang, P.; He, X.; Zhang, C.; Liu, S. Exsolution of CoFe(Ru) Nanoparticles in Ru-Doped (La0.8Sr0.2)0.9Co0.1Fe0.8Ru0.1O3−δ for Efficient Oxygen Evolution Reaction. *Nano Res.* **2022**, *15* (8), 6977–6986. https://doi.org/10.1007/s12274-022-4328-0.

(66) Fu, L.; Zhou, J.; Zhou, L.; Yang, J.; Liu, Z.; Wu, K.; Zhao, H.; Wang, J.; Wu, K. Facile Fabrication of Exsolved Nanoparticle-Decorated Hollow Ferrite Fibers as Active Electrocatalyst for Oxygen Evolution Reaction. *Chem. Eng. J.* **2021**, *418*, 129422. https://doi.org/10.1016/j.cej.2021.129422.

(67) Jiang, Y.; Geng, Z.; Yuan, L.; Sun, Y.; Cong, Y.; Huang, K.; Wang, L.; Zhang, W. Nanoscale Architecture of RuO_2/$La_{0.9}Fe_{0.92}Ru_{0.08-x}O_{3-\delta}$ Composite via Manipulating the Exsolution of Low Ru-Substituted A-Site Deficient Perovskite. *ACS Sustain. Chem. Eng.* **2018**, *6* (9), 11999–12005. https://doi.org/10.1021/acssuschemeng.8b02288.

(68) Brinker, C. J.; Scherer, G. W. *Sol-Gel Science: The Physics and Chemistry of Sol-Gel Processing*; Gulf Professional Publishing, 1990.

(69) Danks, A. E.; Hall, S. R.; Schnepp, Z. The Evolution of 'Sol–Gel' Chemistry as a Technique for Materials Synthesis. *Mater. Horiz.* **2016**, *3* (2), 91–112. https://doi.org/10.1039/C5MH00260E.

(70) Definitions, Terminology, and Symbols in Colloid and Surface Chemistry. *Chem. Int. -- Newsmag. IUPAC* **2003**, *25* (1). https://doi.org/10.1515/ci.2003.25.1.18c.

(71) *The IUPAC Compendium of Chemical Terminology: The Gold Book*, 4th ed.; Gold, V., Ed.; International Union of Pure and Applied Chemistry (IUPAC): Research Triangle Park, NC, 2019. https://doi.org/10.1351/goldbook.

(72) Cochran, E. A.; Woods, K. N.; Johnson, D. W.; Page, C. J.; Boettcher, S. W. Unique Chemistries of Metal-Nitrate Precursors to Form Metal-Oxide Thin Films from Solution: Materials for Electronic and Energy Applications. *J. Mater. Chem. A* **2019**, *7* (42), 24124–24149. https://doi.org/10.1039/C9TA07727H.

(73) Carlos, E.; Martins, R.; Fortunato, E.; Branquinho, R. Solution Combustion Synthesis: Towards a Sustainable Approach for Metal Oxides. *Chem. – Eur. J.* **2020**, *26* (42), 9099–9125. https://doi.org/10.1002/chem.202000678.

(74) Deganello, F.; Tyagi, A. K. Solution Combustion Synthesis, Energy and Environment: Best Parameters for Better Materials. *Prog. Cryst. Growth Charact. Mater.* **2018**, *64* (2), 23–61. https://doi.org/10.1016/j.pcrysgrow.2018.03.001.

(75) Kim, S. J.; Yoon, S.; Kim, H. J. Review of Solution-Processed Oxide Thin-Film Transistors. *Jpn. J. Appl. Phys.* **2014**, *53* (2S), 02BA02. https://doi.org/10.7567/JJAP.53.02BA02.

(76) Parauha, Y. R.; Sahu, V.; Dhoble, S. J. Prospective of Combustion Method for Preparation of Nanomaterials: A Challenge. *Mater. Sci. Eng. B* **2021**, *267*, 115054. https://doi.org/10.1016/j.mseb.2021.115054.

(77) Chick, L. A.; Pederson, L. R.; Maupin, G. D.; Bates, J. L.; Thomas, L. E.; Exarhos, G. J. Glycine-Nitrate Combustion Synthesis of Oxide Ceramic Powders. *Mater. Lett.* **1990**, *10* (1–2), 6–12. https://doi.org/10.1016/0167-577X(90)90003-5.

(78) Najjar, H.; Lamonier, J.-F.; Mentré, O.; Giraudon, J.-M.; Batis, H. Optimization of the Combustion Synthesis towards Efficient LaMnO3+y Catalysts in Methane Oxidation. *Appl. Catal. B Environ.* **2011**, 149–159. https://doi.org/10.1016/j.apcatb.2011.05.019.

(79) Pine, T.; Lu, X.; Mumm, D. R.; Samuelsen, G. S.; Brouwer, J. Emission of Pollutants from Glycine–Nitrate Combustion Synthesis Processes. *J. Am. Ceram. Soc.* **2007**, *0* (0), 3736–3740. https://doi.org/10.1111/j.1551-2916.2007.01919.x.

(80) Thommes, M.; Kaneko, K.; Neimark, A. V.; Olivier, J. P.; Rodriguez-Reinoso, F.; Rouquerol, J.; Sing, K. S. W. Physisorption of Gases, with Special Reference to the Evaluation of Surface Area and Pore Size Distribution (IUPAC Technical Report). *Pure Appl. Chem.* **2015**, *87* (9–10), 1051–1069. https://doi.org/10.1515/pac-2014-1117.

(81) Schlumberger, C.; Thommes, M. Characterization of Hierarchically Ordered Porous Materials by Physisorption and Mercury Porosimetry—A Tutorial Review. *Adv. Mater. Interfaces* **2021**, *8* (4), 2002181. https://doi.org/10.1002/admi.202002181.

(82) Wang, Y.; Gallego, J.; Wang, W.; Timmer, P.; Ding, M.; Luciano, A. S.; Weber, T.; Glatthaar, L.; Guo, Y.; Smarsly, B. M.; Over, H. Unveiling the Self-Activation of Exsolved La $Fe_{0.9}$ $Ru_{0.1}$ O_3 Perovskite During the Catalytic Total Oxidation of Propane. Submitted.

(83) Iervolino, G.; Vaiano, V.; Sannino, D.; Rizzo, L.; Palma, V. Enhanced Photocatalytic Hydrogen Production from Glucose Aqueous Matrices on Ru-Doped LaFeO3. *Appl. Catal. B Environ.* **2017**, *207*, 182–194. https://doi.org/10.1016/j.apcatb.2017.02.008.

(84) Mehtougui, N.; Rached, D.; Khenata, R.; Rached, H.; Rabah, M.; Bin-Omran, S. Structural, Electronic and Mechanical Properties of RuO2 from First-Principles Calculations. *Mater. Sci. Semicond. Process.* **2012**, *15* (4), 331–339. https://doi.org/10.1016/j.mssp.2012.02.001.

(85) Yang, J.-K.; Kim, W. S.; Park, H.-H. Chemical Bonding States and Energy Band Gap of SiO2-Incorporated La2O3 Films on n-GaAs (001). *Thin Solid Films* **2006**, *494* (1–2), 311–314. https://doi.org/10.1016/j.tsf.2005.08.159.

(86) Zhu, K.; Shi, F.; Zhu, X.; Yang, W. The Roles of Oxygen Vacancies in Electrocatalytic Oxygen Evolution Reaction. *Nano Energy* **2020**, *73*, 104761. https://doi.org/10.1016/j.nanoen.2020.104761.

Supporting materials

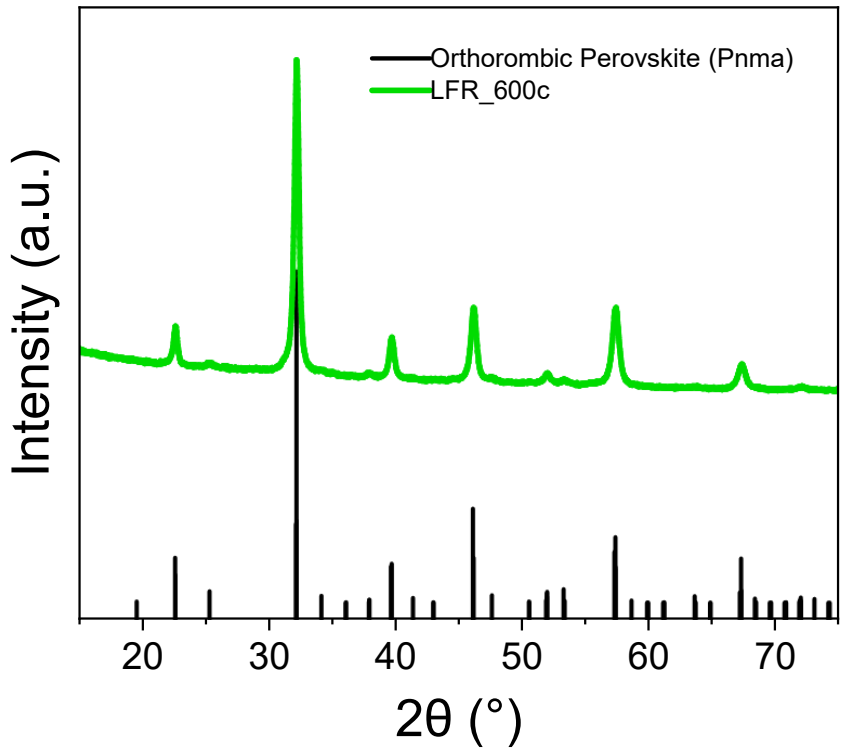

***Figure S1**. XRD diffractogram of as-burned $LaFe_{0.9}Ru_{0.1}O_3$ after calcination at 600 °C (LFR_600c).*

a) LFR_750c

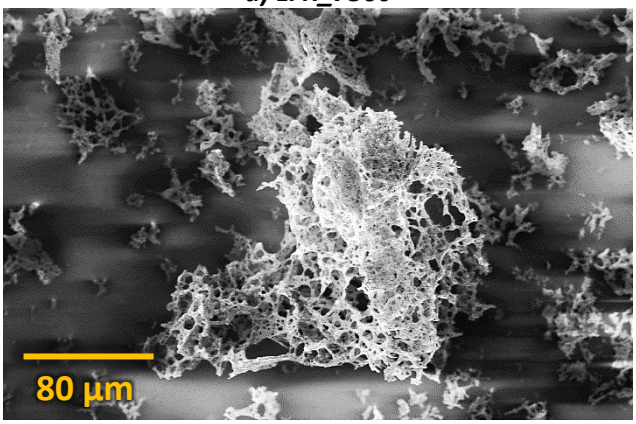

b) *LFR_750c_800e*

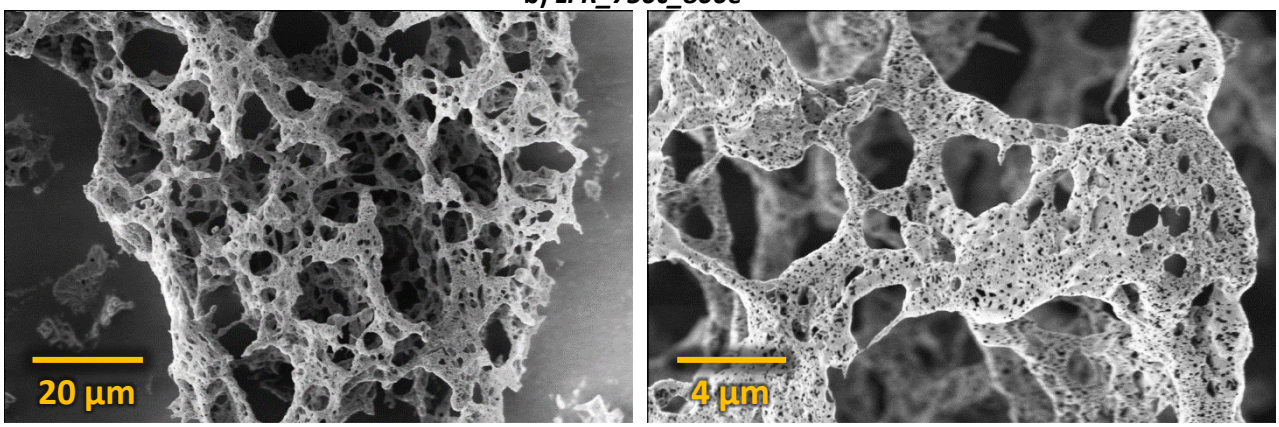

c) *LFR_750c_800e_400m*

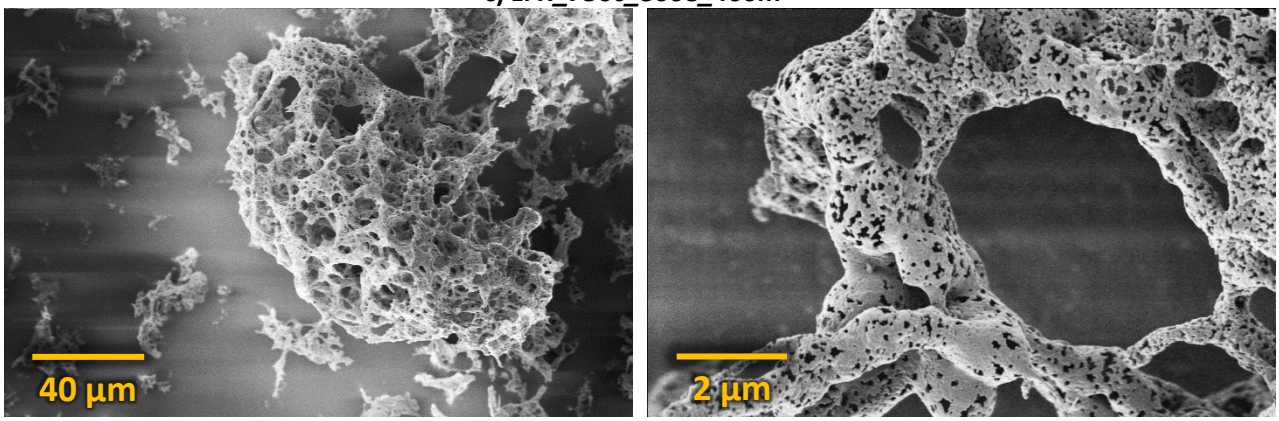

***Figure S2**. SEM images of **a)** LFR_750c, **b)** LFR_750c_800e, **c)** LFR_800e_400m.*

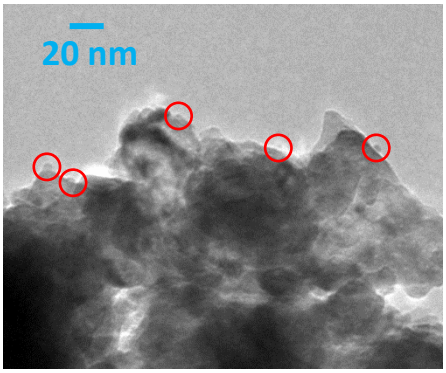

***Figure S3**. TEM image of LFR_750c_600e. Some NPs are indicated with red circles.*

LFR_750c_400e

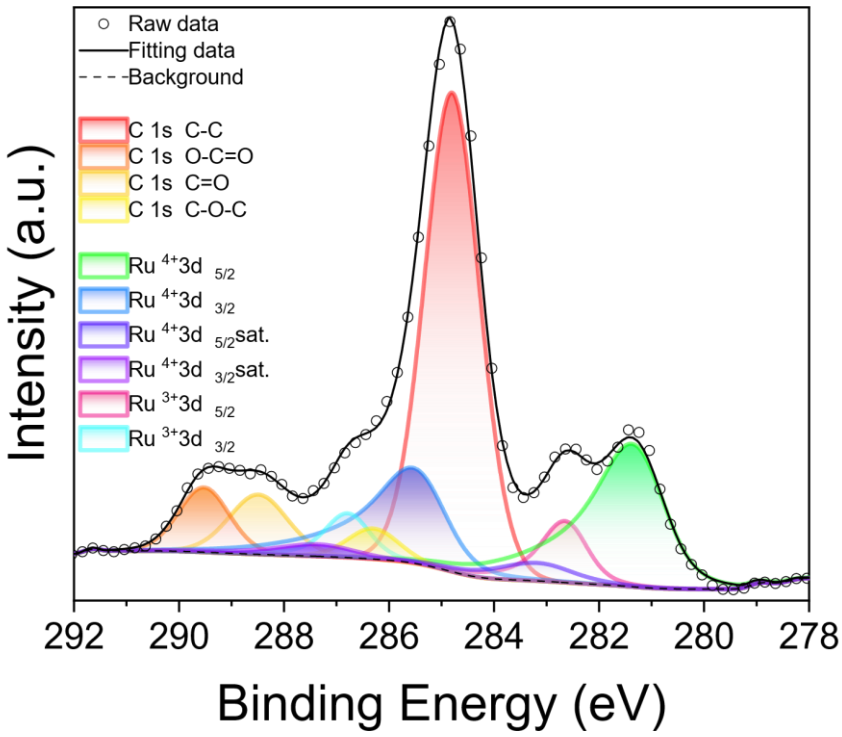

Figure S4*. XPS spectra of LFR_750c_400e*

LFR_750c_500e

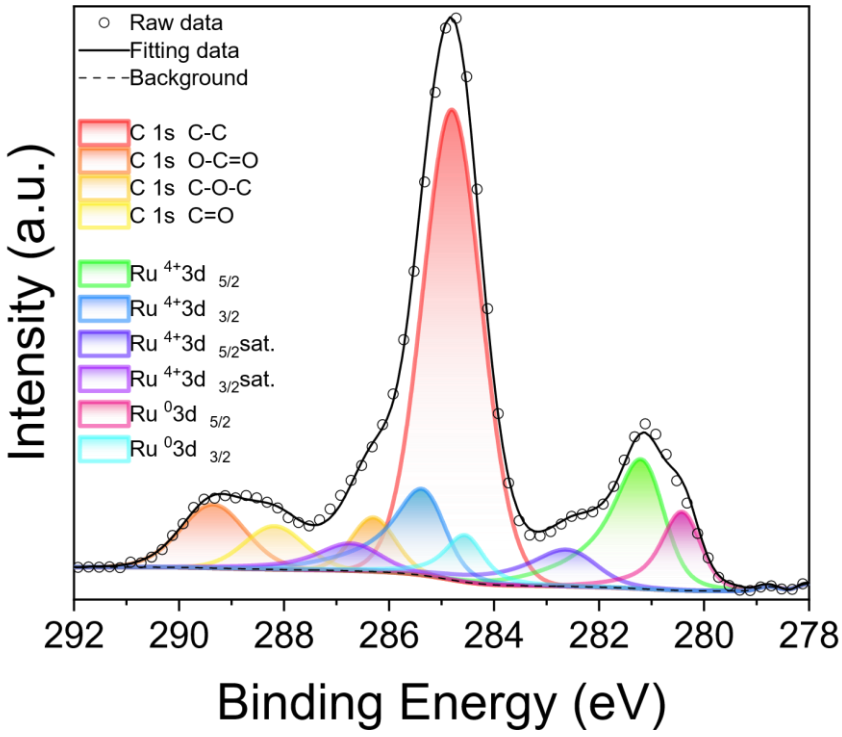

Figure S5*. XPS spectra of LFR_750c_500e*

LFR_750c_600e

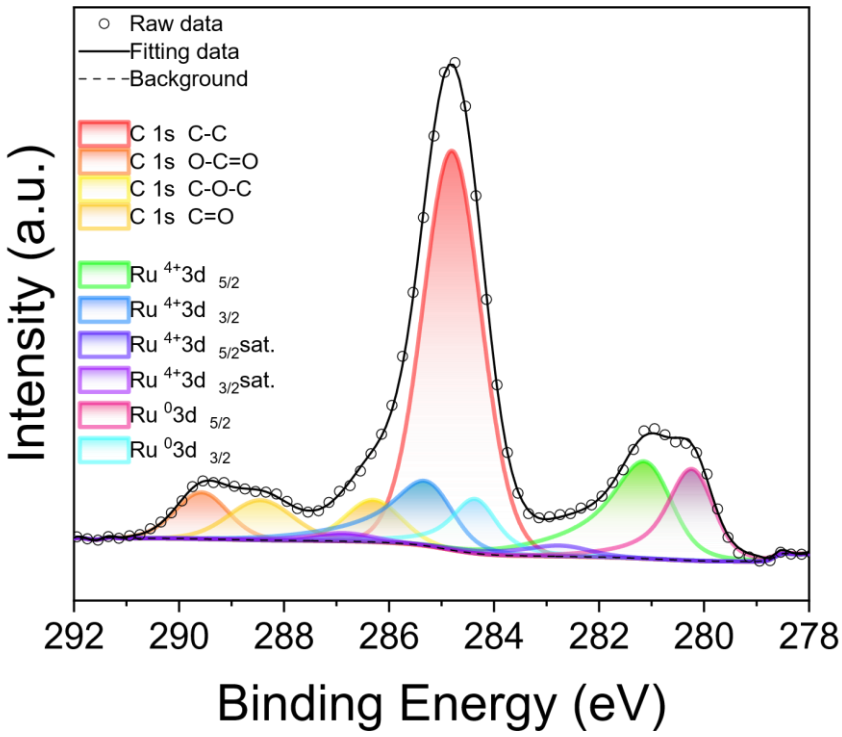

Figure S6*. XPS spectra of LFR_750c_600e*

LFR_750c_700e

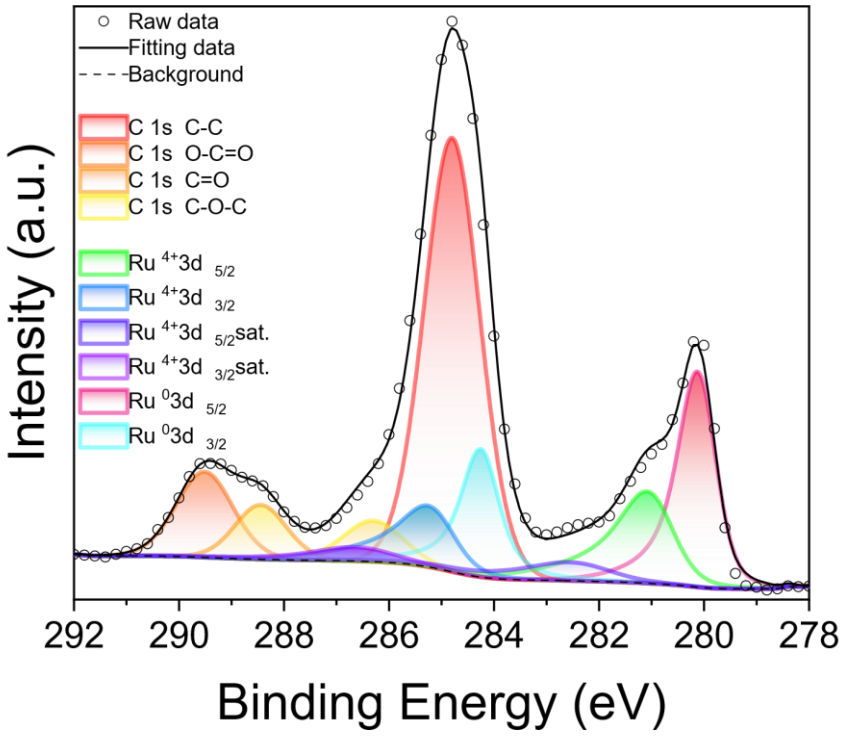

Figure S7*. XPS spectra of LFR_750c_700e*

LFR_750c_800e

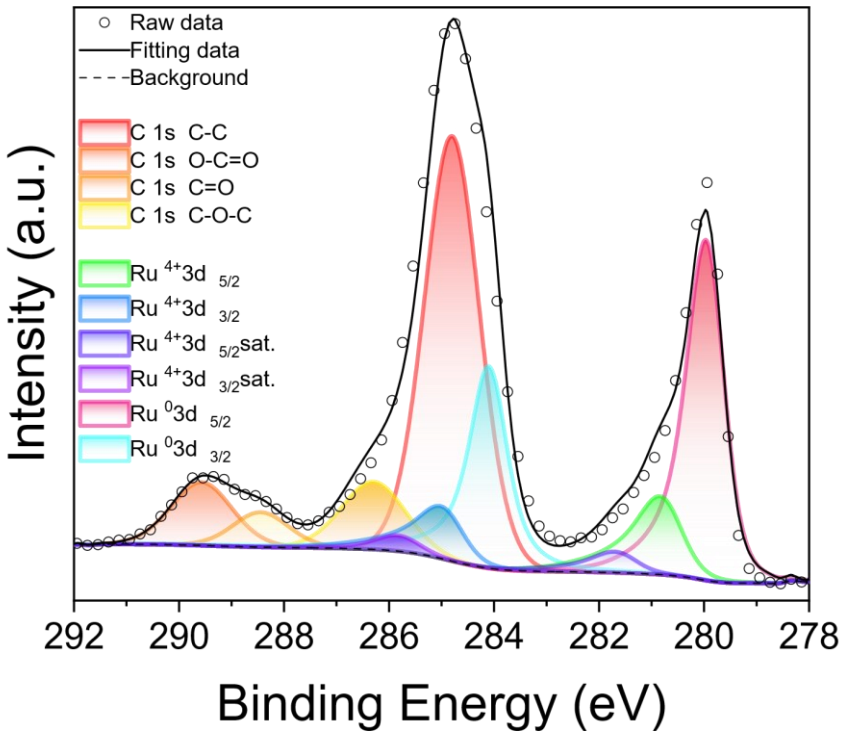

***Figure S8**. XPS spectra of LFR_750c_800e*

LFR_750c_400e_400m

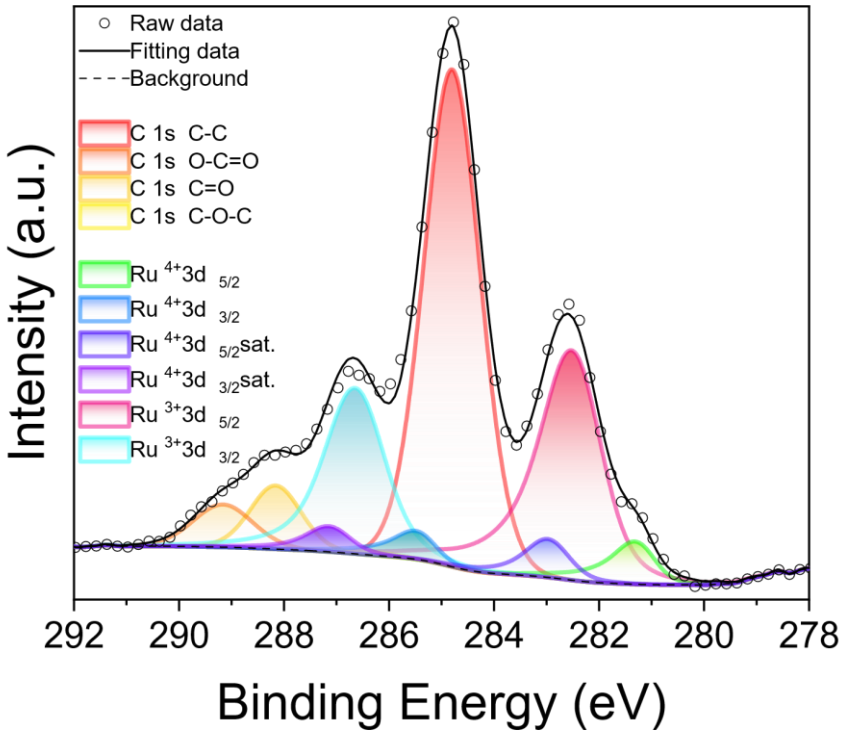

***Figure S9**. XPS spectra of LFR_750c_400e_400m*

LFR_750c_500e_400m

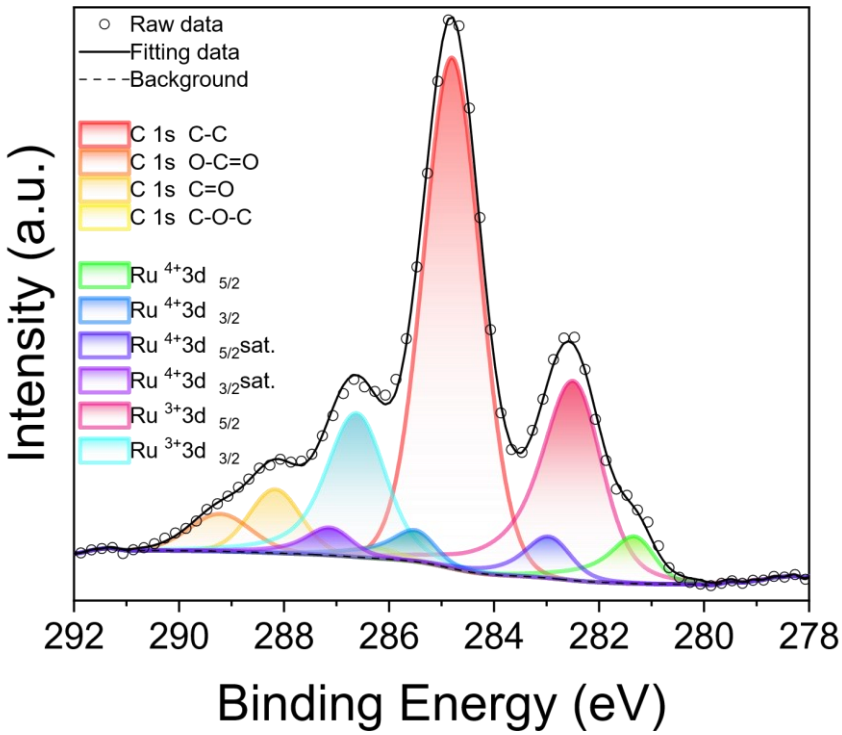

***Figure S10**. XPS spectra of LFR_750c_500e_400m*

LFR_750c_600e_400m

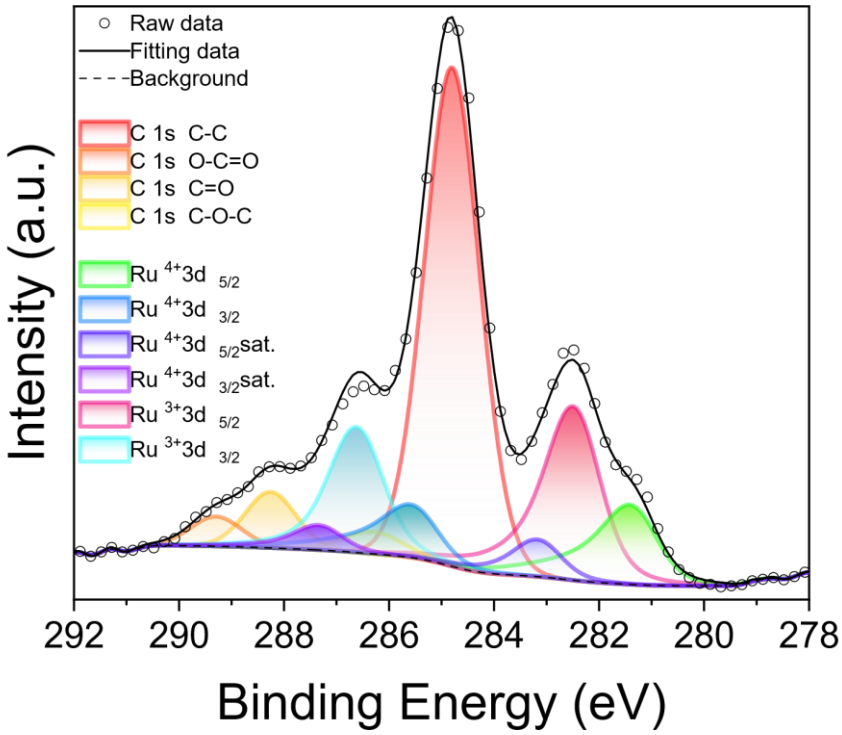

***Figure S11**. XPS spectra of LFR_750c_600e_400m*

LFR_750c_700e_400m

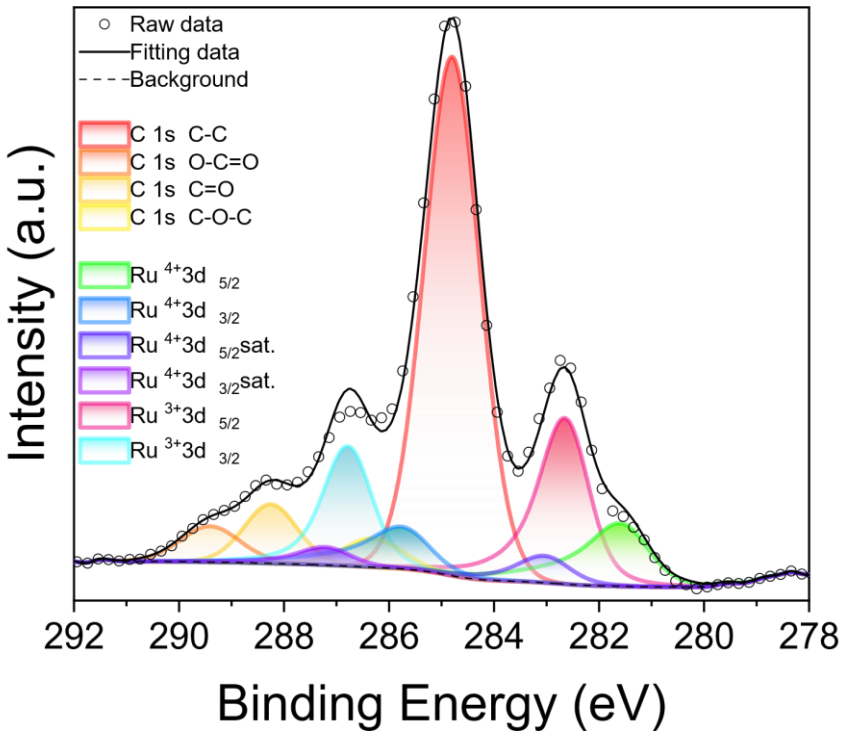

***Figure S12**. XPS spectra of LFR_750c_700e_400m*

LFR_750c_800e_400m

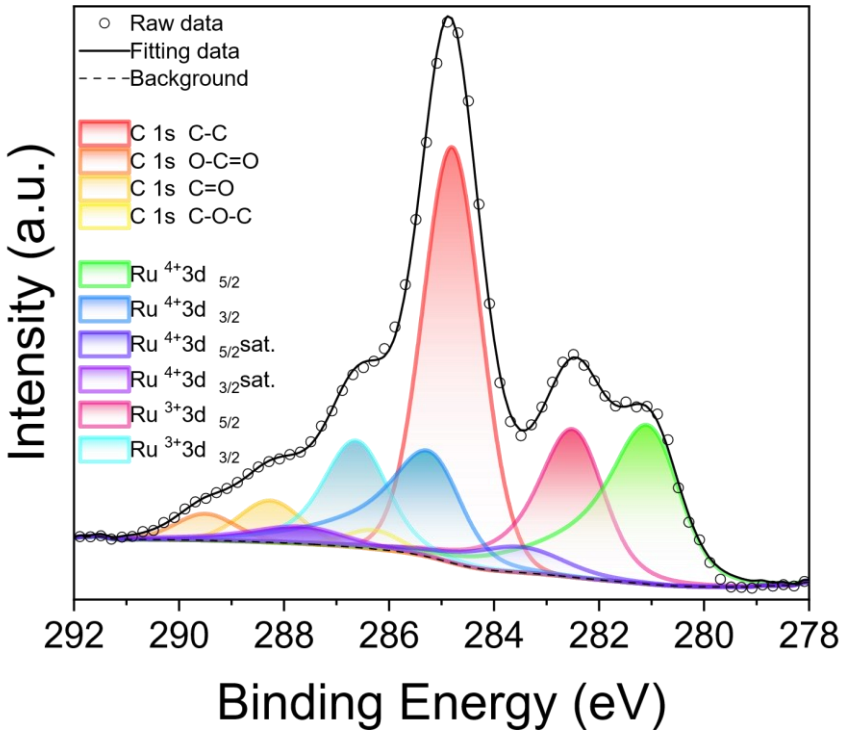

***Figure S13**. XPS spectra of LFR_750c_800e_400m*

LFR_750c_800e_750h

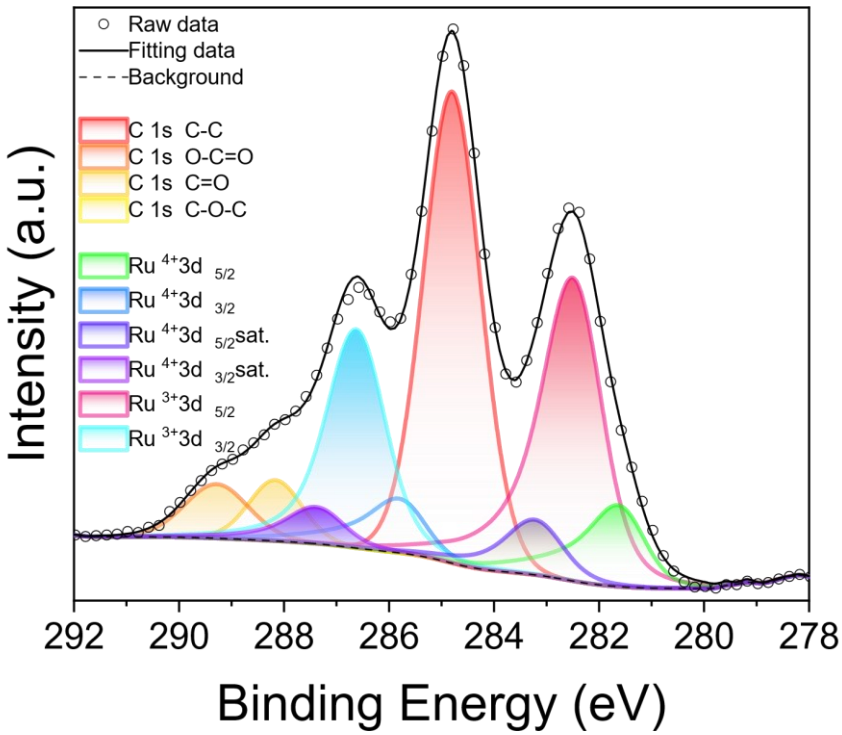

***Figure S14**. XPS spectra of LFR_750c_800e_750h*

LFR_750c_800e_740h_600e2

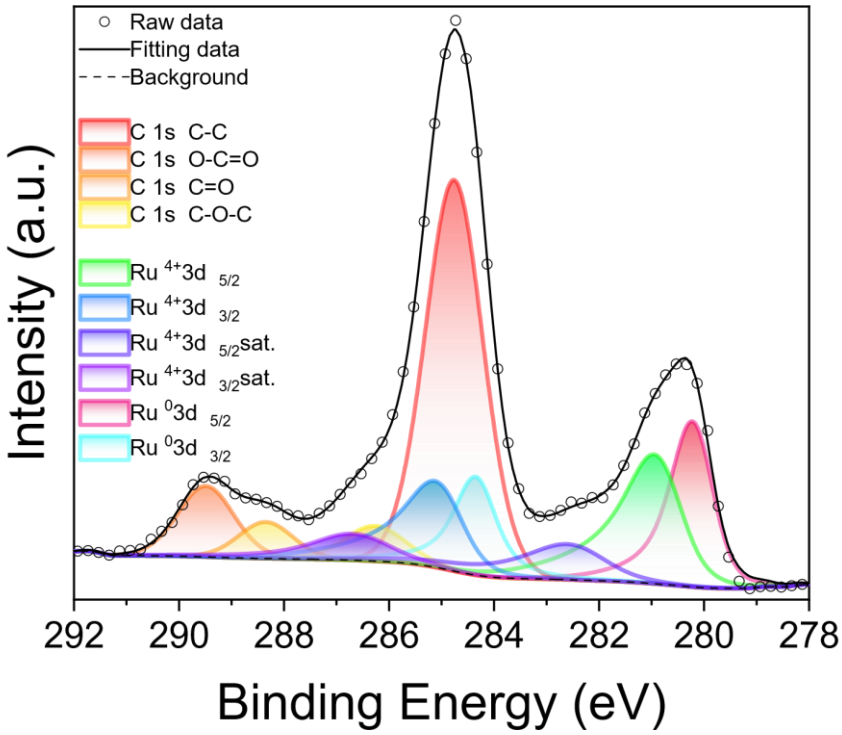

***Figure S15**. XPS spectra of LFR_750c_800e_750h_600e2*

LFR_750c_800e_750h_600e2_400m2

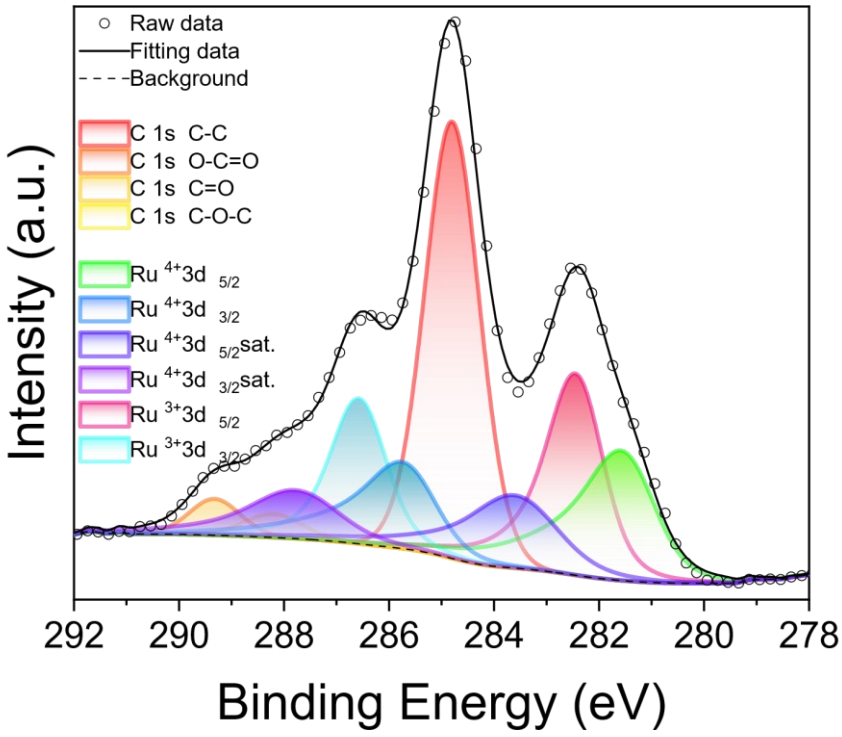

***Figure S16**. XPS spectra of LFR_750c_800e_750h_600e2_400m2*

L0.9FR_750c

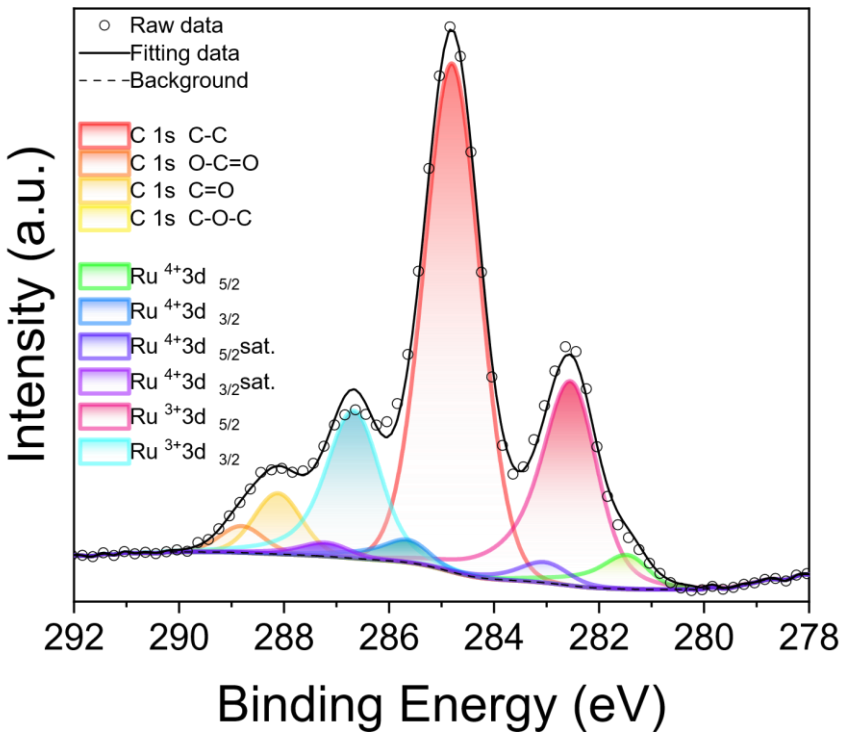

***Figure S17**. XPS spectra of L0.9FR_750c*

L0.9FR_750c_600e

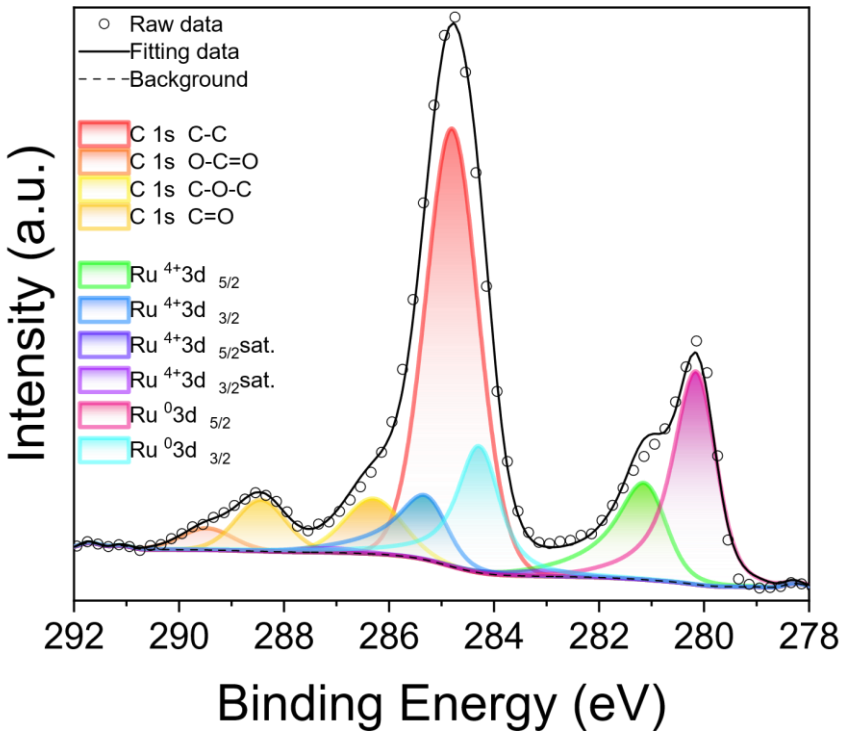

***Figure S18**. XPS spectra of L0.9FR_750c_600e*

L0.9FR_750c_600e_400m

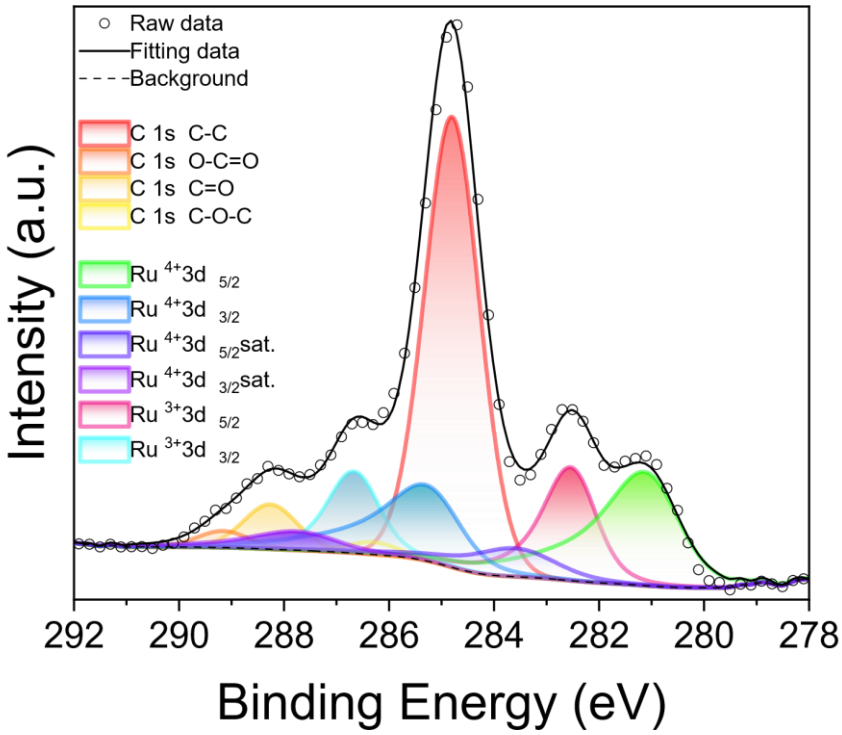

***Figure S19**. XPS spectra of L0.9FR_750c_600e_400m*